Characterization of the greywacke basement of Taupo Volcanic Zone geothermal fields

- New Zealand -

Thesis submitted in accordance with the requirements of the University of Liverpool for the degree of Master of Philosophy

by

Aurelio Melia

November 2016

Dedicated to my parents and my fiancée

ACKNOWLEDGMENTS

First of all I would like to express my sincere gratitude to my supervisor Dan Faulkner for allowing me to have this awesome experience in the Rock Deformation Lab and for leading me through this MPhil, encouraging and supporting me from the beginning till the end of this work. Throughout all this time he taught me a lot, not just regarding our scientific talks and experiments explanations, but also in his way of thinking and approaching the problems, inspiring me in this project and in real life.

My gratitude goes also to David McNamara for being an amazing supervisor. Dave's support during all these months was fundamental to achieve the final results: by giving me important advises and essential information on what I was working on. He did it from everywhere and at any time.

I would like to deeply thank GNS Science - New Zealand for funding my project. Furthermore, I can't but thank Betty Mariani for the precious advises imparted along the course of my permanence at the University of Liverpool and for allowing me to use her own optical microscope, it saved me a lot of time.

I would like also to thank all the people working in the Rockdef Lab, first Gary for training me on some machines and for his constant technical support in most of the lab/workshop operations. Then, Sabine, Pamela, Catalina, Jo, Rachael, who created with their sense of humor a nice atmosphere in the lab. In a particular way, I have to thank John for the trainings, Carolyn for the important advises about my petrographic observations and overall Mike, who has been constantly available during all the period of my project for every request.

Thanks also to all the guys of the Volcanology Lab, overall to Felix von Aulock who helped me for the thermo-analysis measurements. Thanks to Carmel Pinnington and Sarah Henton for the trainings to the SEM and related operations. Also thanks to Paula Houghton from the financial office, she has been always ready to help me, often even above her competences. I have also to thank all the people who supported me in the department and in the administration offices. Working in the lab has been a fantastic

experience and I really feel to have learned a lot, also if in a relatively short period of time.

Family and friends played an important role supporting me throughout the entire process both by keeping me harmonious and helping me putting pieces together.

Thanks to all my friends and flat mates in Liverpool for giving me ways to relax and enjoy through all this time. In particular thanks to Nicolò, for watching the exciting European Cup together and for his very tasty dishes and to my old and dear friend Lamberto without whom I would not be writing this thesis now.

I thank my family, my Mom and Dad for supporting me in everything, for this new challenge, and for bearing the distance. The same for my brothers Riccardo and in a special way Dario.

The final thanks are for Rita, to whom this thesis is dedicated. There are no words to thank her for what she has done for me. Even though she is far she has always been the main reference point in everything, supporting me and giving me the patience to go on, day after day.

I will be always grateful to all of you.

ABSTRACT

Geothermal energy usage is spreading around the world in both electricity generation and direct use. In New Zealand geothermal resources are known to be hosted in greywacke basement rocks. The fracture networks control fluid flow in these reservoirs and the wells that access them. Hence, it is very important to understand how these structures are impacted by the mechanical and thermal properties of this basement rock, and how these in turn are affected by the change of temperature and pressure conditions at depth.

Faults and fractures are a key mechanism for the transport of fluids through the crust, providing a pathway for the emplacement and development of geothermal systems. This project utilizes geomechanics, geophysics and petrology to investigate the dynamics of fluid flow within the greywacke basement at Taupo Volcanic Zone (New Zealand), in relation to the exploitation of the geothermal energy. The experimental work describes the response of this lithology under different conditions of stress and temperature, which are factors influencing the permeability of the reservoir rocks. The results have implications for permeability models of this area, which are fundamental for the planning and development of geothermal fields.

The tests that have been carried out are targeted to describe the physical properties of this material and their relation to fluid flow. Uniaxial tests, seismic waves velocity measurements, Brazilian tests, porosity measurements, triaxial testing, permeability measurements, and thermo-analysis have been utilized in order to acquire data on elastic properties (E= 54 - 85 GPa; v= 0.19 - 0.36), strength (UCS= 205 - 384 MPa; tensile strength= 14 - 32 MPa), seismic wave velocity (Vp= 5.89 - 6.41 km/s; Vs= 3.20 - 3.61 km/s), porosity (ϕ= 1.035%), permeability (k_{nat}= ~10^{-21} m^2), thermal properties (α_L= 11.617·10^{-6} $°C^{-1}$). These data are accompanied by information on the rock composition and microstructure.

Comparisons of the results are made with the purpose of understanding the similarities or differences between previously acquired data and the new data generated

here. The interpretation of the laboratory results is important in order to have a better idea about the greywacke basement, in terms of physical properties.

Following on from the characterization of the basement in this work, it will be possible in the future to understand better the failure mechanisms of these greywackes using numerical simulations of failure and to evaluate the future implications for the geothermal fields in New Zealand.

TABLE OF CONTENTS

LIST OF TABLES

LIST OF FIGURES

INTRODUCTION

Geothermal energy usage is spreading around the world in both electricity generation, and direct use (Bertani, 2011) (e.g. spas and swimming pools, space heating (including district applications), greenhouse heating, aquaculture, industrial uses, snow melting, and agricultural drying). This trend is particularly developed in New Zealand electricity production, which, following the data of Ministry of Business, Innovation and Employment (2016), is increased in providing from geothermal resources from ~7% in 2000 to ~17% in 2015.

In most geothermal systems around the world, structure, at many scales from fracturing to faulting, are the main control on fluid flow. Geothermal environments are susceptible to variable heat fluxes, dynamic fluid flow regimes, and active tectonics which impact the physical and mechanical properties of the reservoir rocks where they are held. Such a dynamic environment has an impact that can render the host rocks highly altered, fractured, and microstructurally complex (Siratovich et al., 2014). Consequently, the experimental correlation of physical properties to produce valuable relationships may not be entirely straightforward. In order to help in the optimization and maintenance of geothermal resources, studies of these properties, and attempts to quantify how they relate to one another in the subsurface are important (e.g., Gupta and Sukanta 2006; Di Pippo 2008; Grant and Bixley 2011).

Moreover, the heat flow, stress state, permeability and commercial potential of a geothermal reservoir can be highly influenced by the behavior and the impact of a thermal gradient on a geothermal resource. Induced or natural thermal gradients can cause thermal cracking of rock (David et al., 1999) which leads to the degradation of strength (Heap et al., 2013b) and an increase in permeability (Faoro et al., 2013). It is essential to do detailed studies on the conditions that constrain the onset of thermal cracking in a geothermal reservoir for the optimal utilization of the resource, wellbore stability considerations, reservoir forecasting, and stimulation procedures (e.g. Zoback et al., 2003; Ghassemi and Zhang, 2004; Grant and Bixley, 2011). Thermal cracking is also an important process concerning a number of geological phenomena, such as magmatic dyke emplacement, contact metamorphism, and cooling of magma and lava bodies. It is necessary to quantify the thermal properties of the reservoir rocks to endorse the understanding of thermo-mechanical behavior in a geothermal reservoir.

The Taupo Volcanic Zone (TVZ) in New Zealand is a NE-SW oriented and fault controlled volcano-tectonic depression, filled by Quaternary volcano-sedimentary lithologies with underlying faulted Mesozoic greywacke basement and with dimensions approximately 350 km long and 60 km wide (Alcaraz et al., 2012). The present geothermal development for electricity production in New Zealand utilises reservoirs at depths up to ~3.5 km, establishing what is known as the "conventional" resource. Future development of geothermal power in New Zealand aims at deeper potential reservoirs including a potential deep (4-5 km) drilling project (Bignall, 2011). But is geothermal energy a viable sustainable energy source likely to replace fossil fuels on a large scale? The average continental heat flow is 50 mW/m^2, in New Zealand has been reported a very large variation of the heat flow has been reported, from 20.9 to 336 mW/m^2 (Simpson, 1987). Hence the average heat flow for New Zealand corresponds to 71.7mW/m^2, namely the average of heat flow for islands arcs (Jessop et al., 1976). Therefore, with a surface of 267,710 km^2 and with a power consumption of 39.6 GWh (2011), in New Zealand the geothermal could sustainably satisfy circa 50% of the power required in one year for the whole country. This demonstrates that geothermal energy can be an important source of power, maybe not enough to replace totally fossil fuels, but if complemented with other renewable energies could play a fundamental role giving energy independence in countries with low power consumption and a heat flow above the average. This is evident when comparing New Zealand to United Kingdom (2014), which has smaller surface area (243,610 km^2), lower heat flow (around the continental average) and a very large power consumption (257 GWh). The requirement for power would be around twenty times more than geothermal energy could supply.

In New Zealand geothermal resources are known to be hosted in greywacke basement rocks (Wallis et al., 2012). The fracture networks control fluid flow in these reservoirs and the wells that access them. Hence, it is very important to understand how these structures are impacted by the mechanical and thermal properties of this basement rock, and how these in turn are affected by the change of temperature and pressure conditions at depth. Current knowledge of the brittle deformation (faults and fractures) at extended depths (beyond conventional) in the TVZ basement rocks comes from seismic investigations, which indicate a potential convective geothermal regime exists to

depths of ~6 - 8 km (Bibby et al., 1995; Bryan et al., 1999). Thus, in order to determine how fluids move in these basement rocks at these depths, it is fundamental to study the rock conditions and mechanics in relation to the variation of pressures and temperatures.

The main focus of this thesis will be to characterize the greywacke basement rocks (from the Waipapa Terrane) that underlie some of New Zealand's geothermal regions, through its physical properties. In order to fulfill this target, various laboratory experiments were carried out, including uniaxial compressive strength (UCS) tests with the aim of calculating the elastic properties and to understand the strength of this rock. During the UCS tests P and S wave velocities were measured in order to help establish the degree of microfracture density. Rock tensile strength was also investigated through Brazilian tests, for which new test equipment was expressly designed and manufactured.

Experiments were also performed under conventional triaxial conditions ($\sigma_1 > \sigma_2 = \sigma_3$) and data about strength and pore volume variation were acquired. During the triaxial tests P and S wave velocity measurements were carried out and permeability measurements were performed using the pulse transient method. Other measurements of permeability were made in greywacke samples in which a single diametric macrofracture was created. I also investigated how this macrofracture maintained or lost aperture under various confining pressure conditions.

In addition, porosity was also measured for a consistent range of greywacke basement rock samples. Microstructural observations were performed using the optical microscope and scanning electron microscope (SEM) on samples with both natural cracks and induced cracks during deformation experiments. This was done in order to study the types of crack morphology, fill, and fracture state of the rock. Finally, to obtain information about the thermal properties of the greywacke in the geothermal reservoir, thermo-analysis measurements were carried out on core samples.

The results of this study provide insight into the nature of fracturing in the basement rocks that underlie some of New Zealand's geothermal resources, and thus how they control fluid flow. Results on mechanical and thermal properties, as well as porosity and permeability, will be useful to constrain parameters for thermo-mechanical modeling of fluid flow in existing basement hosted geothermal fields in New Zealand, and theoretical deep (>3.5 km) resources that may be targeted in the future.

CHAPTER 1:

STUDY AREA - TAUPO VOLCANIC ZONE (TVZ)

The first chapter of this thesis introduces and describes the study area of this work, and gives an essential background of knowledge for the following parts where more specific details will be treated.

Chapter 1 is divided in two sections: the first section talks about the geological history of Taupo Volcanic Zone, where the study took place. After a quick geographical framing, the attention will be focused on the geologic evolution and the geologic structures that characterize this area, going through the sedimentary fillings of the basins, supported by examples, maps and cross sections.

The second section presents the main properties that are involved in a project for a geothermal system. To make a project of a geothermal field requires a 360 degrees study from the big scale, which involves tectonic studies, through a regional scale, to a small scale, which involves the site where the well is planned to be drilled. Obviously, to choose the best location to drill, which involves a large budget, requires a lot of effort. The studies to identify the site begin with the identification of the structures that can act as source of hot fluids, continue with the characterization of the lithologies, to reach a final result that involves all the properties of the geothermal fields. Finally, a quick general view on geothermal systems will be given through few examples.

1.1. GEOLOGICAL SETTING

New Zealand is located on the border between Pacific Plate and the Australian Plate. In the North Island the Pacific Plate subducts underneath the Australian Plate, whereas in the South Island the Australian Plate subducts beneath the Pacific Plate, with a transition between these two occurring between the two islands. The geothermal activity in New Zealand is related to subduction underneath the North Island where tectonic stress (rifting) and volcanism is responsible for the generation of the pathways that result in the creation of geothermal fields.

1.1.1. THE GEOGRAPHICAL LOCATION AND TECTONIC SETTINGS OF THE TVZ

The study area, called the Taupo Volcanic Zone (TVZ), is located in the center of the North Island, (Fig. 1.1). This area corresponds to the southernmost, ~300 km-long, portion of the ~2800 Km-long Tonga-Kermadec arc system (Cole and Lewis, 1981; Luyendyk, 1995; Mortimer, 2004; Smith Price, 2006; Wilson and Roland, 2016) (Fig. 1.2). The TVZ is acknowledged worldwide for its powerful volcanic and geothermal manifestations. Specifically, this central TVZ hosts an extraordinarily vigorous active hydrothermal region which, tied with its volcanic productivity, puts it in the same rank as the Yellowstone system (Christiansen, 2001; Hurwitz and Lowenstern, 2014). In detail, the central TVZ has a present day average heat flow of 700 mW/m^2 and a total flux of 4.2 GW (Bibby et al., 1995; Hochstein, 1995; Wilson and Roland, 2016). In total, the TVZ hosts twenty-four geothermal fields (Fig. 1.1).

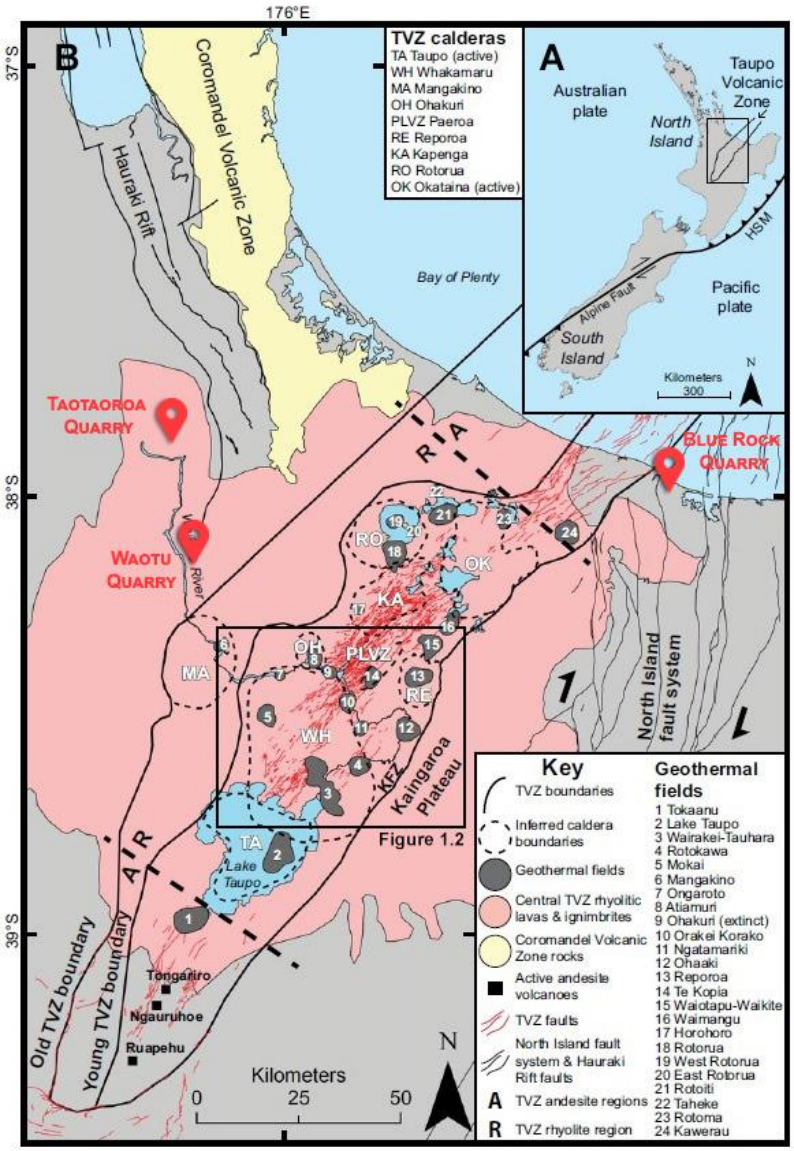

Figure 1.1: a) Large scale map of New Zealand. b) Summary map of central North Island showing the TVZ and the position of its geothermal fields. The box represents Fig. 1.2 (Downs et al., 2014). The red indicators show the locations of the quarries from where the samples were taken: Taotaoroa Quarry (TTGW), Waotu Quarry (WHGW) and Blue Rock Quarry (BRGW).

The central TVZ can be geographically divided into two parallel basins extending in a northeast-southwest direction (Downs et al., 2014). The northwestern basin is identified as the Taupo Fault Belt (TFB), which displays typical rift morphology (Rowland and Sibson, 2001), the seismicity is vigorous (Bryan et al., 1999), and based on paleoseismology, has subsided at a rate of 3 to 4 mm/yr (Villamor and Berryman, 2001). The southeastern basin is the Taupo-Repora Basin (TRB) (Fig. 1.2). Seismically

it is less active than the TFB (Bryan et al., 1999), but has subsided at a similar rate of 3 to 4 mm/yr (Manville, 2001). The kinematics of the TFB are predominantly normal, with a possible minor component of strike-slip motion (Rowland and Sibson, 2001; Acocella et al., 2003). Information on the kinematics of the TRB as well as its contribution to the tectonic and magmatic evolution of the TVZ is less known. The TRB is however significantly interesting for the high temperature (>250 °C) geothermal resources located within it which are explored and studied for energy generation in New Zealand (Fig. 1.1 and Fig. 1.2). The total estimated resource in this basin exceeds 2000 MW (Bibby et al., 1995).

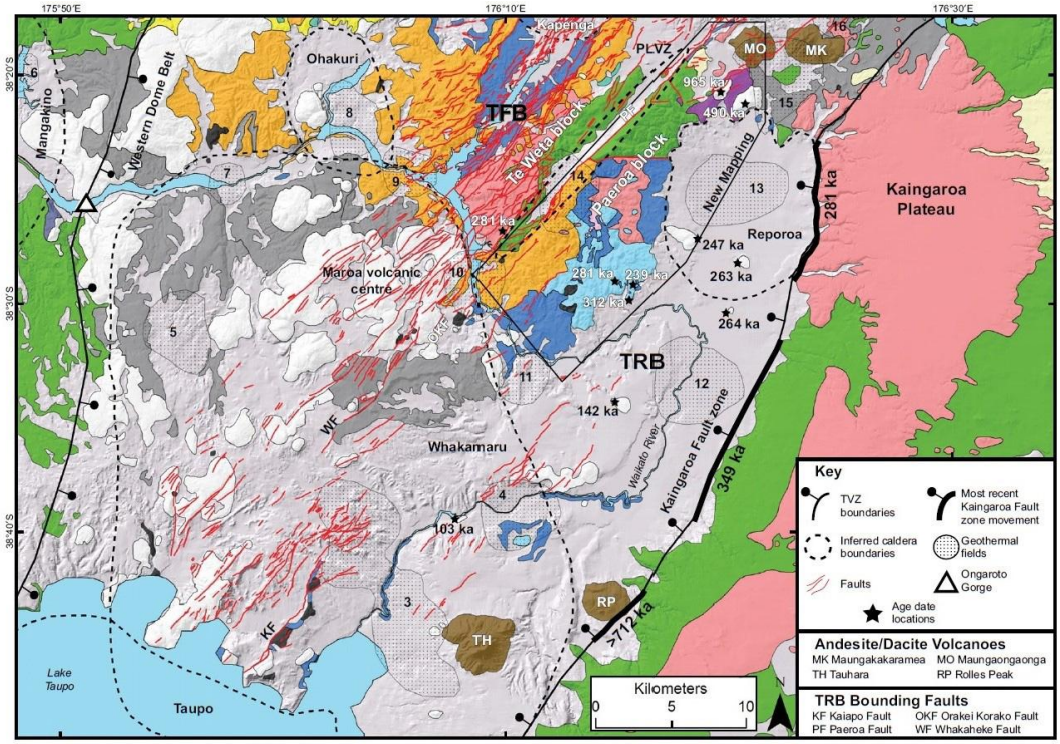

Figure 1.2: Geologic map of part of TVZ showing the distribution of lavas, volcaniclastic and sedimentary strata. Fig.1.1 shows which area of New Zealand is described in this map. The Taupo-Repora Basin (TRB) is located in the North / West side of the Kaingaroa Fault. The Taupo Fault Belt (TFB) is the basin located in the North area, which displays typical rift morphology. The corresponding stratigraphy is illustrated in Fig. 1.3 (Downs et al., 2014).

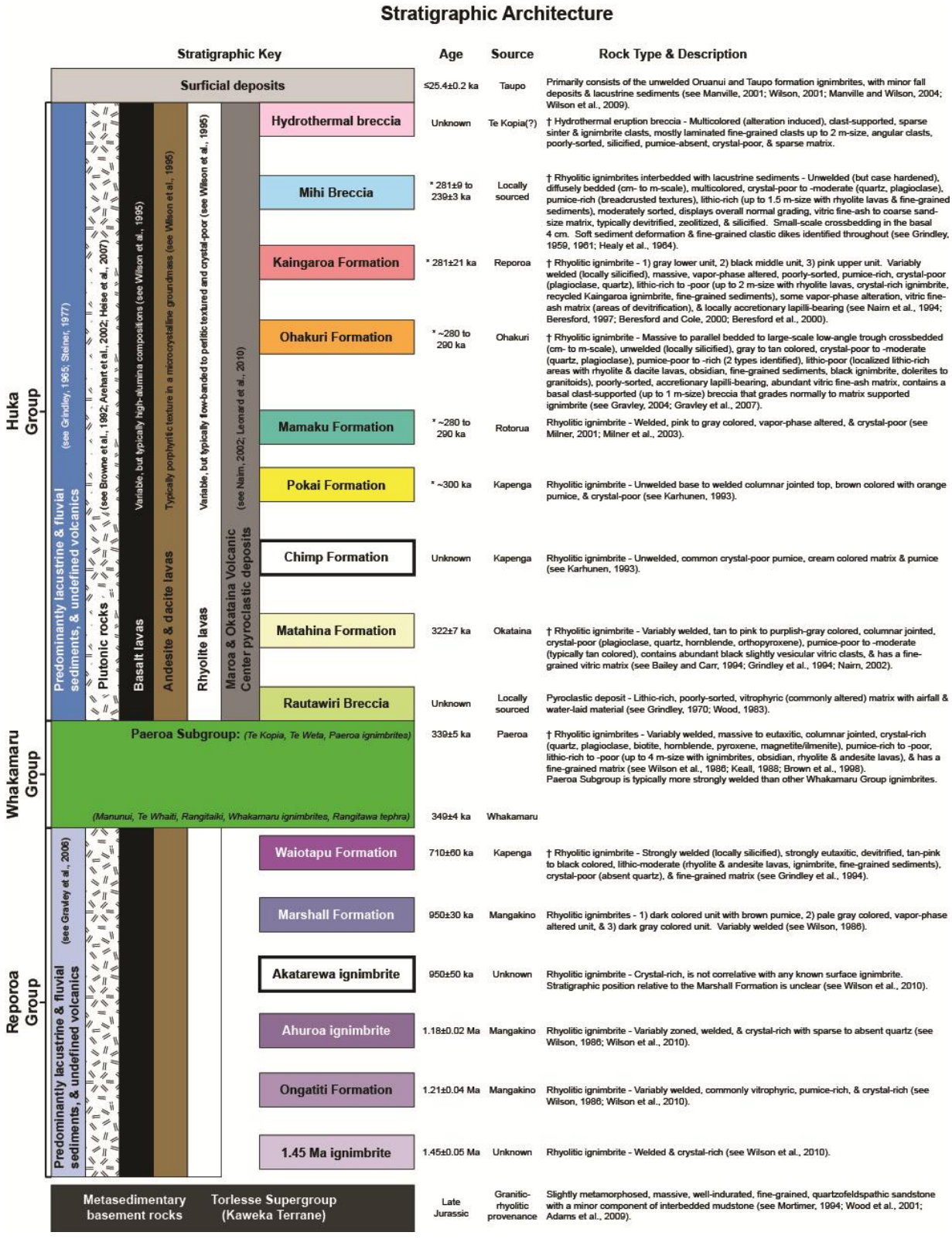

Figure 1.3: Stratigraphic architecture, descriptions, and key for all deposits discussed within the text and shown in Fig. 1.2, for which this figure acts as legend (Downs et al., 2014). This stratigraphy characterizes the North Island and the TVZ (Fig.1.1).

1.1.2. GEOLOGY OF TVZ

This section presents the early geological history of TVZ area and its evolution with the migration of the TVZ arc. A general view is given about the three parts of TVZ, northern, central and southern portions. Moreover, the main tectonic structures are also described, which play a fundamental role in the geothermal activity zone. Finally, examples of the stratigraphy will be given, which will be briefly described to give an idea of the composition of the TVZ basins.

1.1.2.1. Current tectonic setting

The genesis and evolution of the modern TVZ represents only the latest stage of a long and complex history of interactions between the Pacific and Australian plates over the past 25–30 m.y. (e.g., Schellart et al., 2006; Mortimer et al., 2010; Schellart and Spakman, 2012; Reyners, 2013; Timm et al., 2014). The present-day configuration of the subduction system displays westwards directed oblique subduction of the Pacific plate beneath the Australian plate under the North Island of New Zealand (Fig. 1.4) (Wilson and Roland, 2016).

The NE-SW trending TVZ represents the most recent (last ~2 m.y.) tectonic manifestation connected to this subduction (Fig. 1.1) (Mortimer et al., 2010). The migration of the TVZ arc-rifting can be identified in terms of temporal evolution and divides the TVZ into sectors called: Old TVZ, Young TVZ and Modern TVZ (Fig. 1.5).

The TVZ presents both structural and volcanic structures. A central area (central TVZ), dominated by rhyolitic volcanism in a region 120 Km long and 60 Km wide, is characterized by arc-related composite cone-building andesitic volcanism co-located along the axis of the rift (Fig. 1.1) (Wilson et al., 1995).

Structurally, the axis of the rift is offset along strike by transfer (accommodation) zones that align with caldera margins, geothermal fields, and inferred

deep-seated basement faults, some of which align with faults of the North-Northwest trending Hauraki Rift (Rowland and Sibson, 2001, 2004; Downs et al., 2014).

The volcaniclastic filled basins are interpreted as developing gradually through secular rifting (Villamor and Berryman, 2001; Nicol et al., 2006), which rises in magnitude from ~3 to >15 mm/yr from Southwest to Northeast, respectively, along the axis of the TVZ (Wallace et al., 2004). Furthermore, within the central TVZ another event of basin-forming process happened that adds complexity to the structural and stratigraphic history of the district. The central TVZ has undergone a minimum of 25 rhyolitic eruptions over the last 1.6 m.y., which were large from 30 to >1500 Km^3, causing the development of at least eight calderas (Wilson et al., 2009). These calderas have a diameter range between ~10 and 40 Km and are overlaid upon. In some episodes perhaps they are directly linked with the formation of fault-controlled rift basins (Gravley et al., 2007; Rowland et al., 2010; Allan et al., 2012). The Taupo volcanic center (Fig. 1.1) is the modern source of rhyolitic volcanism (Nairn, 2002; Wilson et al., 2009; Downs et al., 2014).

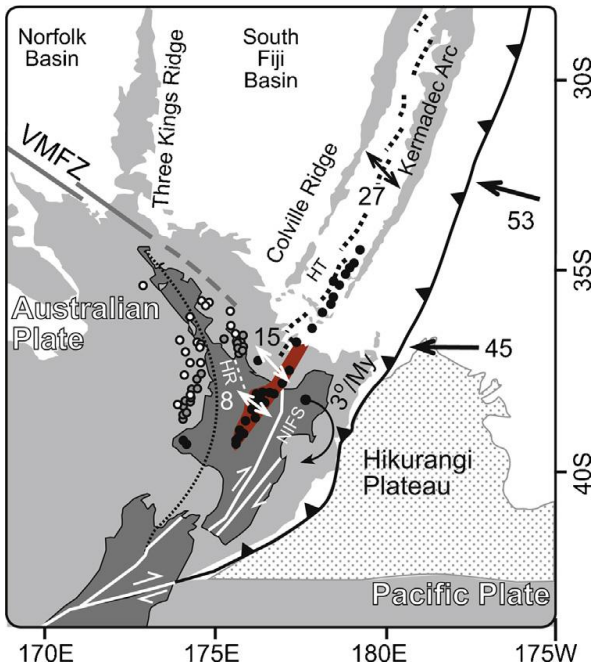

Figure 1.4: Current tectonic setting of northern New Zealand, annotated with localities of volcanism for three different time periods ± 0.5 Ma (Circles: black = 0 Ma; grey = 8 Ma; white = 16 Ma) from Seebeck

et al. (2014a), geodetic vectors of extension (double arrows: Parson and Wright, 1996; Wallace et al., 2004) and relative plate motion (single arrows: De Mets et al., 1994) in mm/year. Terrane suture in basement rocks as inferred from magnetic anomaly = dotted line. Rotation of eastern North Island shown for the period 3 Ma to present (Wallace et al., 2004). HR = Hauraki Rift; HT = Havre trough; NIFS = North Island Fault System; VMFZ = Vening Meinesz Fracture Zone (see text for context). From Wilson and Rowland, 2016.

1.1.2.2. How is the TVZ subdivided?

The tectonic and volcanic features described previously potentially control the TVZ rifting processes and the occurrence and nature of large-scale faults which can operate as both barriers and pathways for deep fluid flow (Rowland and Sibson, 2004; Rowland and Simmons, 2012). The main tectonic elements that had a principal role in the Late Oligocene to the present evolution of the plate boundary and which had probable impacts on the structure of the TVZ are reported in Fig. 1.1 and include:

a. Old TVZ:

The Old TVZ includes volcanic systems active from ca. 2 Ma up to 350 ka, for which most of the rocks and their source volcanoes have been destroyed by erosion or burial. Products of this activity crop out generally in the western TVZ, but are recorded in geothermal drill holes between 1–3 km depth (Gravley et al., 2006; Wilson et al.,2008b, 2010; Rosenberg et al., 2009; Eastwood et al., 2013; Milicich et al., 2013a; Chambefort et al., 2014), and are in large quantities present in contemporary sedimentary basins (Shane and Froggatt, 1991; Alloway et al., 2004; Pillans et al., 2005) and in deep-sea cores (Carter et al., 2003, 2004; Alloway et al., 2005; Allan et al., 2008). A comprehensive stratigraphy and chronology inside this period has yet to be established (Wilson and Rowland, 2016).

b. Young TVZ:

The Young TVZ includes volcanic systems active from 350 ka to about 61 ka, namely during the establishment of the major structural features of the TVZ that control the positions and nature of the TVZ geothermal systems. The lower boundary for this

time division is that defined by the widespread and voluminous fall deposits and ignimbrites collectively called the Whakamaru Group (Leonard et al., 2010). The eruption record for this period is partly complete, particularly for the larger-scale events (Manning, 1995, 1996; Wilson et al., 2009) but many aspects of the local structural histories are unknown.

c. Modern TVZ:

The Modern TVZ consists of volcanic systems active since 61 ka. This period is defined as that since the Rotoiti eruption, dated at 61 ka by Wilson et al. (2007), but with an alternative age of 45 ka (Danisík et al., 2012). The eruption record for the central TVZ from this time period is considered to be complete (Vucetich and Howorth, 1976; Wilson, 1993; Nairn, 2002; Jurado-Chichay and Walker, 2000) and its deposits are marker planes for present-day tectonics in the central North Island. The eruptive histories of the andesitic volcanoes in the northern and southern TVZ segments are known in variable amounts of detail only for the later part of this period (e.g., Donoghue et al., 1995; Cronin and Neall, 1997; Cole et al.,2000; Moebis et al., 2011; Pardo et al., 2012).

In addition to temporal division of the TVZ, it can also be discussed in terms of distributions of various types volcanism with three distinct segments (Healy, 1962; Cole, 1979; Wilson et al., 1995; Wilson and Rowland, 2015):

Northern TVZ is delimited by the Kawerau area and northward out beyond White Island to the edge of the continental shelf (and beyond to the Kermadec Arc: Gamble et al., 1993). The arc volcanism is principally represented by andesite–dacite composite cones. There is an intense geothermal system at White Island, but in general there are presently only low-level geothermal manifestations.

Central TVZ includes the area between Kawerau and Tokaanu at the southern end of Lake Taupo. This area is dominated by silicic volcanism and magmatism with connected geothermal activity and rift-related faulting (Wilson et al., 1995).

Southern TVZ is delimited by the Pihanga-Kakaramea chain of composite cones to the isolated vents southwest of Mount Ruapehu. Typically, most continental arcs show this kind of segment, with large composite cones dominated by andesite–dacite compositions (with a rare presence of basalt and without rhyolite), and a limited manifestation of hydrothermal activity (Wilson et al., 1995).

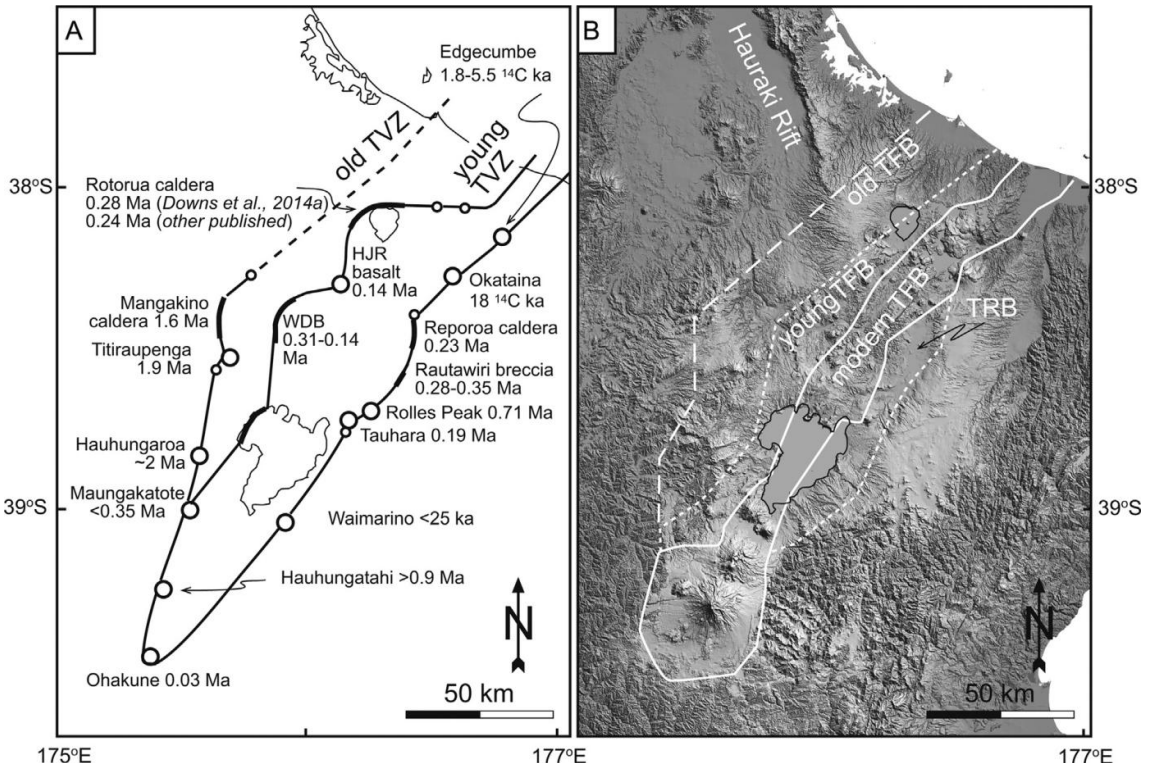

Figure 1.5: a) Definition of the TVZ formed by envelopes that enclose all volcanic vent structures known or inferred to have been active in the 2 Myr lifetime of the zone (old TVZ) and the last 350 kyr (Young TVZ). Major lakes outlined by thin black lines; b) Boundaries of the evolution and migration of TFB and location of TRB. In detail are shown the envelopes enclosing the Modern (<26 ka), Young (340–26 ka) and Old (>340 ka) Taupo Fault Belt structural domains (from Wilson and Rowland, 2016).

1.1.3. STRATIGRAPHY

The TVZ basins were filled contemporaneously with continuous magmatic events, including rhyolite lavas, andesite and dacite lavas, basalt lavas, and plutonic intrusions, and from around 2 Ma with ignimbrite deposits and other volcanic-type deposits, as well as breccias, sandstone and siltstone deposits associated with lacustrine and fluvial environments (Grindley, 1965; Steiner, 1977; Wilson et al., 1995; Gravley et al., 2006). A cross section of the Kawerau Geothermal Field is provided as an example of the typical stratigraphy of the TVZ, and the locations of magmatic bodies within the volcano-sedimentary formations overlying over the greywacke basement (Fig.1.6). In this cross-section it can be seen that above the greywacke basement there is the succession of volcano-sedimentary formations into which andesite lava (Kawerau Andesite) and rhyolite lava (Caxton Formation) bodies and intrusive bodies (Caxton Formation intrusive) have been emplaced. Brief descriptions of these formations are shown in Table 1.1.

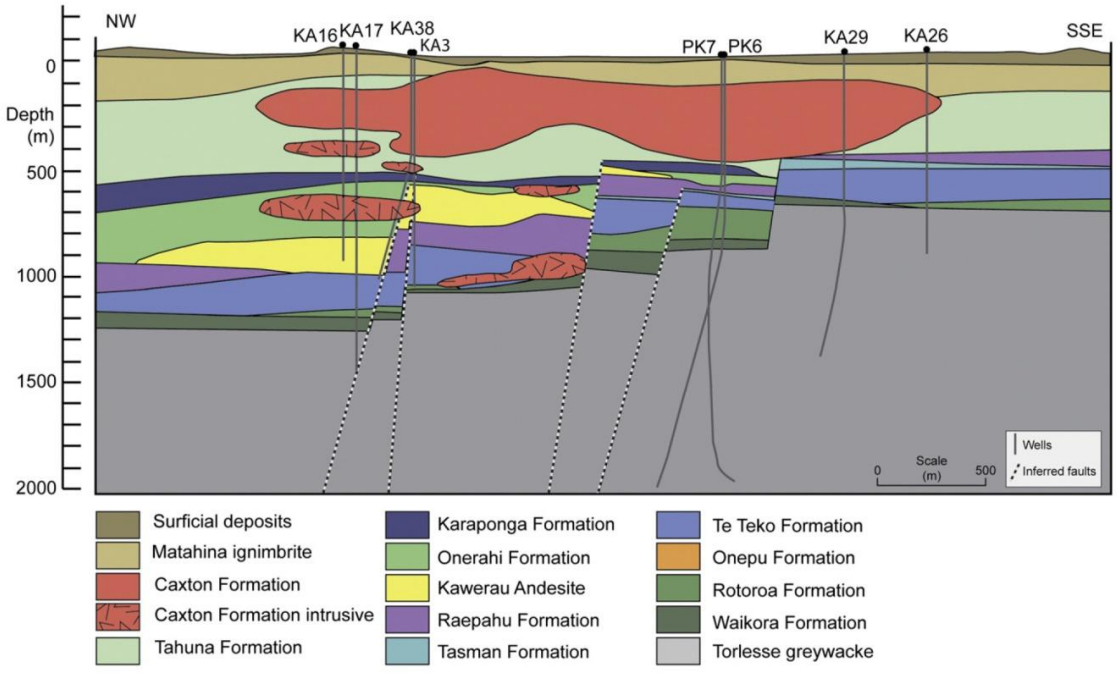

Figure 1.6: Stratigraphic cross-section from north-northwest to south-southeast across the Kawerau Geothermal Field. Wells near the section are shown by a solid and inferred faults (dashed lines) are shown as dashed lines (from Milicich et al., 2016).

Formation	Lithology	Thickness
Recent alluvium	Peat deposits; sands and gravels; unconsolidated pyroclastics (incl. Whakamana Breccia, Rotoiti Breccia)	10–50 m
Hydrothermal eruption breccias	Hydrothermal eruption deposits, from 14,500 and 9000 yr BP	1–4 & 2–10 m
Unconsolidated pyroclastics	Unwelded pumiceous pyroclastic flows and airfall tuffs	0–90 m
Onepu Formation	Twin surficial domes of rhyodacite (pl, qtz, pyx, hb, bt) and intrusive (porphyritic crystal-rich; corroded qtz, pl, mafics)	~200 m
Matahina ignimbrite	Partly welded grey-brown lenticulite & vitric tuff (pl, qtz, pyx)	10–410 m
Tahuna Formation	Crystal-rich, fine sandstone, siltstone, muddy lithic-breccia and unwelded pumice-rhyolite lapilli tuff	0–360 m
Caxton Formation	Buried domes of spherulitic and banded rhyolite (corroded and fractured qtz and pl) and intrusive (corroded and fractured qtz and pl, ±bt±amp)	0–450 m
Karaponga Formation	Partly welded crystal-lithic tuffs (pl, qtz±bt)	0–180 m
Onerahi Formation	Tuffaceous to muddy breccias and coarse tuffaceous sandstone	0–85 m
Kawerau andesite	Augite–plagioclase andesite flows, breccias and tuff (in south)	0–300 m
Raepahu Formation	Partly welded crystal-vitric tuffs (qtz, pl, bt, lithic-poor and qtz, pl, bt, ferromagnesians, lithic-rich)	0–165 m
Tasman Formation	Muddy breccia, sandstone and siltstone, but widely represented by reddish brown siltstone	0–25 m
Te Teko Formation	Partly welded grey crystal-vitric tuff (corroded qtz, pl, bt)	0–255 m
Rotoroa Formation	Tuffaceous sandstone, poorly sorted crystal and vitric, water-laid tuff, siltstone	0–200 m
Waikora Formation	Greywacke pebble conglomerate and minor intercalated tuff and siltstone	0–450 m
Greywacke basement	Weathered, sheared greywacke and argillite	–

Abbreviations used are pl = plagioclase; qtz = quartz; pyx = pyroxene; hb = hornblende; bt = biotite; and amp = amphibole.

Table 1.1: Summary of the stratigraphic units and lithologies in the Kawerau Geothermal Field (Milicich et al., 2016; petrographic and mapping studies). This table describes the typical lithologies and their thickness within TVZ.

The Modern TVZ not only provides a representative example of TVZ stratigraphy, but also contains most of the TVZ geothermal fields. The information about the position of the lithologies and the relationships between each other reported in the following paragraphs are derived from the study of extensive outcrops overall, quarry excavations and drill holes. The stratigraphic succession of this area can be described as distinct groups:

a. Greywacke basement

Greywacke type lithologies form the basement for the entirety of New Zealand and are generally composed of slightly metamorphosed, massive, well indurated, quartzo-feldspathic sandstones and minor interbedded mudstones. The grain size in the sandstones is variable, from medium to fine-grained, and lithic components are dominated by volcanic clasts (mostly andesite lava, rare rhyolite lava, and ignimbrite clasts) to fine-grained sandstone, and argillite (Mortimer, 1994; Wood et al., 2001; Adams et al., 2009; which are petrographic, geochemical and sedimentological studies, focused in North Island).

Tectono-stratigraphic terranes (Fig. 1.1 and Fig. 1.7) are divided in two main provinces. The Eastern Province is separated from the Western Province, Buller and Takaka Terranes (Paleozoic), by the Median Tectonic Zone (MTZ), which is a zone of Triassic-Cretaceous plutonic rocks (Bradshaw, 1993; Kimbrough et al., 1994; geochronological and geochemical studies in the TVZ). The Eastern Province comprises the eastern terrane group (composed of, from east to west: Torlesse, Waipapa, and Caples) which are greywacke-dominated turbidite sequences (Suggate, 1978; from mapping and geophysical surveys). A central arc terrane group (composed of, from east to west; Dun Mountain-Maitai, Murihiku, and Brook Street) lies between the MTZ and the eastern group. The easternmost, Maitai Terrane is composed of quartzose sediments while the others are composed of basic to intermediate volcanics and volcaniclastic sediments (MacKinnon, 1983; petrographic and geophysical work). All these terranes are >1.000 km in length and <150 km in width. With the exception of the Murihiku Terrane, Late Permian-Early Triassic and Late Triassic-Early Jurassic (Rangitata Orogeny Phase I) deformation/metamorphism have obliterated good stratigraphic sections.

The basement rocks (pre-100 Ma) of the North Island all fall within the Eastern Province, a Carboniferous-Cretaceous mobile belt made up of several tectonostratigraphic terranes (Bishop et al. 1985; geophysical study). With respect to the contemporary continental margin, an outer group of three terranes (from east to west, the Torlesse, Waipapa, and Caples Terranes) represent accretionary wedge environments. The easternmost, Torlesse (composite) Terrane, is dominated by quartz-rich turbidites with plutonic granitoid compositions, whilst the Waipapa and Caples Terranes show increasing felsic to intermediate volcaniclastic character (MacKinnon, 1983; petrographic and geophysical work).

The greywacke basement within the TVZ is composed of two terranes: Torlesse and Waipapa. The constituents of the Torlesse (composite) Terrane are the Rakaia Terrane, which consists of mostly Permian and Triassic rocks, the Kaweka Terrane (Jurassic), and the Pahau Terrane (Jurassic - Cretaceous).

The three terranes are elongated in a NE-SW direction except for the Rakaia which is found only at the southernmost point of the North Island in Wellington.

Both Rakaia and Pahau Terrane greywacke-dominated rocks formed in an accretionary wedge, with structurally complicated mid-fan, turbidite successions imbricated into 1-5 km thick packets along narrow (0.1-1.0 km) ductile zones (Begg & Mazengarb, 1996; mapping and geophysical studies in Eastern Province, South Island). Deformation and metamorphism (prehnite-pumpellyite to pumpellyite-actinolite facies; Mortimer et al., 1993; obtained from petrography and geochemistry) are related to tectonism in the growing accretionary prism, assigned to the Jurassic-Cretaceous, Rangitata Orogeny (Bradshaw et al., 1981; mapping and geophysical work in North Island).

Detailed geochronological studies of the Torlesse Supergroup metasediments indicate regional metamorphism and subsequent uplift and cooling in the latest Triassic to Late Jurassic and, more locally, in the Early Cretaceous (Graham & Korsch, 1989; Graham & Adams, 1990; Adams & Graham, 1996). Throughout the North Island Torlesse, fossil localities are rare, and most commonly indicate general Early Cretaceous to Late Jurassic ages, rare Triassic, and very rare Permian ages (Fig. 1.7) (Grant-Taylor & Waterhouse, 1963; Stevens, 1963; Speden, 1976; Grant-Mackie, 1978; Te Punga, 1978; Campbell, 1982; Campbell et al., 1993; petrographic work).

The Permian-Jurassic Waipapa Terrane extends from Stephenson Island in the extreme North till Taumarunui area, Southwest of Lake Taupo. There is a two-fold subdivision: Hunua Facies, which is composed of structurally complex, thin-bedded, fine-grained, volcaniclastics, sandstone-siltstone successions with abundant melange and occasional chert and basalt, and the Morrinsville Facies, which is structurally simpler, coarse, volcaniclastics, sandstone, without chert or basalt components (Kear, 1971; Black, 1994; petrographic studies and geochemical techniques) but including some conglomerate units. Within the Waipapa Terrane the metamorphic grade decreases from west to east, rather irregularly, from pumpellyite-actinolite to zeolite facies (Black, 1989; Black et al., 1993; geochemical techniques). Fossil localities, especially in the main clastic successions, are very rare (Fig. 1.7) and what has been observed provides

age constraints of Late Jurassic - Late Triassic (Spörli & Grant-Mackie, 1976; Spörli et al., 2007; geochronological and geochemical work).

The transition from Waipapa Terrane to Torlesse (composite) Terrane is not exposed though its exact location has been postulated in a number of studies. To the north, the terrane boundary is even more uncertain but clearly runs through the NE sector of the TVZ. In fact, it is inferred that the boundary between the two terranes may be close to or directly underneath the Kawerau Geothermal Field, as inferred from observations of geothermal wellbores (Adams et al., 2009; McNamara, 2014; borehole acoustic imaging).

Lithological and petrographic contrasts between the basement terranes are mappable. The Torlesse sandstones show rare argillite and volcanic fragments, as well as granophyre fragments and prehenite, chert fragments are present, and there is a widespread sericitisation. On the other hand, the Waipapa Terrane typically has often abundant argillite and intermediate volcanic rock fragments, granophyre is present and prehnite too, sericite is observed but not to the same extent as in the Torlesse rocks, and chert fragments are rare (Beetham & Watters, 1985; petrographic work, North Island).

Taking the Kaimanawa sandstones as representative example of the Torlesse greywacke, the overall composition strongly suggests derivation from a dominantly granitoid source, although other rocks, notably chert, argillite, and rhyolite (including ignimbrite), are represented among the lithic fragments. Although abundant granite source rocks are indicated by clastic minerals such as quartz, microcline, and biotite, some of the K-feldspar present is probably a cryptoperthitic variety more likely to be derived from shallow intrusive rocks and rhyolite. Any chert fragments present would tend to increase the silica content of the sandstone; argillite fragments, present though infrequent in most samples, would reduce the silica content slightly (Beetham & Watters, 1985; petrographic and geochemical works).

Typically, Waipapa terrane greywackes (Fig. 1.7) are characterised by abundant lithic fragments. Chemical analyses of representative rocks (Beetham & Watters, 1985) highlight the differences between the two greywacke terranes shown in petrographic

studies and reflect the high content of intermediate volcanic rock fragments in the Waipapa sandstones. Petrographic examination shows that fragments of granophyre or microgranite are also present, accompanied by clastic quartz, K-feldspar, and chloritised biotite. K-feldspar includes occasional microcline grains, so that granite was also likely among the source rocks for the sandstone, though less important than shallow silicic intrusives as a contributing source (Beetham & Watters, 1985).

Despite their compositional variations, both greywacke terranes present very low porosity and all permeability within them is thought to be fracture hosted (Wallis et al., 2012; McNamara et al., 2014; porosity and permeability measurements, TVZ). It is the fracture permeability in these basement rocks that allows them to host geothermal reservoirs e.g. Kawerau and Ohaaki Geothermal Fields. The very low permeability and porosity measurements obtained from the study of McNamara et al., (2014) are consistent with the hypothesis that fluid flow in New Zealand's greywacke basement is not controlled by pore space, but rather by structures such as faults and fractures. Major faults and fractures in the greywacke also facilitate flow of high-temperature fluids into the overlying Quaternary succession (Milicich et al., 2016; geochemical techniques).

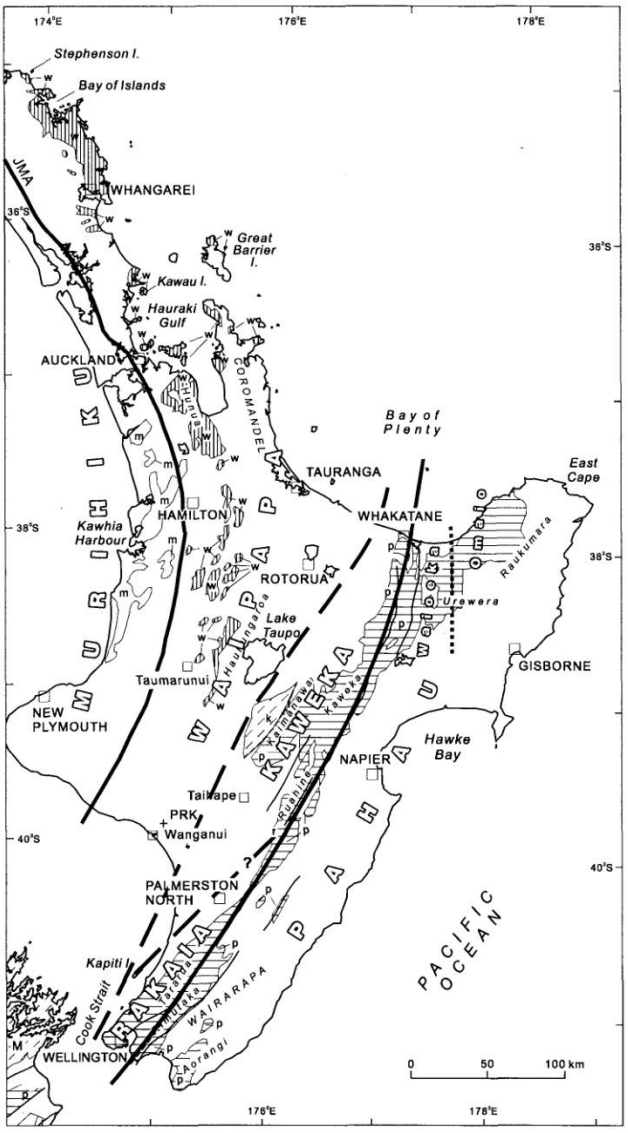

Figure 1.7: Geological map of Torlesse Supergroup and Waipapa Group in the North Island, New Zealand. It shows a suggested terrane configuration. Surface, or probable subsurface, terrane boundary faults shown as solid lines; where these are uncertain, the terrane limits are illustrated with dashed lines (from Adams et al., 2009).

b. Reporoa Group

In the TVZ the greywacke basement is overlain by the Reporoa Group. This stratigraphic unit consists mainly of rhyolitic ignimbrites (1.45 Ma till ~710 ka). These ignimbrites can be welded to strongly welded, dark to pale gray colored; usually they are fine-grained, crystals rich, vitrophyric, and contain pumice (Fig. 1.3) (Wilson et al., 1986; Grindley et al., 1994; Wilson et al., 2010; from petrographic studies).

c. Whakamaru Group

The Whakamaru Group, which overlies the Reporoa Group, is a useful marker horizon with which to spatially and temporally divide the geological history of TVZ for two reasons: first, these ignimbrites share easily identifiable petrographic and lithological features, such as Paeroa ignimbrites (Wilson et al., 1986; Keall, 1988; Brown et al., 1998; petrographic and geochemical work); and second, the older (~349 ka) and voluminous (>1500 Km^3) ignimbrites of the Whakamaru Group are widespread across the central North Island (Down et al., 2014; petrographic study).

The Whakamaru Group consists of massive to eutaxitic, rhyolitic ignimbrite, variably welded and columnar jointed. The rocks are quartz crystal rich and also contain plagioclase, biotite, also hornblende, pyroxene, magnetite and ilmenite. Pumice content is variable, from rich to poor, as is the occurrence of lithic fragments. Typically this Group presents a fine-grained matrix (Wilson et al., 1986; Keall, 1988; Brown et al., 1998; petrographic studies). The Paeroa Subgroup (~339 ka) is typically more strongly welded than other Whakamaru Group ignimbrites.

d. Huka Group

The Huka Group follows chronologically after the Whakamaru Group and is composed of a series of rhyolitic ignimbrites interspersed by breccias, and interbedded with lacustrine sediments, or other pyroclastic deposits (Fig. 1.3). These formations date between ~330 ka and ~25.4 ka. The Group is lithologically very variable: from unwelded to strongly welded, different geometries and relations between the layers (massive to parallel bedded), show a wide range of colors; and contains variable amounts of pumice and lithic fragments (Down et al., 2014; petrographic study).

e. Surficial deposits

Early deposits dated around 25.4 ka, consist principally of the unwelded Oruanui and Taupo Formation ignimbrites, with minor ash fall deposits and lacustrine sediments (Manville, 2001; Wilson, 2001; Manville and Wilson, 2004; Wilson et al., 2009; petrographic studies).

1.2. THE TVZ AS A GEOTHERMAL CENTRE IN NZ

Geothermal exploitation in the TVZ consists of 25 distinct geothermal fields, and a number of surface features (Fig. 1.1). Many of these geothermal fields have been explored to some degree by drilling wells and, in those fields that have been developed for energy production wells can reach depths of up to ~3.5 km. In the Kawerau Geothermal Field for instance, more than 70 wells have been drilled to date for various purposes, despite that no more than 6 – 7 wells are ever in production simultaneously. Indeed, many of the older wells are now used for field monitoring or have been plugged and abandoned (Milicich et al., 2016).

The high heat flow (4200 ± 500 mW/m^2) controlled by hydrothermal convection (an example in Fig. 1.8) and concentrated in the TVZ geothermal systems, is calculated to be around four times higher than the average heat brought to the surface by volcanic eruptions (Hochstein 1995). On the order of 10^8 m^3 of 250°C fluid is released from the geothermal system every year through the 100-km long Central TVZ segment (Sibson & Rowland 2003).

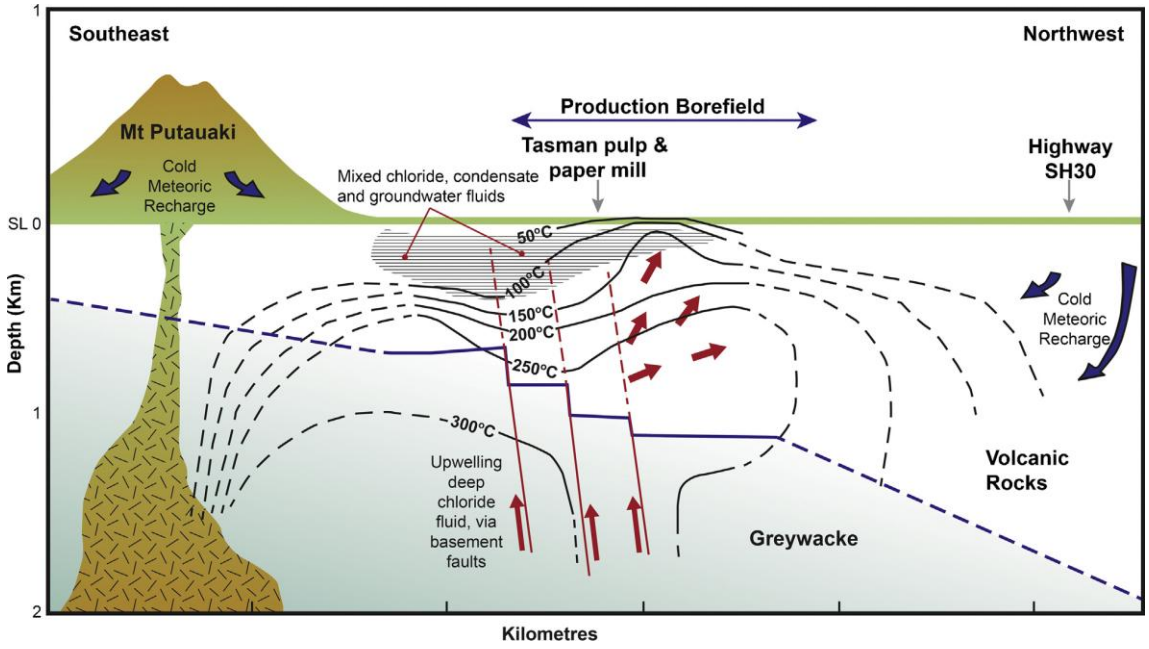

Figure 1.8: Conceptual model of the Kawerau Geothermal Field (after Christenson, 1997 and Holt, 2007); (from Milicich et al., 2016).

1.2.1. HOW GEOTHERMAL FIELD ARE DEFINED - RESISTIVITY MAPPING

Using electrical resistivity methods, twenty-three active and two extinct geothermal fields have been recognized inside the rhyolite-dominant area of the TVZ (Bibby et al. 1995). Low resistivity zones (approximately < 30 Ω) are associated with geothermal fields, active or extinct, even if the devitrification at ambient temperatures within ignimbrites older than approximately 1 Ma also reduces resistivity considerably (Bibby et al. 1999). The boundaries of most of the geothermal systems are typically characterized by a clear resistivity contrast at depths of 1–2 km, which suggests that the hot geothermal fluid may rise from the depth as an almost vertical column (Rowland and Sibson, 2004).

There are two NE–SW trending, extended zones of low resistivity from the Taupo Caldera to the Okataina Caldera (Fig. 1.9). These two low resistivity belts confine densely faulted rift segments, which display only minor geothermal activity. Zones of low resistivity also trend perpendicular to the rift axes, which is inferred to coincide spatially with rift accommodation zones (Wan & Hedenquist, 1981; Cochrane & Wan, 1983; Rowland and Sibson, 2004).

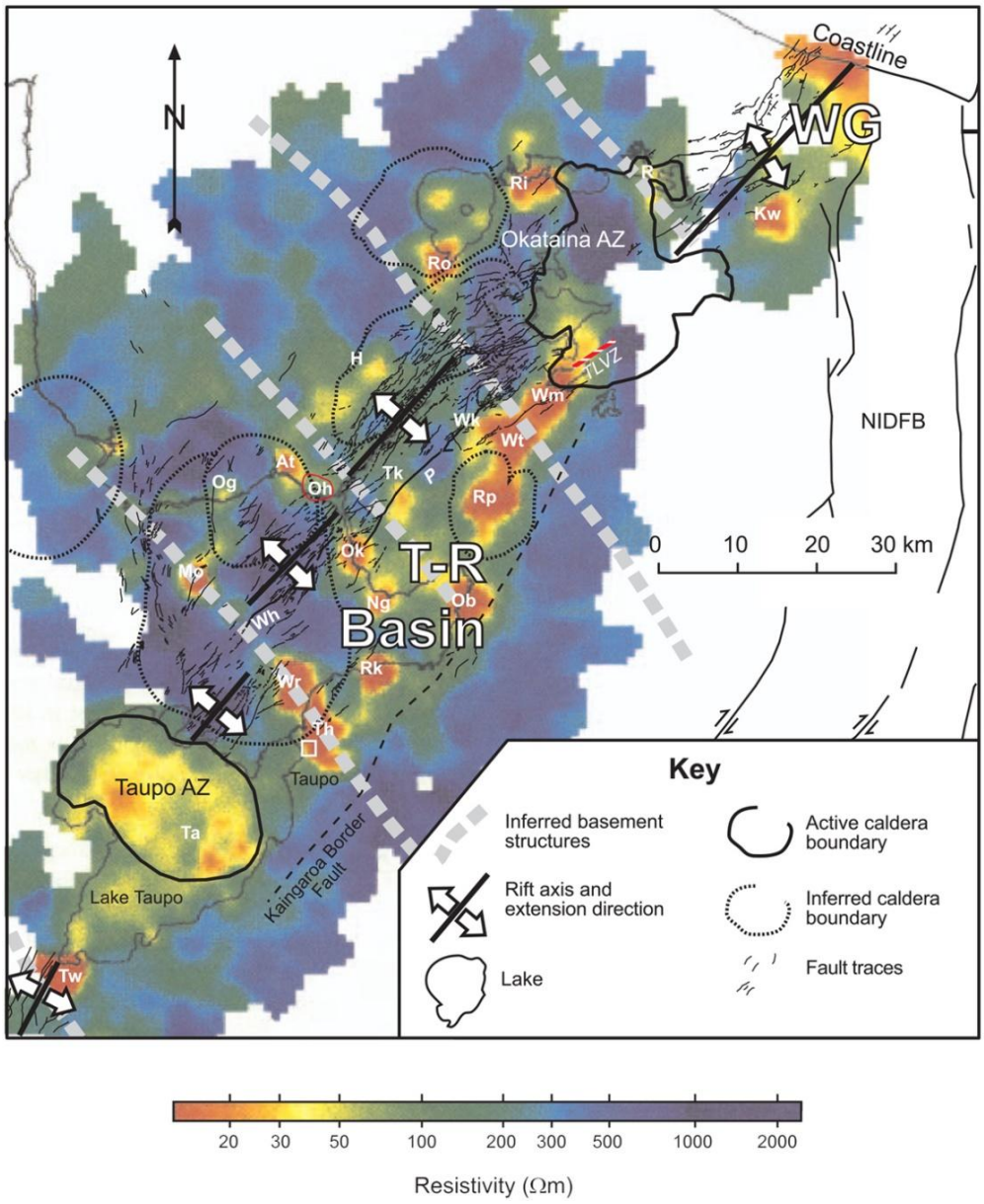

Figure 1.9: The rift position, its axis oriented in a NE-SW trend, is shown with a perpendicular extension direction. The electrical resistivity of the TVZ (after Stagpoole & Bibby 1998) in relation to rift segments, accommodation zones, inferred basement structures (after Wan & Hedenquist 1981), and inferred and active caldera boundaries (after Nairn et al. 1994) are also illustrated. Geothermal fields, indicated by low resistivity (color-coded red), are labelled if referred to in text: At, Atiamuri; H, Horohoro; Kw, Kawerau; Mo, Mokai; Ng, Ngatamariki; Oh, Ohakuri (extinct); Ob, Ohaaki-Broadlands; Ok, Orakeikorako; R, Rotoma; Ri, Rotoiti; Rk, Rotokawa; Rp, Reporoa; Th, Tauhara; Ta, Taupo; Tk, Te Kopia; Tw, Tokaanu-Waihi; Wm, Waimangu; Wk, Waikite; Wr, Wairakei; Wt, Waiotapu. Additional labels: T-R Basin, Taupo-Reporoa Basin; WG, Whakatane Graben; P, Paeroa Fault; Wh, Whakaheke Fault; TLVZ, Tarawera Linear Vent Zone; NIDFB, North Island Dextral Fault Belt. From: Rowland and Sibson (2004).

1.2.2. HOW GEOTHERMAL FIELD ARE DEFINED - HYDROLOGY MODELS

Hydrological models form the basis for deciding suitable areas to drill geothermal wells. The main factors affecting fluid flow paths include the nature of the heat source (for instance if it is an isolated pluton or a sill complex) (Cathles et al., 1997), topography (Healy & Hochstein, 1973; Simmons et al., 1993), and permeability, which is rarely isotropic over the spatial and temporal scales of interest in a geothermal regime.

In a hydrothermal environment, the bulk permeability of a rock-mass is constantly changed by fracturing, brecciation, and cementation from hydrothermal precipitation. The bulk permeability is dictated by:

- The intrinsic permeability of the lithologic units, which for consolidated rocks extends over 13 orders of magnitude (Brace, 1980).
- A component of anisotropy from rock layering and existing fracture sets;
- Structural components affecting permeability like faults, fractures, and dykes that were formed or emplaced in the prevailing stress field, and remained active during the period of hydrothermal fluid flow (Barton et al. 1995; Sibson 1996).

Faults may act as impermeable barriers to cross-fault flow or as high permeability conduits; while their permeability relative to the host rock is probably time dependent, varying with displacement, host lithology, and hydrothermal cementation (Sibson, 1994).

Globally, high-temperature geothermal regimes are generally associated with Quaternary to recent silicic or andesitic volcanism in districts of active extension or transtension. An excellent example is the TVZ (Bibby et al., 1995). The actual hydrology of the TVZ is linked with the geological-tectonic situation; in fact the TVZ was developed inside the Mesozoic basement assemblage of metasedimentary rocks

over the last 2 Ma and in its modern form (past 350 ka) corresponds with a structurally and magmatically segmented rift system (Wilson et al., 1995; Rowland & Sibson, 2001).

In the TVZ, faults and fractures definitely affect flow paths at the scale of the geothermal reservoir dividing the shallow hydrology in compartments or providing pathways for the flow. In turn, the flow through fractures appears to be important at depth, locally within cover sequences, and when initial intergranular percolation networks have been reduced beneath a critical level by hydrothermal precipitation and cementation. Hydrothermal alteration is pervasive in the upper part of the TVZ geothermal systems but decreases dramatically with depth corresponding to a change in lithology from porous breccia to tight greywacke. Inside the lower part, some extension fractures catch drusy apertures gaping up to 20 cm (Rowland & Sibson, 2004**).**

1.2.3. CONTROLS ON GEOTHERMAL FLUID / HEAT FLOW

Geothermal fluid flow, and therefore the heat flow, travels through the TVZ geothermal systems via a mixture of lithological porosity and secondary permeability, for instance faults and fractures.

The crustal assembly of rocks within the central TVZ is assorted but can be grouped into two contrasting packages: basement rocks and a Quaternary cover sequence (Roland and Sibson, 2004). Most of the geothermal energy production in the TVZ derives from volcanic/volcano-sedimentary aquifers (Table 1.2) deposited since the Whakamaru ignimbrites eruption at 330 ka (Wilson et al., 1995). The older TVZ strata between the Whakamaru ignimbrites and the basement are poorly known, but they can act as containing units that are lithologically similar to the shallow aquifers (Brathwaite et al., 2002). Porosity, as the permeability, is an essential property of reservoir rocks in geothermal fields. The pores between (and within) minerals or rock grains provide storage space for fluids.

Porosity can be described as primary and secondary. The primary porosity in volcaniclastic and sedimentary rocks is formed by the original spaces between mineral

or rock clasts. The secondary porosity comes from the leaching of unstable minerals during the hydrothermal alteration, for instance in the partial replacement of calcic plagioclase by adularia and orthoclase (Brathwaite et al., 2002).

The same porosity classification used for hydrocarbon reservoir rocks can be utilized in the study of geothermal reservoirs. Therefore porosity can be divided into macroporosity, pore spaces >16 μm, and microporosity, pore spaces <16 μm. The macroporosity corresponds to the intergranular holes. The microporosity is instead composed of micropores in clay minerals, for example illite and chlorite. The intercrystalline porosity is identified as micropores in clay minerals, for instance like in illite and chlorite, but it may not be significant to provide to have permeability because of the small size of the pores and their lack of connectivity (Brathwaite et al., 2002). A further contributor to the secondary porosity in the basement rocks are microcracks, which are defined as discontinuous fractures having less than 20 mm length and less than 0.5 mm in width. They commonly occur on a grain scale. Thermal cracking can produce these features, which has been accredited to several processes: the different thermal expansion of minerals, the temperature gradients induced as a function of heating rate, anisotropic thermal diffusivity of minerals, the bursting of fluid inclusions, mineral decomposition, and devolatilization (Cooper and Simmons, 1977; Wong and Brace, 1979; Lo and Wai, 1982; Keshavarz et al., 2010; Heap et al., 2012). Although the intrinsic porosity of rocks is very important for permeability, often it is not sufficient to ensure the exploitation. Therefore, in order to produce enough permeability to maintain the production, geothermal wells must intersect fractures and faults. However, faults and fractures are subject to cementation and clogging and consequent decline in productivity. So the ideal circumstances for the geothermal wells occur when the faults or other extensive fissures are located in porous strata with high storage capacity and extensive micropermeability (Brathwaite et al., 2002).

In TVZ, the greywacke sandstone basement rocks appear to have an intergranular porosity near zero because of the induration due to metamorphism and alteration. Samples of greywacke basement rock from Kawerau and Ohaaki Geothermal Fields show that the spaces between mineral and lithic grains are filled with a recrystallized matrix of illite and chlorite. However, intergranular porosity is locally

present in the conglomerates of the Waikora formation at Ohaaki, and siltstone clasts in tuff from the Ohakuri Group. In the volcanic and volcaniclastic lithologies of TVZ, secondary pore spaces of significant size consist of leach cavities in calcic plagioclase and primary mafic minerals and of vugs associated with vein or cavity filling by hydrothermal quartz or epidote (Brathwaite et al., 2002).

In Table 1.2 representative examples of porosity are given for different lithologies of TVZ. It is possible to see the significant difference in porosity between the greywacke basement (Torlesse) and the others.

	Post-330 ka Aquifers		330 ka	Pre-330 ka Formations		Torlesse "basement"		
	Waiora Formation	Rautawiri Breccia	Rangitaiki Ignimbrite	Ohakuri Group	Waikora Formation	Ohaaki Axial-A	Kawerau Waioeka	Surface outcrops
%	33.0	24.9	13.2	20.9	14.5	6.5	7.2	1.7
SD	8.1	7.05	7.7	6.8	6.6	2.7	4.5	0.75
N	64	124	65	33	25	22	24	13

Table 1.2: Porosity (%) is shown of some Ohaaki Formations, Kawerau basement and surface outcrops. SD = standard deviation; N = number of analyses (from Brathwaite et al., 2002).

As the intrinsic permeability inside the basement greywacke is too low to satisfy the condition for a hydrothermal convection (McNamara et al., 2014) fluid must move through alternate pathways. For instance, greywackes drilled beneath Kawerau and Ohaaki-Broadlands geothermal fields host abundant micro-fractures and are pervasively altered; permeability seems insufficient to sustain geothermal production wells apart for where the drilling has intercepted hydraulically conductive faults, as in the Kawerau field (Wood et al., 2001; Wallis et al., 2012). This observation carries the result that convective flow systems extending into the basement rocks need to utilize structural permeability in the form of macroscopic fault–fracture networks. Two positive correlations between fracture character and permeability were recognized in the KA50 (Kawerau's well) data (Wallis et al., 2012):

1) The flows in the well are located at the same depths of fractures with large apertures.

2) The fractures that intersect each other on the borehole wall are more densely distributed in permeable zones.

The permeability of shear fractures have been demonstrated by experimental and theoretical studies to be highly related to fracture aperture (Barton et al., 1995). In their study of deep geothermal wells in the Wairakei Geothermal Field, McLean and McNamara, (2011) verified that the largest apertures in the fractures could be correlated with the existing feed zones.

Looking on the larger scale, since the convection probably extends through the whole depth of the seismogenic zone, which reaches to depth between 6 and 8 km, fluid flow through fractures in the basement rocks has to contribute to the bulk permeability of the TVZ. From borehole measurements of low-porosity bedrock zones it has been noticed that hydraulically conductive fractures are those that are perfectly oriented for a possible reactivation of the shear fractures in the prevailing stress field (e.g. Barton et al., 1995; Ito & Zoback, 2000; Townend & Zoback, 2000). However, any hydrological mark of structurally controlled fluid flow at depth could be masked by scattered flow inside the strongly permeable pyroclastic cover rocks, with a level of masking that is function of the basin depth and average intergranular porosity. For instance, the superficial hydrology of geothermal systems inside the Taupo-Reporoa Basin, which encloses a thick (<5 Km) sequence of poorly consolidated pyroclastic and volcaniclastic material (Risk et al., 1999), is clearly not controlled by rift faults. Instead, in the Kawerau geothermal system, some production wells are fed from faults in the greywacke basement, showing the importance of the structural control at depth (Wood et al., 2001).

Several studies have been made on the fracture and fault systems in the TVZ geothermal fields and characterise them in order to understand their contribution to geothermal fluid flow. These studies incorporate various techniques from active fault mapping, borehole televiewer (BHTV) logging, and earthquake location studies (McLean and McNamara, 2011; Wallis et al., 2012; McNamara et al., 2015; McNamara

et al., 2016). Direct study of the structural character of basement greywacke that hosts geothermal systems is rare and in restricted to a study of two BHTV logs acquired in the Kawerau Geothermal Field (Wallis et al., 2012). From this investigation, it was noted that:

a) dominant fracture orientations matched the regional structural trend, but subordinate fracture orientations depended on the proximity of the greywacke to modeled, variously oriented, large scale faults;

b) there is a significant difference in fracture aperture above and below ~2640 meters depth such that deeper fractures tended to have larger apertures likely related to the fact that the greywacke basement unit at these depths contained less argillite and more sandstone below 2640 meters.

This lithological control on fracture character, and thus the permeability, is also evident in similar outcrops. The coastal section at Kuaotunu displays promontories that are dominated by thick sandstone sequences and are geographically divided into bays formed where the basement rocks are incised and when the lithology is dominated by argillite or interbedded argillite-sandstone. This is expected due to the greater resistance to the erosion of the huge sandstone units. Quartz filled fractures usually occur as relatively microcrystalline veneers on sheared surfaces in argillite, while in the sandstone-dominated rocks, quartz filled fracture are often wide. This means that even if both lithologies hosted the hydrothermal fluid flow, the permeability was higher in the sandstone (Wallis et al., 2012). This demonstrates how the lithology can influence the type of brittle failure occurring and thus the rocks permeability. The higher the tensile strength of the material is (for example the greywackes) the more likely it will deform via opening fractures. The lower tensile strength the material has (like the argillite), the easier is to deform as discrete narrow slip planes (for instance fractures filled with quartz veneers).

1.2.4. ROCK PROPERTIES OF GEOTHERMAL RESERVOIR ROCK

1.2.4.1. Seismic wave velocity

Geophysical methods provide essential information to establish optimal sites for the exploitation of geothermal energy. Refraction seismic profiling and tomographic inversion techniques are used to find out the velocity structure, major faults with reduced velocity, and fluid-bearing horizons (Baechler et al., 2003).

An example of inversion technique is the one applied by Wu and Lees, (1999a) in the geothermal field at Coso (California). This inversion method for P wave anisotropy has been applied to high precision microseismic travel-time data. The direction-dependent P wave velocity and hence its perturbation are represented by a matrix instead of a scalar. The resulting anisotropy distribution was employed to estimate the variation in crack density, stress distribution, and permeability inside the geothermal field.

However, the combination of velocity tomography with preexisting or new seismic reflection data can considerably improve the knowledge of the structure and composition. Deeper levels in the geothermal system can be determined by seismic tomography in the case that seismic reflection data are not enough to have a clear description. For instance, the identification of deep faults which are fundamental for the geothermal system because, as already said in this work, they can carry up deeper and hotter fluids which may represent a bigger heat source (Baechler et al., 2003).

There are several ways to utilize seismic waves to scan the subsurface, and the use of different techniques and the combination of the seismic velocities with other data can be very useful. An example of these techniques can be the tomography, which can be joint with thermal modeling utilizing the relationship between seismic velocity and temperature (Schoen, 1996). The concept of such combined analysis would be to verify if the velocity structure reflects variations in the temperature field as a significant achievement for the geothermal exploration (Bauer et al., 2010).

Usually, studies about geothermal fields are conducted analyzing regional earthquake data to determine three-dimensional V_p, V_p/V_s. This procedure consists of

associating earthquake hypocenters and focal mechanisms of faults with the study of the region. It is useful to characterize the size, the shape, the amplitude anomalies of the velocity structure at depth and their location relative to the geothermal field. From this, three-dimension model and refined seismicity pattern for the whole study area can be determined (Hauksson et al., 2007).

Another case where V_p and V_s data are very useful is to study anomalous patterns in relation to the geothermal field. Sometimes anomalies allow understanding of reservoir depletion and it is possible to monitor the status of reservoirs using these techniques (Silas M. Simiyu, 2000).

The TVZ seismicity defines a seismogenic zone up to ~6-8 km deep, by including widespread episodic seismic swarms and occasional moderate to large normal slip earthquakes (M_L < 6.5) (Bibby et al., 1995; Bryan et al., 1999; Sherburn et al., 2003).

To sum up, seismic wave velocities play a fundamental role in geothermal field studies, not only to support other parameters and interpretations, but overall to acquire exceptional 3D models of the subsurface reaching to several km depth and showing, with accuracy, the different velocity gradients in relation to different lithofacies.

1.2.4.2. Strength

The tensile strength for TVZ rocks can be derived from laboratory test conditions; pyroclastic and sedimentary rocks have values ≤5 MPa, rhyolite domes could range in tensile strength up to 10 MPa, and intact greywacke could reach 15 MPa (Lockner, 1995).

TVZ basins' weak and low cohesion rocks control the mechanical response of the crust to extension on the rift segments. The mechanical response is usually in the form of open fractures, mainly limited to rhyolite domes and competent ignimbrite sheets, greywacke basement rocks, and rocks strengthened by silicification. Rift segments in the TVZ present optimally oriented normal faults and few extrusive dykes and fissures (Rowland and Sibson, 2004).

Although TVZ normal faults usually appear oriented for the reactivation in the prevailing stress field (Rowland & Sibson, 2001), localized restoration of cohesive strength by cementation is estimated to be very significant (Sibson & Rowland, 2003).

1.2.4.3. Thermoelastic properties

The behavior and the influence of a thermal gradient on a geothermal source can have a significant impact on the heat flow, stress conditions, permeability and commercial potential of a geothermal reservoir. The induced or natural thermal gradients can effect thermal cracking in the rocks (David et al., 1999) which can result in the reduction of rock strength (Heap et al., 2013b) and a rise in permeability (Faoro et al., 2013).

Meticulous studies on the conditions that lead to the beginning of thermal cracking in a geothermal reservoir are indispensable for the most advantageous utilization of the resource, for considerations about the wellbore stability, for predicting the reservoir response to stimulation procedures (Zoback et al., 2003; Ghassemi and Zhang, 2004; Grant and Bixley, 2011). Thermal cracking, due to the differential rise of minerals volume under the influence of the temperature, is an important process that can be also linked to different geological phenomena, such as: magmatic dyke emplacement, cooling of magma and lava bodies, and contact metamorphism.

To promote the understanding of the thermo-mechanical behavior in a geothermal reservoir, it is necessary to quantify the thermal properties of the reservoir rocks. The optimization of a high-enthalpy geothermal energy scheme is greatly reliant on the natural permeability of the system (Grant and Bixley, 2011). However, the disturbance of the natural situation of the reservoir by drilling and withdrawing heat and fluids changes the state of the reservoir in relation to pressure and temperature (Ghassemi and Zhang, 2004). With change in temperature, the host rocks of the reservoir are influenced by thermal gradients which can consequently give rise to thermal cracking, intensifying the development of permeability. These thermal gradients cannot be only caused by drilling fluids interacting with hot reservoir rocks (Brudy and

Zoback, 1999), but also by underground injections of depleted power plant fluids (Grant and Bixley, 2011) and targeted injections of cold water (Ghassemi and Zhang, 2004). Therefore, thermal cracks may result in the improvement of permeability of the wells over both short and long time scales (Axelsson and Thórhallsson, 2009; Grant et al., 2013). When cooling fluids are injected to the reservoir rocks, rocks thermally contract producing tension, and new fractures can be formed (Brudy and Zoback, 1999; Tarasovs and Ghassemi, 2012). The targeted injections of cold fluids usually used in the geothermal industry has been well documented as re-opening and expanding of already existing fractures and determining the creation of new fractures (Kitao et al., 1990; Flores-Armenta and Tovar-Aguado, 2008; Axelsson and Thórhallsson, 2009; Grant and Bixley, 2011).

Briefly, it is important to obtain data on the thermo-elastic properties of the rocks in a geothermal reservoir because it is possible to plan where and how to make thermal cracks. These cracks are responsible for changes in the reservoir rock physical properties such as the attenuation of acoustic velocities (Vinciguerra et al., 2005; Fortin et al., 2011; Heap et al., 2013a), the increase in porosity (Bauer and Handin, 1983; David et al., 1999; Chaki et al., 2008), the increase in permeability as a result of microcracking (Heard and Page, 1982; Darot et al., 1992; Fortin et al., 2011; Nara et al., 2011; Faoro et al., 2013), the degradation of rock strength (Balme et al., 2004; Keshavarz et al., 2010; Heap et al., 2013b; Patel et al., 2013); and the considerable influence on the thermal expansion coefficient (Cooper and Simmons, 1977; Lo and Wai, 1982; Lin, 2002).

CHAPTER 2:
TECHNIQUES AND METHODS

This part of the thesis will explain the techniques and methods utilized to acquire the data and the results of the study of the physical properties of the greywacke and their behavior under particular conditions.

This chapter is divided in three sections: the first section will describe the preparation of the samples, from the quarry-derived block of rock to the production of the cores, in relation to the kind of test where they will be involved, from strain gauged uniaxial samples to jacketed triaxial samples.

The second section will illustrate the apparatus with which the experiments have been done. Some of these rigs were designed and made by Prof. Dan Faulkner, so their function will have more detailed explanations. The same is true for the seismic equipment, which is a fundamental part of this project. The jig for Brazilian tests was designed by the author of this thesis, will be described in detail. Less detailed descriptions will be made for standard commercially available devices, such as for example the SEM and the thermo-analysis machines.

Finally, in the third section the methodologies followed in the experiments will be explained, describing the data analysis as well as the data collection, and the reason why these procedures have been chosen and how they may affect data quality.

2.1. SAMPLE PREPARATION

In this section the procedure to make the greywacke cores and prepare them to be tested will be described. A wide range of techniques have been used in this project, meaning that the measurements need different diameters of cores. From the standard core used for this project, which is 20 mm diameter and 50 mm length, the dimensions varied to shorter cores, thinner and shorter cores, shorter and fractured cores. Finally, thin sections of the materials used in experiments, before and after the failure, were made for microstructural analysis. The application of the strain gauges to the sample, and their wiring configuration will be described.

The samples tested for this work come from Taotaoroa Quarry (TT), and belong to Waipapa Terrane. Taotaoroa Quarry (WGS84: 37°54'20" S - 175°38'14" E) is located between the town of Cambridge and the town of Matamata, around 8 km north-west from Karapiro Lake. Thin sections from other sites were used only for petrological observations: Waotu Quarry (WA), at ~15 km W from the town of Tokoroa (WGS84: 38°11'48" S - 175°40'55" E), with greywackes belonging to Waipapa Terrane; Blue Rock Quarry (BR), at ~2 km S-SE from the town of Whakatane (WGS84: 37°59'35" S - 176°59'54" E), which greywackes belong to Torlesse Terrane (Fig. 1.1).

2.1.1. CORING OPERATIONS

The laboratory samples were cored from a block of Waipapa greywacke from Taotaoroa Quarry (Fig. 2.1a), using a diamond tipped coring drill with an internal diameter of ~ 20 mm (Fig. 2.1b) mounted on a pillar drill (Fig. 2.1c). The machine is configured for minimal vibration to reduce the damage to the cores. Using a water swivel that uses water as a coolant during the cutting also reduces dust production. The ends of the cores were cut to approximate the length using the diamond blade saw (Fig. 2.1d). Samples were squared using a diamond grinder (Fig. 2.1e-f) so that the ends were squared to the sample long axis within a tolerance of 0.01mm or less, according to guidelines given by Paterson & Wong (2005).

Another type of sample was cored from the same block of greywacke rock in order to run the thermal analysis measurements (in order to determine the thermal expansion coefficient and the specific heat capacity). The core was produced using a diamond tipped coring drill with a diameter of ~ 6 mm (Fig. 2.2a) mounted on a drilling machine with similar characteristics to the previous one described in this paragraph. The ends of the cores were cut to approximate length using the diamond blade saw and the samples were squared using a small diamond grinder (Fig. 2.2c).

Figure 2.1: a) Greywacke rock and cores; b) Rock drilling; c) Pillar drill; d) Diamond saw; e) Grinder; f) Grinder detail: the core is held in the V-block, which is secured on a magnetic surface.

Figure 2.2: a) 6mm diameter core; b) Squared samples produced from the core in Fig. 2.2a; c) Grinder used to square these samples.

2.1.2. UNIAXIAL TESTS - CORE PREPARATION

Axial and radial strain gauges were glued to cores in order to measure the strain in the two directions. The strain gauges were linked to the strain gauge amplifiers by soldering the strain gauge wires to terminals glued on the core (Fig. 2.3).

The sample length was ~50 mm and the diameter ratio with the length was approximately 2.5:1, as suggested in Paterson & Wong (2005). Samples with this dimension ratio (2-2.5:1) ensure the stress and strain in the central portion of the plug are not affected by stress shadows produced by elastic mismatch between the rock and the loading platens (Paterson & Wong, 2005).

2.1.2.1. Strain gauges and the Wheatstone bridge principle

The strain gauges are employed to measure the strain and they were applied either 2 per core (one in axial position and one in radial position) or 4 per core (two in axial position and two in radial (circumferential) position). The "axial" type strain gauge has a length of 20 mm (PFL-20-11) while the "radial" strain gauge has a length of 10 mm (PFL-10-11). The use of 4 strain gauges rather than 2 is employed to measure the strain in two places on the core, rather than rely on a single measurement of strain (Fig. 2.3). In detail, PFL-10-11 measures the circumferential strain (radial strain), and it is positioned approximately in the middle of the core length, perpendicular to the axis of the core. The PFL-20-11 is positioned in a longitudinal (axial) way, parallel to the axis of the core. The strain gauges work on the basis of the Wheatstone bridge principle.

Figure 2.3: Greywacke core with 20mm diameter and ~50mm length. Axial and radial strain gauges and terminals were applied on it.

A Wheatstone bridge is an electrical circuit used to measure an unknown electrical resistance by balancing two legs of a bridge circuit, one leg of which includes the unknown component. R1, R2, R3 and Rx are resistors. R1 and R3 are resistors of standard and known value, while the R2 resistor is variable.

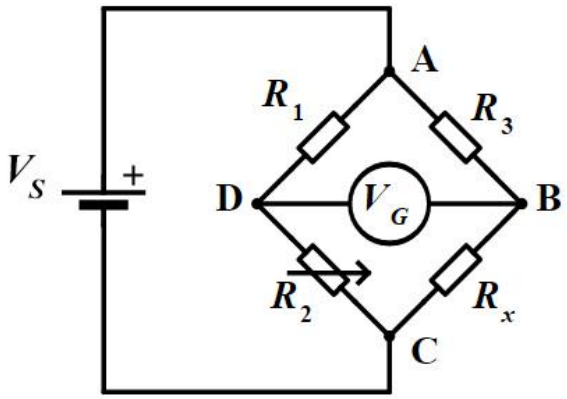

Figure 2.4: Electric scheme of Wheatstone bridge. A, B, C, D, are node points. R are resistors and R_X is the unknown resistance. V_G is the measured voltage and V_S is the supply voltage.

This circuit, constituted by four resistors, is powered by the voltage V_S. If the relationship of the two resistors of the known side (R2 / (R2 + R1)) is equal to the relation of the other two resistors of the unknown side (Rx / (Rx + R3)), the electric potential difference between the two intermediate points will be nullified. To perform the measurement, the R2 resistor is varied to obtain the balance point, namely when there is zero potential difference between B and D (Fig. 2.4). If the values of the resistors R1, R2 and R3 are known with great precision, the value of Rx can be determined with similar accuracy. Small changes in the value of Rx will break the balance and the variation in strain will be clearly identified by the instruments. In general, the Wheatstone bridge illustrates the concept of a difference measurement, which is extremely accurate.

The measured voltage V_G can be calculated as follow:

Equation 2.1:

$$V_G = \frac{V_S\, k\, \varepsilon}{4}$$

where:

V_G = measured voltage

V_S = supply voltage

ε = strain

k = gauge factor (calibration factor given by the operator in relation to how resistance varies with strain)

Therefore, from the Equation 2.1 it is possible calculate the strain:

Equation 2.2: $$\varepsilon = V_G \frac{4}{V_S\, k}$$

The amplifier used in this work is: "Strain gauge amplifier module type 628" manufactured by RDP with 1/4 bridge. Details about the types of strain gauges are reported in Table 2.1:

Gauge type	**PFL-10-11**	**PFL-20-11**
Gauge length	10 mm	20 mm
Gauge resistance	120 ± 0.3 Ω	120 ± 0.3 Ω
Gauge factor	2.12 ± 1%	2.13 ± 1%
Temperature compensation for	11 x 10^{-6}/°C	11 x 10^{-6}/°C
Transverse sensitivity	-0.5 %	-0.6 %
Test condition	23°C 50%RH	23°C 50%RH

Table 2.1: Parameters of the two strain gauges radial (PFL-10-11) and axial (PFL-20-11) used for the uniaxial tests. PFL-10-11 is the gauge horizontally positioned on the cores. PFL-20-11 is the gauge vertically positioned on the cores.

2.1.3. TRIAXIAL CORE PREPARATION: JACKETING

For the triaxial tests a greywacke core prepared as previously described for cores for the uniaxial tests was used, having the following dimensions: 20mm diameter and ~50mm length. In triaxial testing of rocks, the jacketing of the specimen in an impermeable jacket is a very important factor in the experimental conditions (Fig. 2.5 a-b). The jacket used here is a "Nalgene 180 PVC Tubing". It is needed to prevent the confining fluid from entering pores or cracks and its use greatly influences the strength. In general terms, its action is needed to enable the confining pressure effectively to

inhibit the opening of cracks or to slide on existing crack surfaces (Paterson & Wong 2005). Machined disks (with spiral patterns) were applied on the top and on the bottom of the jacketed core (Fig. 2.5 a-b) in order to help to evenly distribute the fluid pressure over the face of the sample.

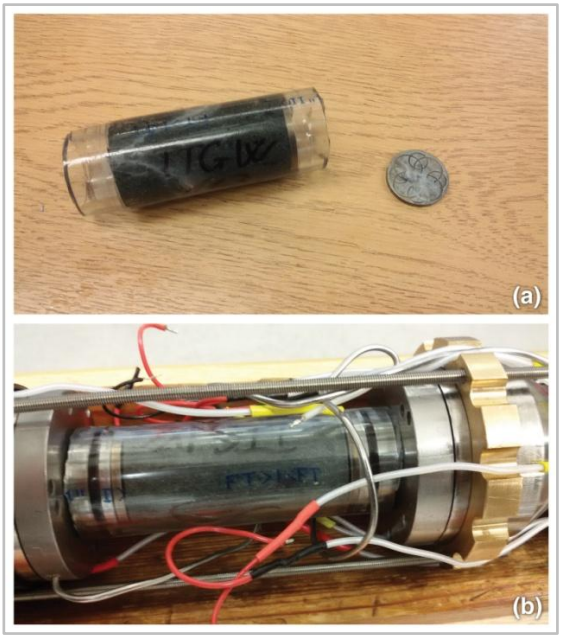

Figure 2.5: a) Jacketed core and porous disks; b) Jacketed core inside the sample assembly ready for triaxial test.

2.1.4. BRAZILIAN TEST DISK PREPARATION

The specimens for Brazilian tests were cut from the cores prepared for the uniaxial tests previously described, with the purpose of obtaining the required standard dimensions for this test. The standard specimen for the Brazilian test has to be a circular disk (cylinder) with a thickness-to-diameter ratio (t/D) between 0.2 and 0.75 (ASTM D3967-08). Therefore, the thickness of the disks is around 10 mm since the diameter of the disks is 20 mm (Fig. 2.6).

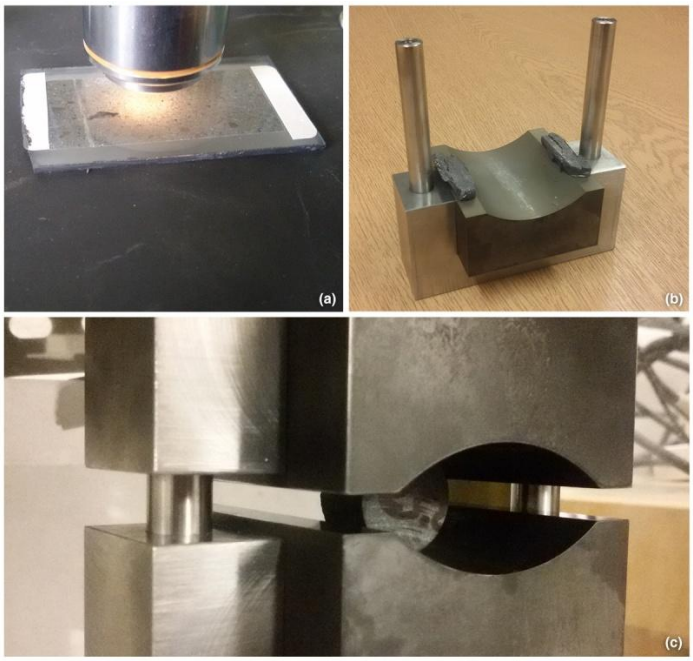

Figure 2.6: Disk inside the Brazilian jig during the test. a) Thin section of greywacke during microscope observations; b) Pieces of lead applied on the jig for the Brazilian test in order to reduce the stress on the disk upon failure. c) Greywacke disk inside the Brazilian jig during Brazilian test.

2.1.5. THERMAL DEFORMATION TESTS DISK PREPARATION

The specimens for thermo analysis have cylindrical shape with a 6 mm diameter and 5 mm length (Fig. 2.2b). They were cored and squared as described before (Section 2.1). To approximate the length they were cut using the diamond blade saw (Fig. 2.1d).

2.1.6. PERMEABILITY MEASUREMENTS THROUGH A SINGLE FRACTURE: SAMPLE PREPARATION

The jig for the Brazilian test was employed to prepare samples in order to measure the fluid flowing through a single fracture on greywacke disks with approximate dimensions of 20 mm x 30 mm. To make a central and extremely thin fracture through the disk (almost undetectable by the human eye), two pieces of lead were employed on the sides of the jig, between the two curved bearing blocks, to

support the load and reduce the stress on the disk at failure so that the fracture occurs in a slower way, avoiding a large crack (Fig. 2.6). Without the lead the loading apparatus elastically unloads when the sample fails and can produce widespread failure of the core. Next the fractured cores were jacketed with a "Nalgene 180 Polyurethane Tubing" (Fig. 2.5). Finally they were placed inside the sample assembly to proceed with permeability measurements.

2.1.7. THIN SECTIONS AND POLISHED BLOCKS

These sections were made from greywacke blocks. After being cut and smoothed in the University of Liverpool and choosing the surfaces to observe, the rock surfaces were sent to an external private specialized company with the aim to get the requested thin sections. The surfaces were selected in a way to study the fractures, natural and induced (Fig. 2.6a). For conventional SEM images, the samples must be electrically conductive, at least on the surface, and connected to ground to prevent electrostatic charge build up on the surface. For this reason a very thin layer of conductive material (graphite) has been applied on the thin section utilized for the SEM, commonly deposited with the sputtering technique. The same operation has been done in the case of the two polished blocks containing the samples with the single fracture (Fig. A24). The polished blocks were produced by immersion of the fractured samples inside a cylindrical container, which then has been filled with epoxy resin mixed with a hardener liquid (Fig. 2.7). After the two blocks were obtained, the rock surfaces were polished by hand with progressively smaller grit sizes (where the smallest grit size was 0.3 μm).

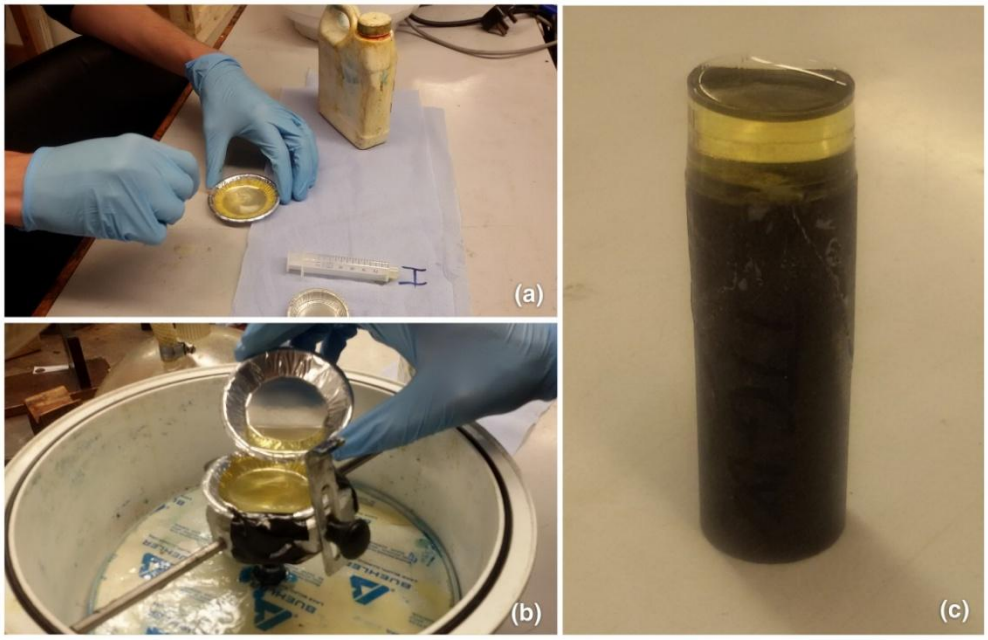

Figure 2.7: a) Epoxy resin preparation; b) Lately the resin is inserted in the vacuum chamber and the air is removed before to pour the resin on the core; c) Finally the core is stuck inside the resin, which also blocks its internal cracks avoiding their movements.

2.2. DESCRIPTION OF THE APPARATUS USED

This chapter will introduce the apparatuses and their components, explaining how they work and how the data are obtained. Schemes, diagrams and photos will be displayed to give a better idea of the descriptions: the technical scheme of the jig for the Brazilian test particularly. More attention will be given to the machines that were made in the University of Liverpool in comparison to the other standard commercial equipment used.

2.2.1. UNIAXIAL APPARATUS

The uniaxial deformation apparatus utilized for the uniaxial tests is designed by ELE International, with modifications made by Prof. Daniel Faulkner in order to allow P and S wave velocity measurements and logging of the mechanical data. This machine

(Fig. 2.9) is able to apply on the core a force of 294.3 kN in a vertical direction. During the deformation process it is possible to measure the velocity of P and S waves, their attenuation and the elastic properties (from strain data).

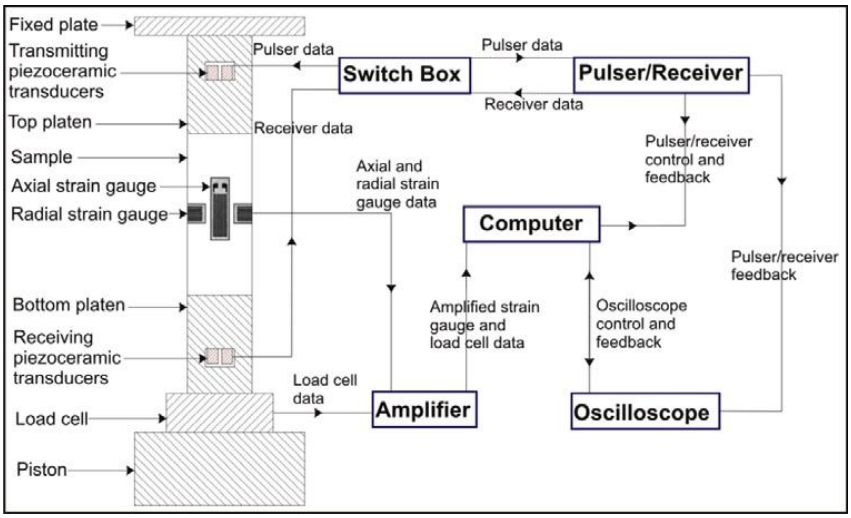

Figure 2.8: Schematic diagram of uniaxial apparatus (after Blake, 2011).

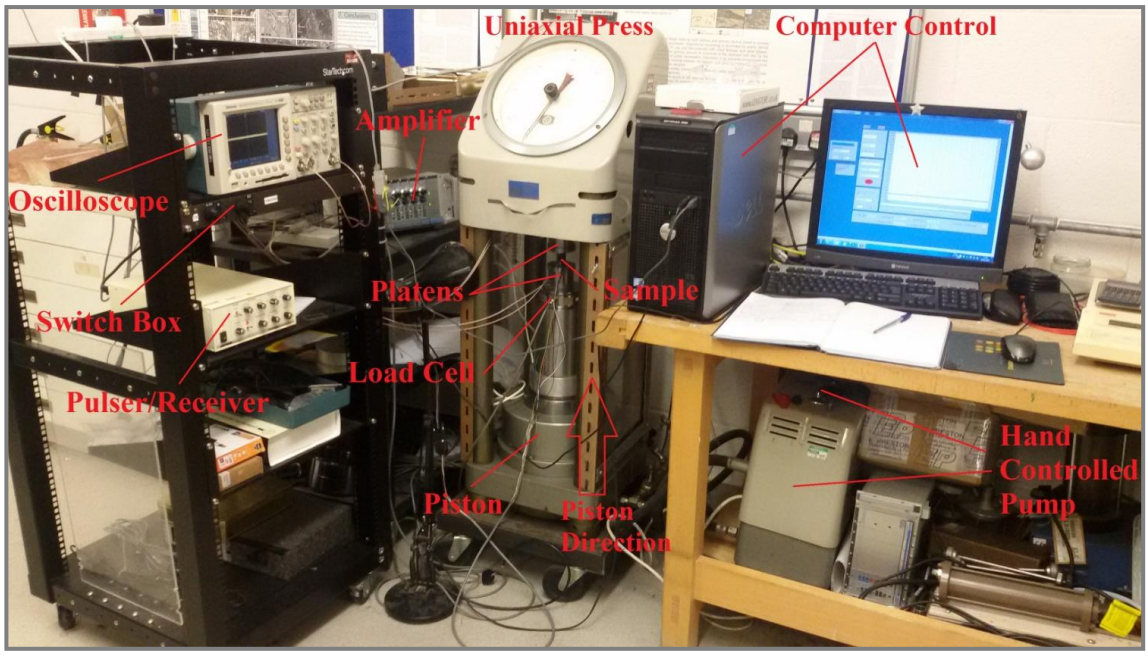

Figure 2.9: Uniaxial and seismic apparatus utilized for the tests which are described in this work. On the left side is the seismic equipment, which is linked to the core. In the middle is the uniaxial equipment, which hosts the core. On the right side there is the operator position, who controls the tests using the computer control and the pump.

The uniaxial sample assembly is composed of two main parts: the top platen and the bottom platen. There are two different kinds of top platen. The top platen (I) has a P wave piezoelectric ceramic and only one S wave piezoelectric ceramic. The top platen (II) has a P wave piezoelectric ceramic and two S wave piezoelectric ceramics (Fig. 2.10). The bottom platen is similar to the top platen (I), so it presents one P wave piezoelectric ceramic and one S wave piezoelectric ceramic only. In the top platen (II), the direction of polarization of the two S wave piezoelectric ceramics (called S1 and S11) is perpendicular (Fig. 2.10c). When the top platen (II) is at 0° position in comparison with the bottom platen, the polarization direction of the S1 wave piezoelectric ceramic lays on the same plane of the polarization direction of the S wave piezoelectric ceramic. The polarization direction of the S11 piezoelectric ceramic is at 90° to S1. All the piezoelectric ceramics are glued to the platens using a silver-loaded epoxy adhesive, which has a high mechanical bonding, an optimal electrical conductivity and a quick room-temperature curing.

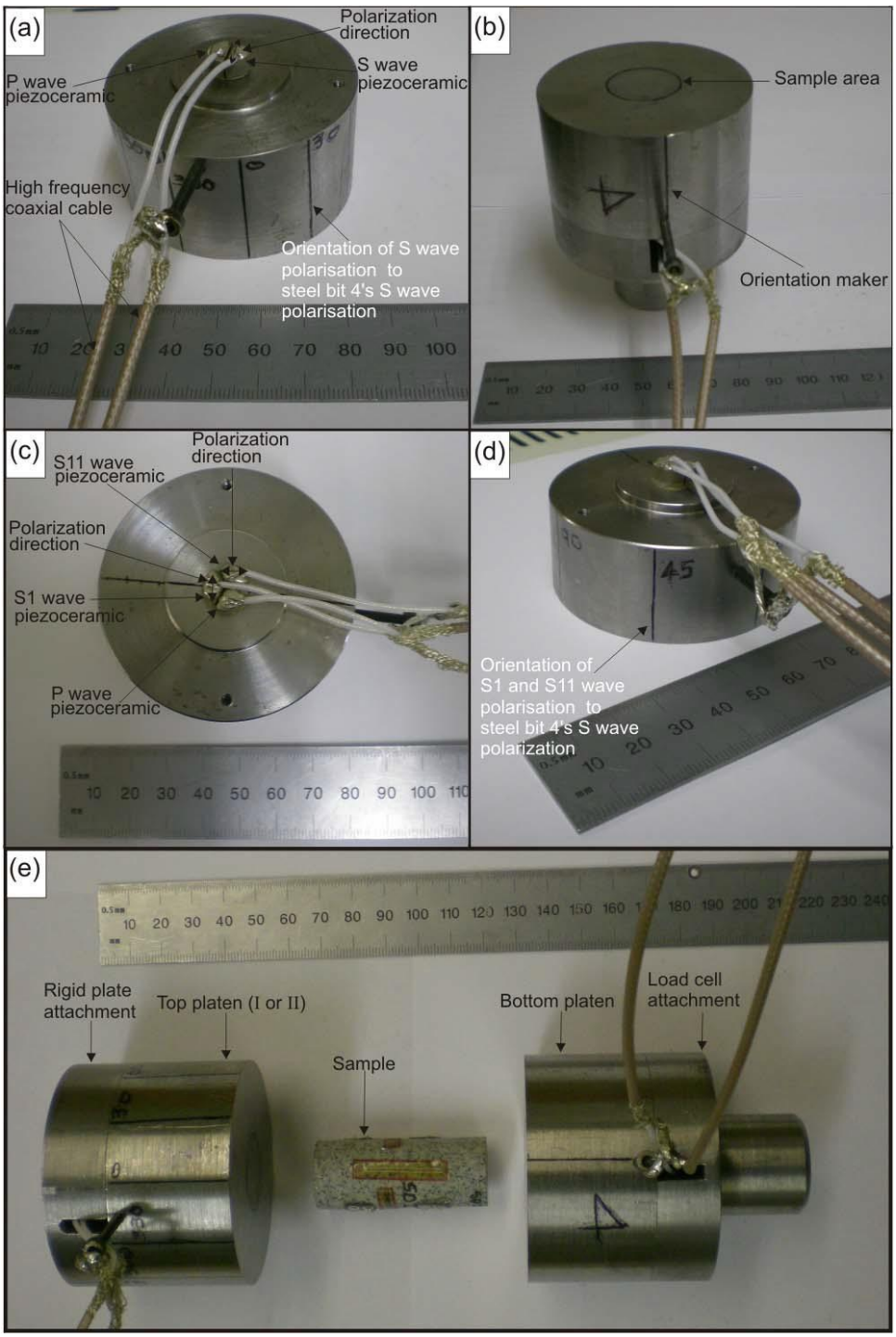

Figure 2.10: Uniaxial sample assembly. a) Top platen (I). b) Bottom platen. c-d) Top platen (II). e) Complete uniaxial sample assembly (from Blake, 2011).

The uniaxial sample assembly is located in a standard uniaxial press where the sample is compressed in unconfined way ($\sigma_2 = \sigma_3 = 0$) between a moving hydraulic piston (hand controlled) and a fixed rigid plate. The hydraulic piston is managed by the operator who controls the valve pump. To monitor and obtain data on the elastic properties of the rock sample, an axial and radial strain gauges are utilized (in this work two axial and two radial strain gauges have been used (Section 2.1). Each strain gauge is wired in a 1/4 Wheatstone bridge configuration. The resolution of the strain gauges is ±0.000005. A load cell (Tedea-Huntleigh compression load cell, model 220, grade C4) with high accuracy is used to estimate the force applied. In particular, the load cell has a maximum capacity of 294.3 kN and a resolution of ±0.0075 kN. The signals of strain gauges are amplified using strain gauge transducer amplifiers (model RDP 628), with a 600 multi-channel signal conditioning system. The amplified signals are finally recorded by the computer. This apparatus performs experiments at room temperature.

2.2.2. ULTRASONIC MEASUREMENT SYSTEM

For the generation, propagation and reception of seismic waves an ultrasonic measurement system is used. This arrangement is composed of five main components: piezoelectric ceramics, a pulser/receiver, a switch box, an oscilloscope and high frequency coaxial cables. Usually this equipment is used in conjunction with the uniaxial apparatus, as in this project, but it can be engaged also with the triaxial rig (Fig. 2.9).

2.2.2.1. Piezoelectric ceramics

The role of the piezoelectric ceramics is to generate and receive P and S waves. They are capable of converting the electrical energy to mechanical energy and, in the opposite way, mechanical energy to electrical energy. When an electrical potential is applied across the ceramics and they change their shape. The kind of ceramic used in this work is made from PZT-5H, or rather lead zirconate titanate ($Pb(Zr,Ti)O_3$). The

most important feature of it is that it has a peak frequency of 1.5 MHz, which is due to dimension of the crystals. When the piezoelectric ceramic is polarized in the direction of the wave propagation and the electrodes are set on the two sides of the ceramic, orthogonal to the polarization direction, P waves are produced. Furthermore, when the piezoelectric ceramic is polarized perpendicular to the direction of the wave propagation and the electrodes are set on the two sides of the ceramic, S waves are produced (Fig. 2.11) (Blake, 2011).

The backing material is typically a highly attenuative, high density material that is used to control the vibration of the piezoelectric ceramic by absorbing the energy spread out from the back part of the piezoelectric ceramic. However, overdamping of the crystal will reduce the signal amplitude, so a compromise is sought. When the elastic wave impedance of the backing material matches the elastic wave impedance of the piezoelectric ceramic, the result will be a heavily damped piezoelectric ceramic with wider bandwidth that shows good range resolution (an excellent characteristic for attenuation measurement), but may be lower in signal amplitude (Blake, 2011). The elastic wave impedance (Z) of a material is defined as the product of its density (ρ) and elastic wave velocity (V):

(Equation 2.3) $$Z = \rho V$$

As the elastic wave impedance of the piezoelectric ceramic exceeds the elastic wave impedance of the backing material, the amplitude of the signal increases but the piezoelectric ceramic resolution is reduced. In this work sintered stainless steel backing material was used, 0.125"+/-0.005" thick with 0.5 μm nominal pore size (from Mott Corporation, USA) as backing material on the piezoelectric ceramics (Van Valkenburg, 1983). The elastic wave impedance of both backing material and PZT-5H is ~29.7 MRayls. It is hard to soft solder a material to stainless steel because of its thin and strong oxide films. Hence, a thin sheet of copper, ~0.25mm thick (which is much easier to soft solder on it) is glued to the stainless steel using silver-loaded epoxy adhesive.

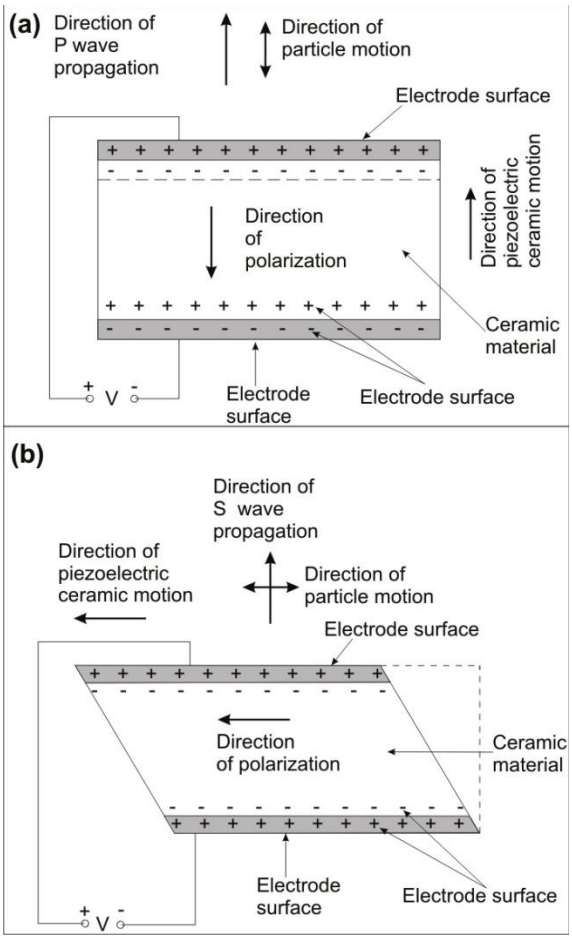

Figure 2.11: a) Schematic of piezoelectric ceramics for compression waves. Based on the polarization, piezoelectric ceramics can generate or receive P or S waves. P waves are generated when the piezoelectric ceramic is polarized in the direction of wave propagation and electrodes are applied on the two faces of the ceramic normal to the polarization direction; b) Shear waves. For the generation of S waves, the piezoelectric ceramics are polarized normal to the direction of wave propagation and electrodes are applied to the two faces that are parallel to the polarization direction (after Strassburger, 1982).

2.2.2.2. Pulser/Receiver

The pulser/receiver is used to produce the excitation voltage for the transmitting piezoelectric ceramic in the ultrasonic measurement system and amplifies the electrical response coming from the receiving transmitting piezoelectric ceramic.

Two piezoelectric ceramics are needed to operate the pulse/receiver in through-transmission mode: one to produce the elastic wave and the other one to receive the wave propagated through the rock sample. The pulse/receiver can be used in pulse-echo mode as well. In this case, it will need only one piezoelectric ceramic that will generate

the elastic waves and detect the reflected ones from the "sample / loading platen" interface.

The pulser part of this system (Fig. 2.12) controls three main things: energy, repetition rate, and damping. Energy control has pulse energy and pulser impedance that sets the energy of the excitation pulse generated by the pulser, as long as pulse amplitude control to set the amplitude of the excitation pulse. This energy is stored in the capacitor and is from time to time discharged into the sending piezoelectric ceramic by closing the repetition switch. The repetition rate controls the frequency and the damping control regulates the damping that is applied to the piezoelectric ceramic.

The receiver part of the pulser/receiver has a low-noise amplifier which amplifies the received electrical signal. These signals then go through modifiable high and low pass filters.

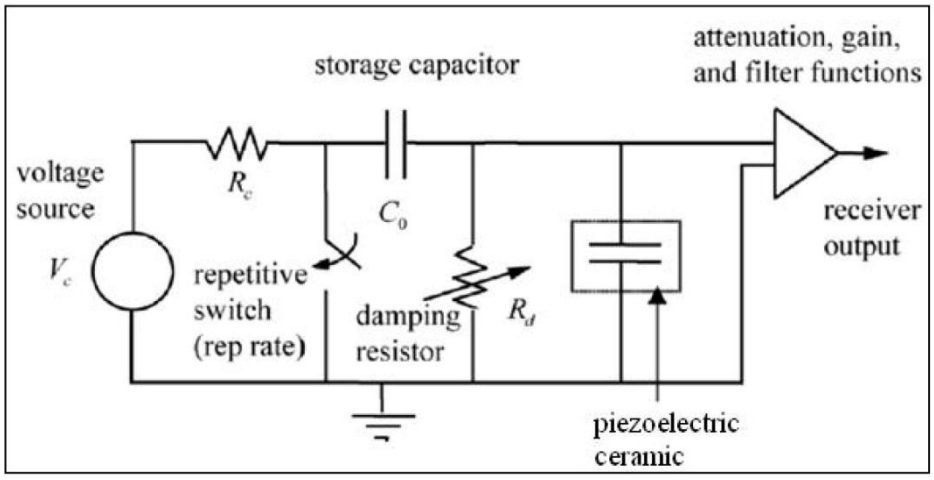

Figure 2.12: A highly simplified circuit representation of a “spike” pulser/receiver (after Schmerr Jr and Song, 2007).

2.2.2.3. Switchbox

The switchbox allows the possibility to choose which piezoelectric ceramic have to be excited or from which one receives the signal. Every switch presents the option to select the P wave piezoelectric ceramics, the S or S1 wave piezoelectric ceramics, either S11 wave piezoelectric ceramics.

2.2.2.4. Cabling

The transference of the electrical pulses between pulser, receiver and piezoelectrical ceramics occurs through electrical cables. Given the high MHz frequencies involved in the experiments, it is possible that the signals are subject to minor modification. To reduce any potential effect, high frequency coaxial cables are used. The resistance of this kind of cable has to be the same of pulser/receiver output with the purpose to decrease as much possible the internal reflections during the connections between the components. Ultimately, to have optimal performance the resistance of the high frequency coaxial cable is fixed to 50 Ohm.

2.2.2.5. Oscilloscope

The oscilloscope is an electronic measuring instrument that displays, on a two-dimensional graph, the trend in the time domain of the electrical signals and measures the voltage in an easy way. Usually the oscilloscope is used to analyze periodic signals. The horizontal axis of the graph represents the time, while the vertical axis represents the voltage and it is expressed in volts. If the signal is periodic, it is possible to get a stable track by adjusting the time base so that it coincides with the frequency of the signal or a sub multiple. For example, if there is in input a sinusoidal signal at 50 Hz, you can adjust the time base so that a horizontal scanning occurs in 20 milliseconds. This system is called “the sweep continuously”. The oscillator of the time base, not being synchronized with the signal analysis, prevents a stable signal trace being obtained, so it will be seen floating on the screen more or less quickly from right to left or vice versa. To obtain a stable trace, contemporary oscilloscopes have a function called “trigger”: This circuit starts scanning only when a voltage limit is exceeded. After completing the scan the oscilloscope waits for a new event. After that, the display remains synchronized to the signal and the track is stable. The limits of sensitivity of the trigger and of the other parameters are modifiable by the operator. This can be done by introducing a delay between the event and the start of the display, so as to analyze parts of the signal that would be out of the display field otherwise. In particular, in this work a Tektronix TDS 3032B Oscilloscope has been utilized.

2.2.3. PYCNOMETER APPARATUS

The type of pycnometer utilized in this work is a "multipycnometer" model: MVP-D160-E from Quantachrome Instruments. The multipycnometer is a versatile manual pycnometer. It earns this name from its multiple volume feature that offers three sizes of interchangeable samples cells: 135 cc, 20 cc, and 4.5 cc. In addition, there are three different calibrated reference volumes which provide peak performance for every cell size (www.quantachrome.com).

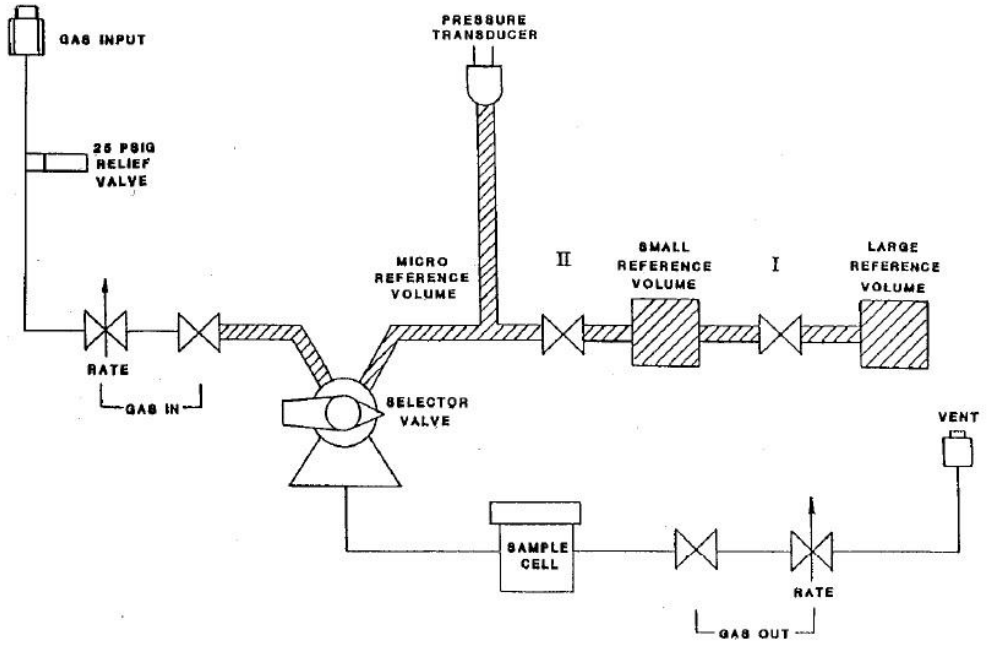

Figure 2.13: Schematic diagram of the helium multipycnometer (from "operating manual MVP-D160-E" - Quantachrome Instruments).

As shown in Fig. 2.13, the multipycnometer is composed mainly of the following pieces:

1) Gas tank connections.
2) Sample cells.
3) Toggle valves.
4) Needle Valves.

5) Pressure relief valve.

6) Selector valve.

7) Pressure Transducer.

The gas is introduced inside the pycnometer by the "gas input" implant. Gas tank connections have the function to connect helium (or nitrogen) gas tanks to the rest of the system. Three sample cells and two adapter sleeves are supplied with the multipycnometer. The cylinder located in the lower front panel is the sample cell holder. The sample cell is a stainless steel cup which slides into the sample cell holder or adapter sleeve. To remove the sample cell there is a black plastic cover on top of the sample cell holder that has to be rotated. The toggle valves need to control the gas movement, to pressurize the cell and to stop the gas flow. The "gas out" needle valve is used to control the rate at which the pressure is released when venting the sample cell or when vacuum is required to decontaminate the sample. The "gas in rate" needle valve is utilized to control the flow rate into the multipycnometer. It defines the rate at which the pressure is developed and also controls the rate at which pressure is released when venting the sample cell or when vacuum is required to decontaminate the sample. A pressure relief valve is located immediately after the input fitting (Fig. 2.13). This valve prevents damages to the pressure transducer due to the over-pressurization. The selector valve has the function to regulate the flow in the chambers. Actually when the selector valve is pointing to the left the sample cell is included in the flow path, instead when it points on the right side only the reference volume is included. The pressure transducer converts the pressure into an analog electrical signal. In the end, the gas is released through the vent.

2.2.4. TRIAXIAL AND PERMEABILITY APPARATUS

The triaxial deformation apparatus used in this project to conduct triaxial tests, permeability and seismic wave velocity measurements, is designed and built by Prof.

Daniel Faulkner. This machine is a high pressure and high temperature triaxial deformation apparatus with a servo - controlled fluid flow system.

This rig is able to perform triaxial experiments in 20 mm diameter standard sample size at 250 MPa confining pressure (servo controlled), 250 MPa pore pressure (servo controlled) and ~1000 MPa differential stress with a load capacity of 300 kN. The servo controlled pore fluid system consists of a pore fluid pressure connection at the upstream end of the leading to a high precision volumometer. The downstream end of the core is linked to a low volume reservoir. This arrangement can be utilized to run permeability measurements using the pore pressure oscillation technique (Fisher 1992), or the pulse transient method (Brace et al., 1968). Moreover, a servo controlled constant displacement rate or constant force (creep) with a displacement rate between 20 μm/s and 30 mm/year can be achieved in the apparatus. The pore fluids usually used are water, argon, CO_2 or reactive fluids.

The temperatures for triaxial tests can be run up to 200°C using a furnace. There is also an internal furnace capable to reach 750°C using argon confining fluid. This apparatus has an acoustic wave velocity/AE system which utilizes an acoustic sample assembly with P and S wave transducers and it is contained within the loading platens. Data are recorded using 16-bit NI DAQ (Data AcQuisition) card and software. The servo control systems are also driven by LabVIEW software.

In this rig the axial load is applied from the bottom of the axial column. The internal force gauge has been manufactured from M300 maraging steel. It has a yield strength of around 2GPa but still conserves malleability. These properties allow to a small cross sectional area to be machined in order to maximize the elastic distortion of the active force gauge element without permanent deformation. The force gauge is designed so that the elastic distortion is localized to the high pressure side of the seal this ensure the force gauge is measuring the force internally. The purpose of the seal is to prevent oil from leaking at the bottom of the pressure vessel.

The rig (Fig. 2.14) can be schematically divided in some main parts: pressure vessel, sample assembly, force gauge, axial loading system, pore fluid controller system, confining pressure system and finally, transducers, data logging system and computer control.

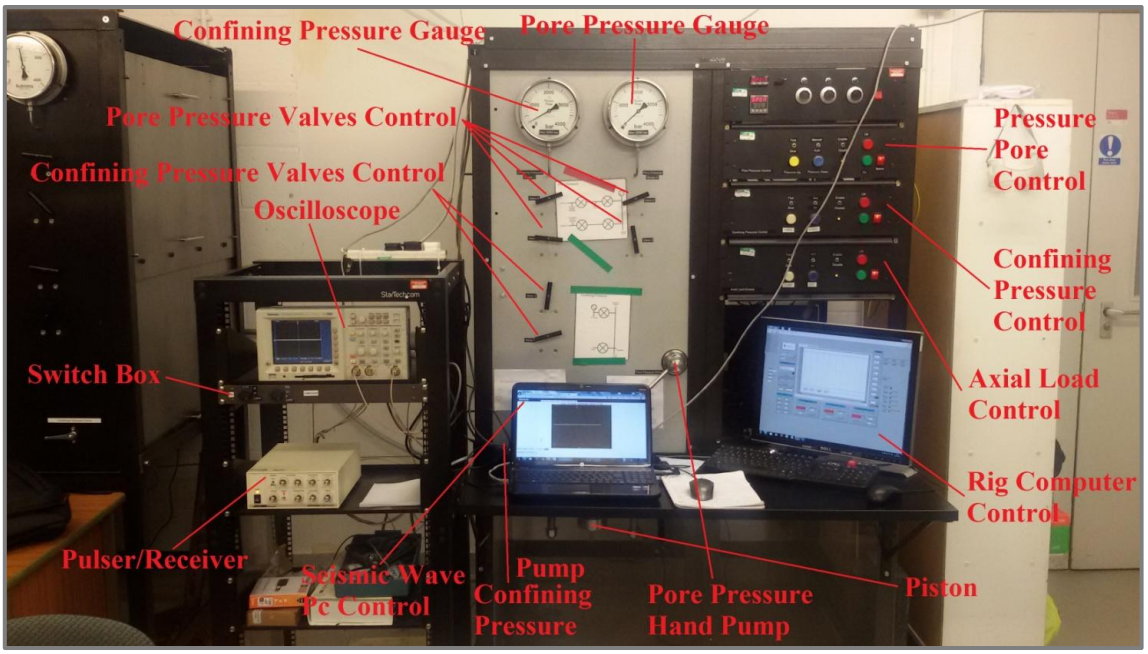

Figure 2.14: Triaxial rig, seismic equipment and computer controls.

2.2.4.1. Pressure vessel and sample assembly

The apparatus has a pressure vessel made of AISI H13 hot-worked tool steel. It uses silicon oil as its confining medium. The silicon oil is chosen (instead of water) as a confining medium in order to prevent corrosion in specific elements of the system. The pressure vessel is situated on the upper part of the rig (Fig. 2.15b) and the sample assembly is inserted inside it through the hole on the top (Fig. 2.15b). The sample assembly secured inside the vessel by a nut on the top, an o-ring and a brass ring to avoid gaps in the inner vessel and the sample assembly.

The pressure vessel is designed to maintain confining pressures up to 250 MPa. It is possible to take measurements of the confining pressure with an analogue gauge and a pressure transducer. The sample assembly is composed by three principal parts: the upper part, the lower part, and the third part which is the sample located between them (Fig. 2.15c). In triaxial tests the impervious jacket preserves the pressured fluid from the sample.

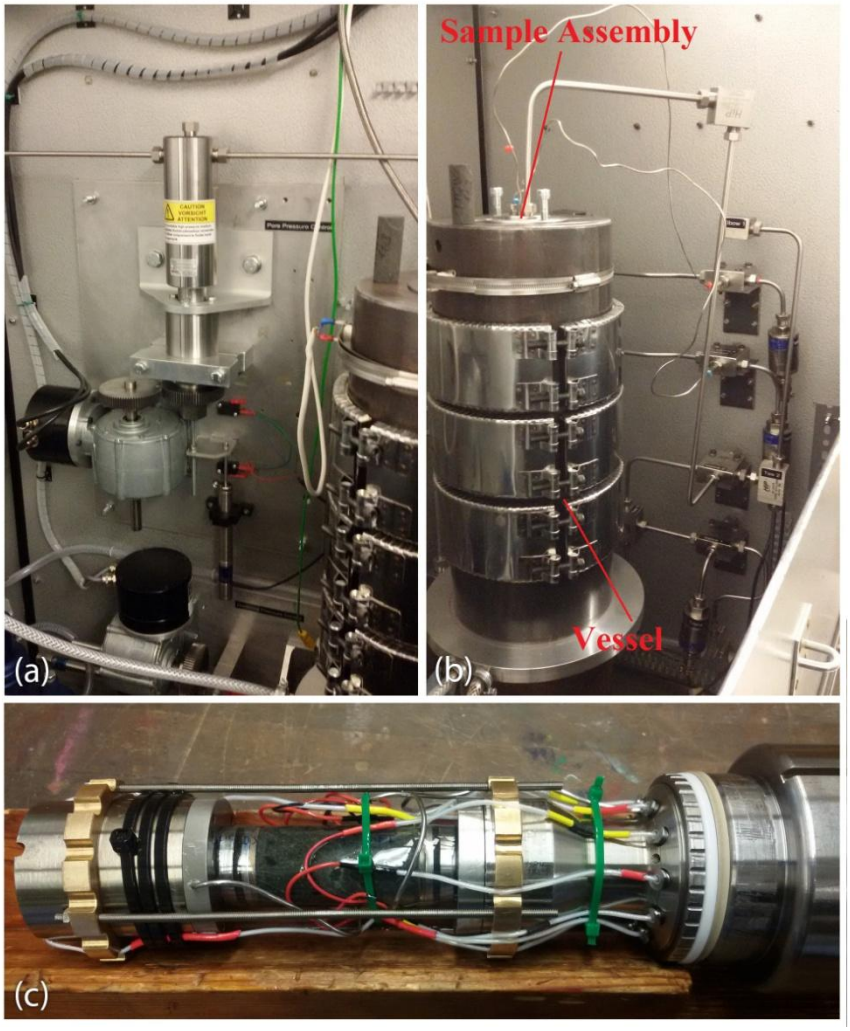

Figure 2.15: a) Internal view of the rig: Nova Swiss hand pump modified to act as a servo-controlled pump; b) Internal view of the rig: the vessel hosting the sample assembly and valve connections on the right side; c) Sample assembly hosting the jacketed greywacke core.

2.2.4.2. The force gauge

The force gauge column is accommodated inside the force gauge block and sealed into the pressure vessel and the force is applied axially from below. The force gauge relies on the elastic distortion of an elastic element in the loading column. It is made from maraging steel C300 (an iron-nickel alloy), which has a very high yield strength (~2 GPa), but similar elastic properties to most steel. This means that the crossectional area can be made quite small, giving a relatively high strain, without approaching the yield strength of the material. This gives a very sensitive force

measurement. The elastic distortion is measured using a sensitive LVDT (Linear Variable Differential Transformer), placed in a blind hole drilled into the force gauge (Fig. 2.16). The output voltage of the force gauge LVDT is calibrated against the output voltage of a commercial load cell which is converted into a force using a calibration provided by the load cell manufacturer. The calibration for the load cell is 2mV/V full scale (30,000 kg or 293 kN) and the excitation voltage supplied is 10 V. By loading from 0 to 30 tons and back down while continuously logging both outputs in the triaxial logging program on the computer. It must be noted that this calibration occurs without confining pressure, as there is no sealing arrangement built into the calibration headstock.

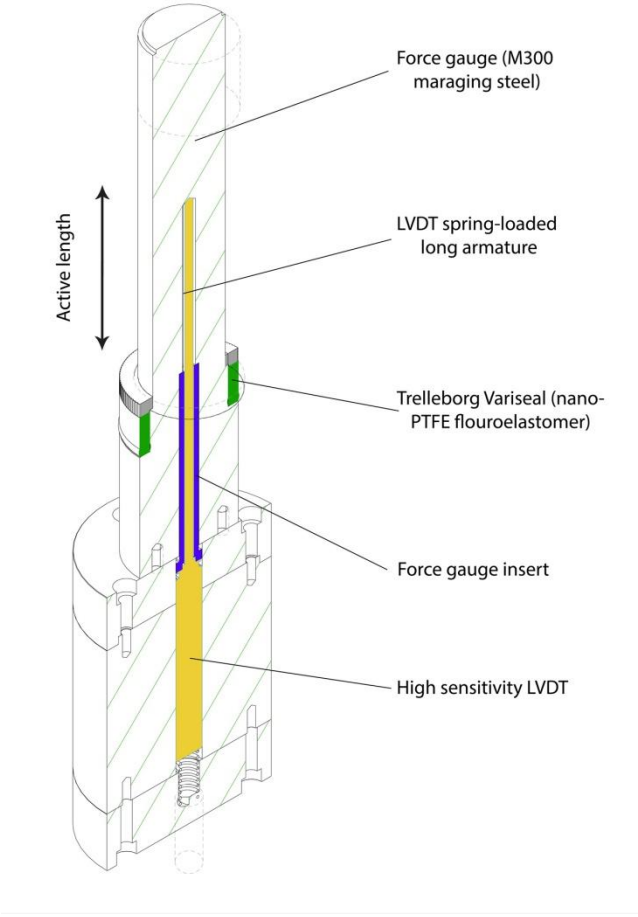

Figure 2.16: Force gauge diagram. The area highlighted in yellow is the part related to the LVDT.

2.2.4.3. Axial load, pore fluid controller, confining pressure and data logging systems

The triaxial machine is composed by a series of servo-systems, which can operate together during the tests. The "axial load system", or servo controlled axial displacement system, controls the force or displacement. The mechanical setup is composed of a ball screw, some gears and a drive motor (Fig. 2.17). The piston displacement is detected by an LVDT. The "pore fluid controller system" is made up of a servo controlled Nova Swiss 5 cm^3 pump which is linked to the upstream reservoir. Through a series of valves and pipes, this system is able to control and modify the pressure of fluid in the sample. In order to generate confining pressure a "confining pressure system" has been installed, which consists in an air driven pump using low viscosity silicon oil. This system is capable to create a confining pressure around the jacket. The confining pressure that can be achieved is 250 MPa.

All data received from the displacement and pressure transducers is registered by the computer. The transducer resolution and the accuracy of the transducers are very important because they affect directly the results obtained from the experiments. Typically, the pressure transducers have a resolution of ±0.02 MPa and the displacement transducers of ±0.25 microns. The accuracy is determined by calibration against a standard pressure gauge or dial gauge. The data is logged using a 16-bit NI - DAQ PCI card in the PC (National Instruments Data Acquisition device). This card is linked to a data logging board via connectors. LabVIEW (2014) is the platform where the software works and it is used to communicate with this device in order to register the pressure and the displacement data. This software was written and developed by Prof. Daniel Faulkner.

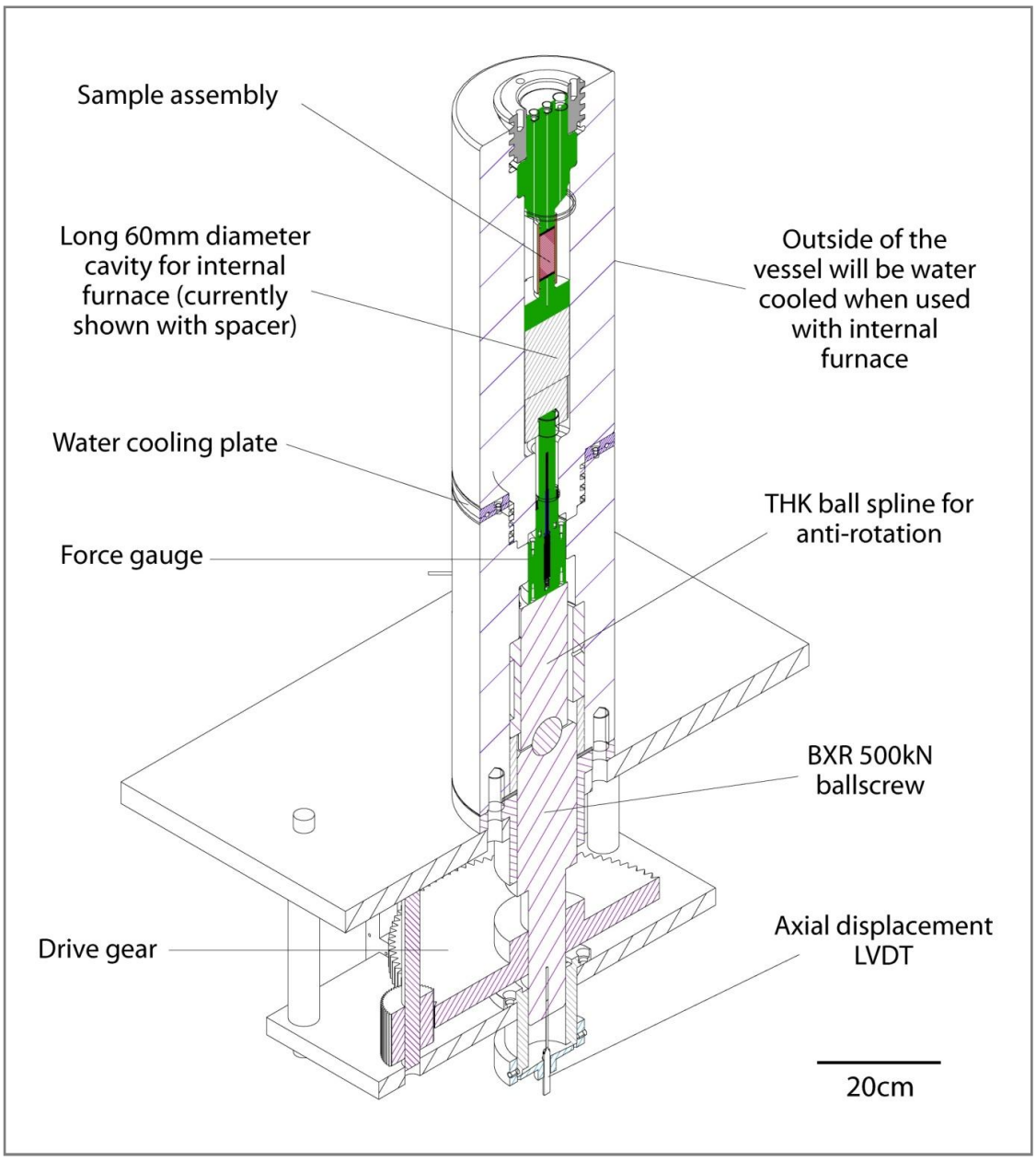

Figure 2.17: Schematic diagram showing the principal elements of the complete rig assembly.

2.2.5. BRAZILIAN TEST APPARATUS (TENSILE STRENGTH)

In order to perform the Brazilian test on the samples to ATSM standards, it was necessary to design a load jig to achieve this purpose. The Brazilian jig was designed specifically for this project following the guidelines given in ATSM D3967-08. Fig.

2.18 shows the design used. The diameter of the cores used in this experiment is 20 mm and in order to have an accurate measurement there are few parameters to respect. These are to cut the ends of the specimen parallel to each other and at right angles to the longitudinal axis, so that the ends of the specimen will not deviate from perpendicular to the core axis by more than 0.5°, and the circumferential surface of the specimen will be smooth and straight to 0.50 mm (ASTM, D3967 - 08).

The jig is made of two housing pieces in mild steel. The top piece has on its center a hemispherical seat, which is a location for a chrome ball, which is very important in case of asymmetric loading. The center of the sphere in the hemispherical seat coincides with the center of the loaded side of the specimen (ASTM, D3967 - 08).

On top of the chrome ball is positioned a loading plate with another hemispherical seat above which the force is applied. The housing (Fig. 2.18) pieces host inside them two bearing blocks (made of D2 Steel, Hardened to HRC 60), which are curved in order to reduce the contact stresses. A geometrical condition is applied here: "the radius of curvature of the supplementary bearing plates shall be so designed such that their arc of contact with the specimen will in no case exceed 15° or that the width of contact is less than D/6, where D is the diameter of the specimen" (ASTM, D3967 - 08).

This curved surface is an arc of circumference and in respect to the previous condition, to achieve the right curvature of this arc I calculated the hypothetical diameter of this circumference in relation to the core circumference.

Finally, the upper part of the jig moves vertically along two guide-roads set on the bottom housing tolerance holes and crossing the top housing in the clearance holes (Fig. 2.18). In order to run the test the jig is positioned inside the press of the uniaxial apparatus as described previously (Section 2.2).

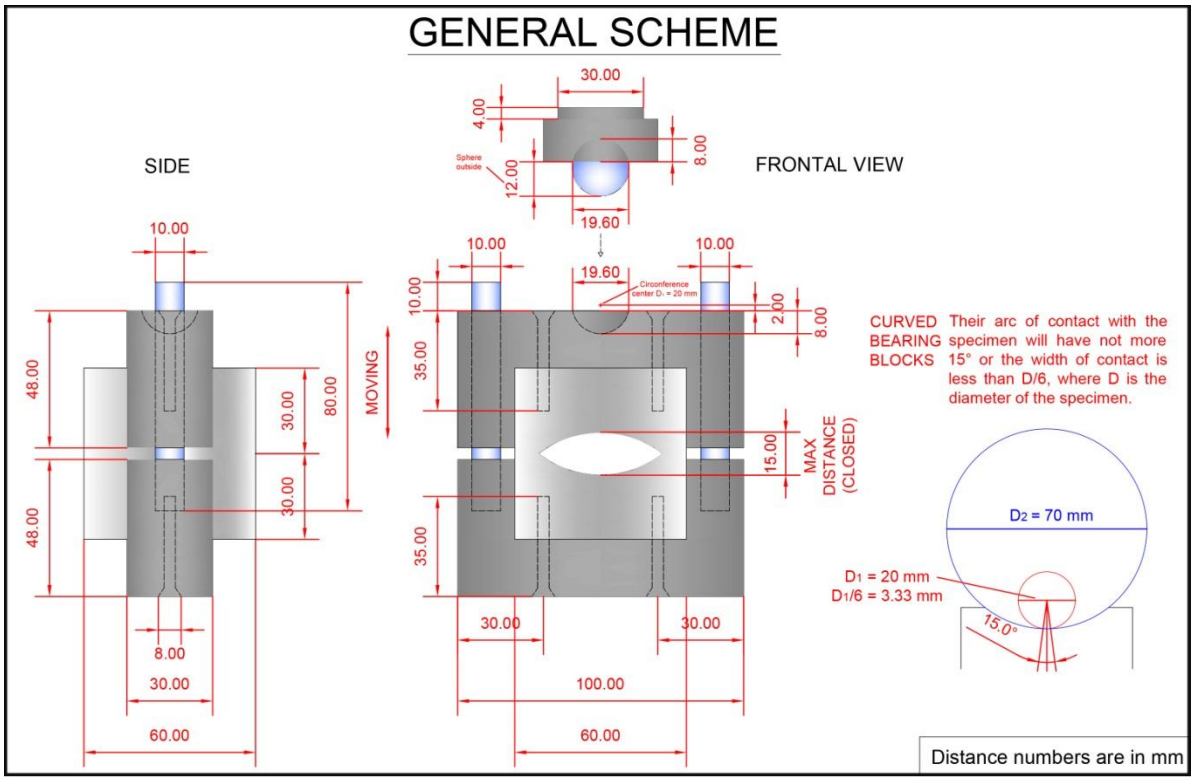

Figure 2.18: Scheme of the jig for Brazilian test from AutoCAD 2014.

2.2.6. SEM

The conventional scanning electron microscope (SEM) utilized in this work is the XL30 of the XL Series from Philips. The electron optical column is optimized for both high resolution imaging: X-ray microanalysis and low magnification performance. Moreover, an embedded EDX system can provide to the user a complete analytical capacity all included in one instrument (See Section 2.1 for SEM samples preparation; Fig. 2.6a shows a greywacke this section; Fig. A24).

2.2.7. NETZSCH TMA 402 F1 HYPERION

Netzsch TMA 402 F1 "Hyperion" is used for multiple heating, cooling and axial load and is suitable with a system of up to 1200°C and a range from 3mN to 3N for the

sample loads. Hyperion measures the thermal expansion coefficient. This machine is composed mainly by a furnace, where the sample zone is located. Around the sample zone there is the heating/cooling system. The sample is placed on a platform, which is the top of a pushrod made of alumina (Al_2O_3). This pushrod is linked to a force gauge, part of the high precision inductive linear variable displacement transducer (LVDT). The LVDT measures the variation of the length of the sample with a resolution of 0.125 nm. The sample chamber is evacuated and purged with argon (zero grades) three times before each experiment to flush out any remaining oxygen. During the experiments, the sample chamber is flushed with 20ml/min of argon. S-type thermocouples monitor both the sample temperature and furnace temperature (Fig. 2.19).

2.2.8. NETZSCH STA 449 F1 JUPITER

Netzsch STA 449 F1 "Jupiter" is used for differential scanning calorimetric analysis (DSC) and measuring specific heat capacity (Cp). The sample is placed inside a platinum crucible, which is located on the top of a rod. The rod (made of Al_2O_3) is linked to the high precision balance (utilized also for thermo-gravimetric measurements). This device is located in the lower part of the apparatus, where also the gas inlet valve is found. The gas (argon) goes in the machine through this valve and is channeled in the sample's chamber. The argon is later evacuated from a gas outlet valve located on the top of the machine. A system of thermocouples measures the temperature of the sample, a reference temperature and the inner chamber of the furnace (Fig. 2.19).

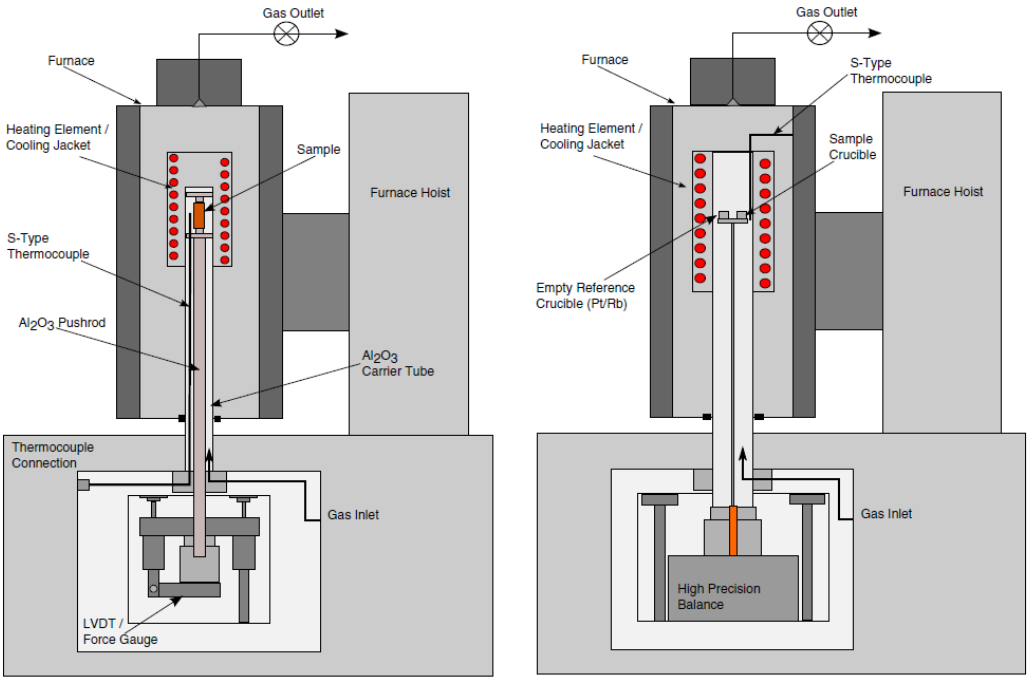

Figure 2.19: Diagrams of NETZSCH TMA 402 F1 Hyperion (left side) and NETZSCH STA 449 F1 Jupiter (right side) (from Siratovich et al., 2015).

2.3. EXPERIMENT METHODOLOGY

The third chapter will introduce the methodologies followed in the measurements. Since it is one of the most important factor in the geothermal fields, more attention will be given to the permeability. The methodology will be illustrated and reasons why these procedures have been chosen. It is important to say that before carrying out the experiments, the apparatus go through a calibration process in order to obtain the best data quality. All the experiments were performed at room temperature (around 20°C), except the thermo-analysis measurements, which are characterized by very high temperatures (till 1000°C).

2.3.1. UNIAXIAL TESTS AND SEISMIC WAVE VELOCITY MEASUREMENTS

The standard methodology for using ultrasonic testing to determine pulse velocities (ASTM, 1997a D2845-95) was adhered to for accurate and reliable measurements of P and S wave velocities. This experimental configuration and methodology lead to very clean elastic wave measurements from which the P and S wave arrivals could both easily be identified.

The cores tested were 20 mm diameter and ~50 mm length greywacke cores (Section 2.1). The first measurement of the seismic wave occurred before applying significant force (sample between the platens and ~0 kN (Section 2.2). At every increase of ~7 MPa, the force was held constant for a period of ~1 minute to record the P and S wave data, while the static data were recorded continuously. The loading rate was kept at ~2 MPa/min. When the force reached a value close to the failure point, which is predicted on the basis of the Westerly granite properties (since it was supposed before the tests that Westerly granite and Waipapa greywacke could have similar properties, based on previous tests (Heap and Faulkner, 2008) for both rocks), the load interval was decreased to ~5 MPa, then ~3 and ~2 MPa as failure was approached in order to have the more velocity measurements in the proximity of failure. Every tested core was brought to failure. Time dependent effects are almost negligible on the evolution of the elastic properties of Westerly granite for a hold time up to 6 hours (Heap and Faulkner, 2008). Similar behaviour was assumed for greywacke.

The software (LabVIEW 2014) records the force (in kN), axial strain and radial strain. The force was transformed from kN to MPa, in relation to the dimensions of the core. The volumetric strain was calculated as the axial strain summed to two times the radial strain.

(Equation 2.4) $$\varepsilon_V = \varepsilon_a + 2\varepsilon_c$$

The elastic properties of the material are usually obtained from the "linear" region of the stress-strain curve. The relationship does not necessarily need to be linear

as long as there is a reproducible relationship between stress and strain, such as for a perfectly elastic material. However, for this work a quasi-linear region was chosen between 40 and 120 MPa, and a linear fit was made to the data in this region.

The static Young's modulus is calculated from the ratio between axial stress in MPa (σ) and strain (ε) from the same region mentioned above using the formula:

(Equation 2.5)

$$E = \frac{d\sigma}{d\varepsilon}$$

The static Poisson's ratio is calculated from the axial and radial strain gauge data from the same region mentioned above using the formula:

(Equation 2.6)

$$\nu = \left| \frac{\varepsilon_{radial}}{\varepsilon_{axial}} \right|$$

Compression and shear wave velocities are defined as the length of the sample (*L*) divided by the arrival time of the waves (*t*), corrected for travel time in the steel spacers:

(Equation 2.7)

$$V_p = \frac{L}{t} \quad ; \quad V_s = \frac{L}{t}$$

(Equation 2.8)

Where Vp is the P wave velocity and Vs is the S wave velocity.

From the P and S wave velocities, elastic constants such as dynamic Young's modulus, E_d, and dynamic Poisson's ratio (ν_d) are also been estimated from the recognized relationships of isotropic materials as follows (e.g. Kuttruff, 1991):

(Equation 2.9)

$$E_d = \frac{\rho V_s^2 (3V_p^2 - 4V_s^2)}{V_p^2 - V_s^2}$$

(Equation 2.10)

$$\nu_d = \frac{V_p^2 - 2V_s^2}{2(V_p^2 - V_s^2)}$$

where ρ is the density. The change in the sample's density, calculated from the variation in volumetric change which occurs during uniaxial compression was accounted for in the formula.

During the uniaxial strength and elastic property measurements the errors that could occur are related primarily to the resolution (±0.0075 kN) of the force measurements and the measurement of the core dimensions. For errors in measuring the dimensions it has been estimated that it is approximately equal to 1.44%, while the force measurement is also related to the sensitivity of both the machine and the software. Significant variability between samples for UCS has been estimated be no more than 31.1%; while it is 21.4% for Young's Modulus and 55.7% for Poisson's Ratio. Also in picking the first arrival of the seismic waves the error occurs, in fact it has been calculated to be 4.62% for the Vp and 1.84% for the Vs. In relation to the errors is important to consider the sample variability of uncertainty, which is typically greater than any measurement errors.

Another factor to consider is the comparison with *in situ* values. In fact, the laboratory tests do not give values that completely represent those *in situ*. For example the variability of a hypothetical reservoir would be very high: different stress fields, macrofractures or fracture networks on large scale would result in differences from the parameters obtained in laboratory. The same is true of the seismic wave velocity measurements: first of all there are limitations due to the variability and the difference between the laboratory and field (Budiansky & O'Connell 1976). However, the errors are after over-estimated. For instance, Blake (2011) demonstrates that usually the errors for the seismic wave velocities in the reality are smaller than the error statistically calculated.

2.3.2. BRAZILIAN TESTS (INDIRECT MEASUREMENT OF TENSILE STRENGTH)

This test method is aimed at determining the splitting tensile strength of a rock by the diametric line compression of a disk. Before running the experiment it is important to mark a diametric line on the top of the specimen. This line helps the operator to put the specimen correctly in the centre of the jig in order to get the right position for the test. In this way the vertical orientation of the disk will be indicated by the marked line. It can be also utilized as a reference line for measurements of the diameter and for the thickness.

The specimen has to be placed in the centre of the spherically seated bearing surfaces. This was done considering the diametric line. At this point the force can be applied and kept constant increasing the compressive force to generate a regular rate of loading so that the failure will be reached (usually between 1 to 10 minutes of loading, depending by the type of rock). In general, this rate should be kept between 0.05 and 0.35 MPa/s (ASTM, D3967 - 08). The splitting tensile strength of the specimen is calculated with the following equation:

(Equation 2.11)

$$\sigma_t = \frac{2P}{\pi LD}$$

where:

σ_t = splitting tensile strength (MPa)

P = maximum force applied indicated by the machine (N)

L = thickness of the specimen (mm)

D = diameter of the specimen (mm)

To achieve a well-represented tensile strength value the following method has been applied: ten greywacke disks (Section 2.2) were tested in the jig for Brazilian tests getting the tensile strength for each disk by applying the formula in Equation 2.9. The errors that occur for the measurement of the tensile strength are related to resolution of the force readings and measurements of the sample dimensions.

2.3.3. POROSITY MEASUREMENTS

For the porosity measurements a helium pycnometer is employed. The helium pycnometer is an instrument specifically designed to measure the true volume of a porous solid exploiting the technique of Archimedes' principle of fluid displacement to determine the solid volume. The porous solids in fact possess a solid volume which is very different from the total volume, since they contain porosity. This kind of pycnometer takes advantage of the ability of helium - which has a small atomic dimension approaching one Angstrom (10^{-10} m) that ensures penetration into crevices and pores - to spread within the empty space inside the core, thus permitting to measurement of the volume actually occupied by the solid material.

The equation employed in the multipycnometer is:

(Equation 2.12) $$V_P = V_C - V_R [(P_1 / P_2) - 1]$$

Where:

V_P = Volume of solid part of the sample (cm^3)

V_C = Volume of sample cell (cm^3)

V_R = Reference volume (cm^3)

P_1 = Pressure reading after pressurizing the reference volume.

P_2 = Pressure reading after including V_C.

When V_P is achieved it is possible to calculate the pore volume:

(Equation 2.13) $$P_V = V_{CYL} - V_P$$

Where:

P_V = Pore volume

V_P = Volume of powder (cm^3).

V_{CYL} = Volume of sample cylinder (cm^3)

Finally, knowing that the definition of porosity of a porous medium is the ratio between the volume of void space and the bulk material volume it is possible get the porosity which is expressed as a percentage:

(Equation 2.14) $$\Phi = P_V / V_{CYL} \ \%$$

However, before starting the measurement a few operations are required for the preparation of the system. The operations consist of purging contaminating gas or vapor from the system. After this step it is possible to start with the measurement. When everything is over, it is necessary to decontaminate the sample within a vacuum.

To achieve a representative porosity value, the following method has been applied: three porosity measurements were taken for each core by applying the Equation 2.12, for a total number of 17 cores.

The readings of pressure and measurement of the sample dimensions are the primary sources of error in the measurements. Other sources of error include the assumption of ideal gas behaviour for the pycnometer measurements. Many samples contain impurities (minerals, particles, water concretions, etc.) on their surface and within pores, the presence of these impurities can affect the results in several ways: the actual weight of the sample is less that the weight indicated when weighed; contaminants fill pores causing a large sample volume to be observed; volatile impurities will cause erroneous readings. Successive volume determinations yielding results trending in one direction are usually an indication that contaminants are being removed after each depressurization. The measurements should be continued until two or three successive determinations are obtained to within 0.2% (operating manual MVP-D160-E).

2.3.4. THERMAL ANALYSIS

The linear thermal expansion and the specific heat capacity of greywacke were measured. For the thermal expansion the thermo-mechanical analyzer Netzsch

TMA 402 F1 “Hyperion” has been used while the thermo-gravimetric and differential scanning calorimetric analyzer Netzsch STA 449 F1 “Jupiter” has been used for the specific heat capacity and the thermogravimetric analysis. The main causes of error are related to the determination of weight and temperature. The thermocouple sits at the base of the sample, and consequently can report a temperature T different from the average of the sample. For these reasons, frequent calibrations of the instrument are necessary.

2.3.4.1. Thermomechanical Analysis (TMA)

The thermo-mechanical analysis occurs in two main stages: calibration and measurements. The greywacke specimens are cylinders of 6 mm diameter and 5 mm length (Fig. 2.2b). In order to correct for the thermal properties of the sample holder assembly, an alumina standard is utilized with similar dimensions to the greywacke sample. The sample is positioned on the top of the pushrod. Two thin alumina disks with a diameter of ~ 8 mm are placed on the bottom and on the top of the greywacke core respectively. When the calibration is over, the experiment can be run inserting the rock sample in its space. As before, the standard alumina sample is placed between the two alumina disks, one on the top and one on the bottom, in order to protect the sample carrier. The evacuation and argon filling is repeated three times as in the calibration phase. A constant force of 0.1 N (equivalent to 3.54 kPa) was applied during the measurements and an LVDT was used to record the strain data. During the experiment a constant flow of argon (zero grade) equal to 20ml/min was made to flow through the chamber. The heat rate was set to 5°C/min with an initial temperature of 25.4°C and a final maximal temperature of 600°C marking the end of the experiment. During the experiment the thermocouple collects the temperature data and sends them to the computer.

The coefficient of thermal expansion is the degree of expansion divided by the variation in temperature. The formula employed to calculate the linear expansion coefficient is:

(Equation 2.15) $$\alpha_L = \frac{1}{L}\ \frac{dL}{dT}$$

where:

L = measured length

dL/dT = rate of the change of the measured linear dimension on the variation of the temperature.

The variation in the linear dimension can be represented like this:

(Equation 2.16) $$\frac{dL}{L} = \alpha_L\, dT$$

This equation works if the linear expansion coefficient does not change too much in relation to the change of temperature dT and if the variation in length is too small, with dL/L << 1. If one of these conditions is not satisfied the equation must be integrated.

2.3.4.2. Simultaneous Thermal Analysis (STA)

As for the thermo-mechanical analysis, the specific heat capacity (Cp) and thermo-gravimetric (TG) analysis occur in two main steps: calibration and measurements. The greywacke specimens in this case are small cylinders of 6 mm diameter and 1 mm length. In order to define these data a standard sapphire disk is utilized as a reference sample. It is used for the standardization of the results comparing the obtained data to that of the reference material, which displays repeatable calorimetric behavior and thermal stability. Thus, the core is located in the sample crucible. At this point, the machine is closed and the software is set. The air has to be evacuated from the furnace (and from the core). Later, the argon gas is released inside the chamber and then evacuated out from the machine. This operation is repeated three times. When the calibration is over the experiment can be run. The evacuation and argon

filling is repeated three times like in the calibration phase. The same procedure as in the TMA measurements is used here. During the experiment a constant flow of argon (zero grade) equal to 20 ml/min was made to flow into the chamber. The heat rate was set to 10°C/min with an initial temperature of 50°C and a final maximal temperature of 1000°C marking the end of the experiment.

The heat capacity of a material is the ratio of the heat exchanged between the material and the environment and the temperature variation that follows. The specific heat capacity is the heat capacity per unit of mass of a material. To get this specific capacity the differential scanning calorimetry (DSC) is used. DSC is a thermo-analytical technique based on the difference of the heat flow required to increase the temperature of the sample and reference. Therefore, the temperature is kept constant in both the sample and reference and the heat required is recorded.

Once the test has started, the furnace heats the sample and the reference sample in the same way. Any variation of heat input between the two is due to the material to be analyzed: an exothermic reaction will require lower heat input into the sample compared to the reference, whereas an endothermic will need greater heat input.

Regarding the TG, it measures the variation of the mass of a sample during the heating. Changes will result from reactions involving the release of volatiles. In this case DSC is utilized to track the necessary heating to increase the temperature of the sample and any deviation from linearity can show a physical reaction (such as phase transition or thermochemical reaction) (Siratovich et al., 2015). Also for TG, after the measurement, there is the standardization phase in which the data are compared with the reference material (Aluminium oxide).

2.3.5. TRIAXIAL TESTS

To run the triaxial test the rig described before (Section 2.2) was employed. The experiment was run with an increasing differential stress, keeping constant at 5 MPa the pore fluid pressure. In this test a typical triaxial experiment was performed, where the

confining pressure was fixed ($\sigma_2 = \sigma_3$ = constant) and servo-controlled at 20 MPa, and the axial stress was increased to the failure. The axial load was applied gradually, and for every step permeability measurements and seismic wave velocities V_p and V_s were taken.

The software (LabVIEW 2014) reads the force (in kN), the displacement, pore pressure and confining pressure (MPa), data from where it has been possible measure parameters as variations of volume, axial strain and differential stress. Also in this case the core tested was a 20 mm diameter and ~50 mm length greywacke core (Section 2.1).

From the triaxial test the change in pore volume during the test was measured (-8.5 mm^3). Stiffness corrections for the elastic column distortion of the rig have been made. The sample column is loaded with a blank of known elastic properties and the displacement recorded as a function of force. Hence the stiffness of the loading column as a function of force can be measured. Using this calibration, the true displacement of the sample can be determined.

The variation of the temperature inside the laboratory produces drift in the force gauge reading. This is relatively small, less than 2 kN overnight.

2.3.6. PERMEABILITY MEASUREMENTS

The permeability is often measured in units of the Darcy, which is defined as the permeability of a porous material through which the rate of flow of water of 1 centipoise viscosity through 1 cm^2 of section is maintained at 1 $cm^3 \cdot s^{-1}$ by a pressure gradient of 1 $atm \cdot cm^{-1}$ (Shmonov et al., 1944). Instead, in this work the m^2 units (S.I. units) will be used to express the measured permeability.

2.3.6.1. The diffusion equation for the flow of compressible fluids through porous media

Faulkner (1997) explained that Darcy's law is a useful description for the flow of fluids through porous media under constant flow conditions. A more general description about the fluids flowing through porous medium can be found in the diffusion equation (Carslaw & Jaeger, 1959), as summarized by Faulkner (1997).

A compressible fluid flowing through a porous medium with a small matrix compressibility is equivalent to the conduction of the heat flow through a solid body. Assuming this, the equations used to represent the heat flow can be used in the same way to describe the fluid flow. The diffusion equation for the fluid flow, obtained from the equation of the heat flow (see Carslaw & Jaeger, 1959), is a second order partial differential equation, and states that for all the values of x, and for t > 0,

(Equation 2.17)

$$\frac{\delta p}{\delta t} = \kappa \frac{\delta^2 p}{\delta x^2}$$

where:

κ = hydraulic diffusivity

The hydraulic diffusivity (κ) of the rock is equal to the ratio between the hydraulic conductivity (K) and the storage capacity (β_c):

(Equation 2.18)

$$\kappa = \frac{K}{\beta_c}$$

The storage capacity (β_c) of a rock is defined as the additional volume of fluid stored a unit volume of rock per unit rise in fluid pressure. The unit of storage capacity is Pa^{-1}. Without the effects of storage, which arise from the elastic compressibility of both, fluid and rock, any increases in fluid pressure would be transmitted with infinite velocity through the porous medium. Brace et al. (1968) portrayed the storage capacity of a rock as:

(Equation 2.19) $$\beta_c = \beta_b + \varphi\beta_f - (1+\varphi)\,\beta_m$$

where:

β_b = bulk compressibility of the porous medium, Pa^{-1}

β_f = fluid compressibility, Pa^{-1}

β_m = compressibility of the constituent minerals, Pa^{-1}

φ = porosity

Knowing that, from Darcy's equation and according to Nutting (1930), the hydraulic conductivity is $K = \frac{k}{\eta}$ (where k is the permeability in m^2 and η is the fluid viscosity in Pa·s), and from the Equation 2.18, it is possible to see that the hydraulic diffusivity is linked to the permeability (k), the storage capacity (β_c) and the fluid viscosity (η) by the following relationship:

(Equation 2.20) $$\kappa = \frac{k}{\beta_c \eta}$$

Since the permeability is measured in m^2, the storage capacity in Pa^{-1} and the fluid viscosity in Pa · s, then the hydraulic diffusivity will be expressed in m^2/s and having dimensions of L^2T^{-1}, which are the same dimensions of the analogous quantity for the thermal diffusivity (Carslaw & Jaeger, 1959).

2.3.6.2. Methods of measurement of permeability

In general, there are two categories of measurements of the permeability: measurement of high permeability associated with low pressure; and measurement of

low permeability associated with high pressure. In the last case the low permeability will be identified as less than 10^{-18} m^2.

In this work it was possible to understand from previous tests (as the porosity tests), observations and from the literature, that the studied rock (greywacke) was expected to be very low permeability. Therefore, a method for low permeability measurement was applied.

The method used in this work to obtain the permeability values is the pulse transient method. It will be summarized here and detailed in a later stage. The pulse transient method was introduced and developed firstly by Brace et al. (1968) on Westerly granite to determine its permeability.

When the experiment begins, the upstream and downstream reservoirs of the sample are in balance. An increase of the upstream reservoir pressure or a decrease of the downstream reservoir pressure is suddenly imposed in order to apply a pressure gradient across the sample. The decay characteristics of this pressure pulse, monitored in the upstream or downstream reservoir or both may then be used to obtain a value for permeability.

The development of the technique by Brace et al. (1968) includes assumptions concerning the storage capacity of the porous medium, and therefore the result acquired is an approximate solution to the diffusion equation (Eq. 2.17), providing only values for permeability and no information about the storage capacity. In the following text it is shown that when low porosity rocks are tested, the approximation of the value for permeability obtained is more accurate. However, complete solutions to the diffusion equation based on this technique have been developed (Hsieh et al., 1981; Trimmer, 1981; Lin, 1982) but there are difficulties associated with using these, and these will be reviewed below, after a description of the original method used by Brace et al. (1968).

The flow of compressible fluids through porous media is described by equation (Eq. 2.17). If we re-write this equation, expanding the term for the storage capacity, we obtain:

(Equation 2.21)

$$\frac{\partial^2 p}{\partial x^2} = \left(\frac{\eta \beta_f}{k}\right) \cdot \left(\frac{\beta_b - \beta_m}{\beta_f} + \Phi\left(\frac{1-\beta_m}{\beta_f}\right)\right) \cdot \left(\frac{\partial p}{\partial t}\right)$$

Brace et al. (1968) claimed that fluid compressibility, β_f, is always much greater than either the bulk compressibility of the rock, β_b, or the compressibility of the constituent minerals, β_m, (see Brace, 1965). Therefore, the term (β_f - β_m) / β_f will be small, and in this analysis will be considered as zero. In addition, if the rocks undergoing testing are of a low porosity, then equation (Eq. 2.21) could be further simplified by setting $\varphi = 0$. Hence equation (Eq. 2.21) becomes:

(Equation 2.22)

$$\frac{\partial^2 p}{\partial x^2} = 0$$

and

(Equation 2.23)

$$\frac{\partial p}{\partial x} = f(t) + C$$

As a result, the pressure gradient does not vary along the length of the sample, but it will vary with time (Fig. 2.22).

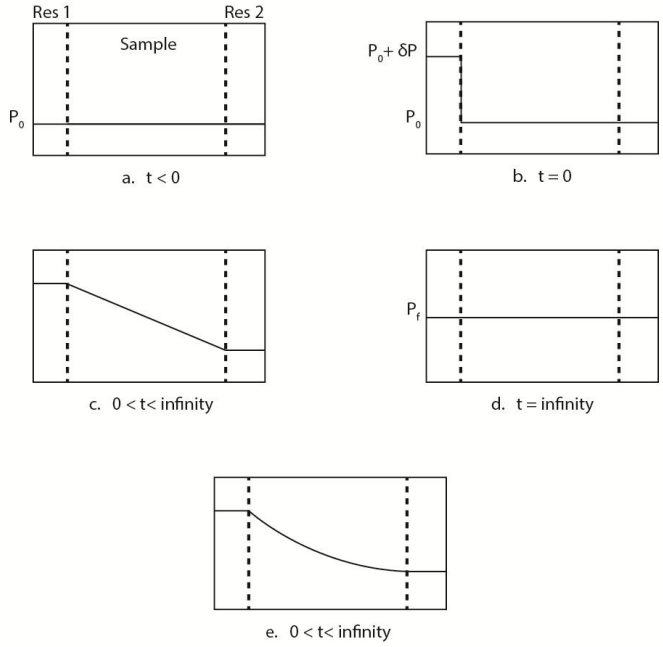

Figure 2.20: This illustration taken from Faulkner (1997) shows the assumed and real pressure variations along the sample during permeability testing using the pulse transient method (after Childs, 1986). Res1 = upstream reservoir; Res2 = downstream reservoir. a) initial condition where pressure is equal in both reservoirs and the sample; b) suddenly increase in pressure (δP) in upstream reservoir at time = 0; c) assumed variation of pressure along sample; d) final equilibration of pressure in upstream and downstream reservoirs and the sample; e) true pressure variation along the length of the sample.

The upstream and downstream reservoirs are equivalent to capacitors in an electrical circuit, and the rock sample may be associated to a resistor. So, the dissipation of the pressure transient in the upstream reservoir through the sample is analogous to the electrical discharge of a capacitor through a resistor. This follows an exponential path, and hence Brace et al. (1968) found that the pressure in the upstream reservoir, p_1 is related to time, t as follows:

(Equation 2.24)

$$P_1 - p_f = \Delta p \left[\left(\frac{V_2}{V_1}\right) + V_2\right] e^{-\lambda t}$$

where

(Equation 2.25)

$$\lambda = \left(\frac{kA}{\eta \beta L}\right)\left(\frac{1}{V_1} + \frac{1}{V_2}\right)$$

with:

p_f = equilibrium pressure (Pa)

Δp = step change in upstream reservoir (Pa)

A = cross-sectional area of sample (m^2)

L = length of sample (m)

V_1 = volume upstream reservoir (m^3)

V_2 = volume downstream reservoir (m^3)

Hence the permeability of the sample may be found by plotting a graph of the natural logarithm of (p_1 - p_f) or (p_f - p_2) against time. The gradient of the resulting line is equal to -λ, and the permeability can be found from equation (Eq. 2.25), where it is the only unknown. Figure 2.21 shows the typical experimental trend obtained using the pulse transient method, following the procedure just described.

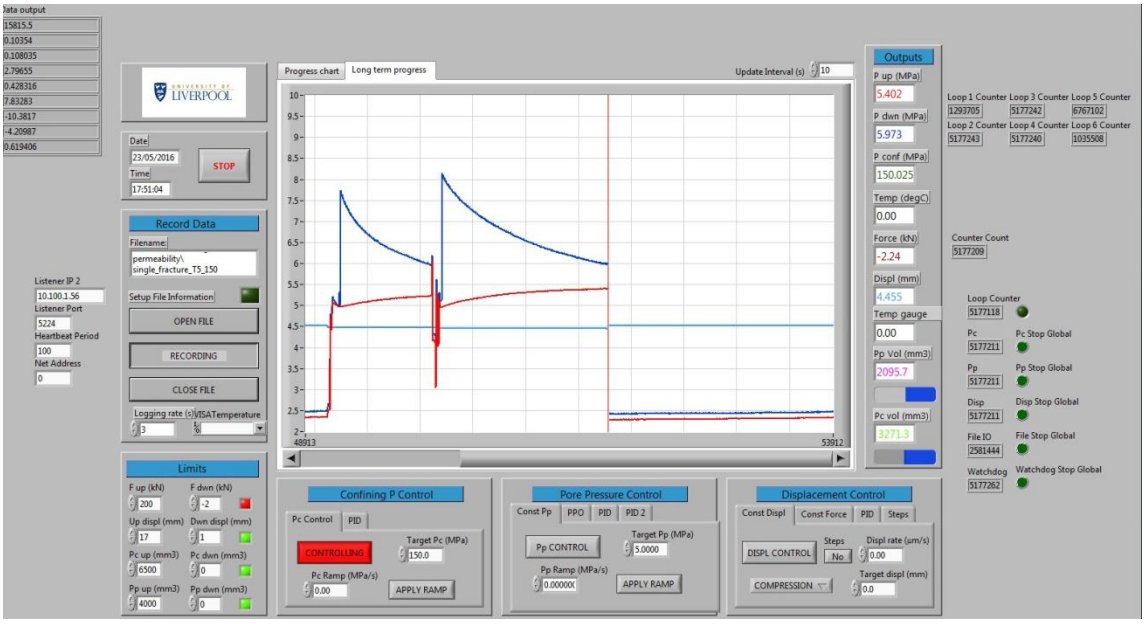

Figure 2.21: Screenshot of LabVIEW 2014 software during permeability measurements.

2.3.6.3. Limitations in permeability measurements

As already mentioned, the solutions for the diffusion equation (Eq. 2.25) have been derived for transient pulses in pressure, assuming zero storage of the sample (Trimmer, 1981; Hsieh et al., 1981; Lin, 1982). However, Trimmer (1981) recognized that if the ratio between the sample pore volume and the reservoir volume is less than 0.25, then a systematic error of less than 10% results from the statement that the sample storage capacity is zero, and that equations (Eq. 2.22) and (Eq. 2.23) hold reasonably well.

Knowing that a representative porosity of the sample used in this study is approximately 1%, under testing conditions, the ratio of the sample pore volume to the reservoir volume is always less than 0.25. Thus there will be a systematic error present in all permeability measurements made using the pulse transient method in this work, but it will be less than 10%. These errors were considered acceptable in the present work since the methods described for obtaining a complete solution to the diffusion equation involve curve fitting and optimization of the experimental apparatus for measurement of either the permeability or the storage capacity (Hsieh et al., 1981; Lin, 1982; Trimmer, 1981). Therefore, no attempts were done to account for finite values for the storage capacity.

Moreover, another potential error during the permeability measurements is due to the temperature changes. The experiments normally were performed at room temperature, around 20°C. Temperature decrease during occasional overnight measurements (or pauses) affected the pressure measurements, but without significant influence on the accuracy of the permeability data.

2.3.7. PERMEABILITY MEASUREMENTS THROUGH A SINGLE FRACTURE

The cores were prepared as described previously (Section 2.1) applying an axial stress using a modified Brazilian test apparatus at a very slow axial strain rate inducing a

macro-fracture in the sample. Then the samples were jacketed. Great care was taken to ensure that the halves of the macro-fractured samples were fully mated with no shear offset.

The target of this experiment is to understand with which rate the fluid can flow through a single fracture subjected to increasing confining pressure and overall when the fracture is totally closed, making the fracture impermeable.

The permeability measurements were performed as a function of confining pressure and using the transient method described before (Section 2.2). In this case axial load was not applied, the pore pressure was kept around 5 MPa, and the confining pressure was increased step by step up to 150 MPa. This experiment is based on the procedure of Nara et al. (2011).

2.3.8. SEM AND XPL OPTICAL MICROSCOPE OBSERVATIONS

An optical microscope and a scanning electron microscope (SEM) were utilized to study the microstructures of the greywackes and their mineralogy. Comparisons between greywacke samples with natural fractures and induced fractures from laboratory experiements have been done in order to discover potential similarities and thus provide insight into greywacke fracture dynamics. In addition, the percentage of minerals, and the grain size and the shape of minerals were documented using the XPL optical microscope. The percentages estimated with the microscope using XPL are subject to a small error because the Dott Sandstone Classification method, which has been utilized in this case, is not a precise method and it introduces the propagation of the error.

CHAPTER 3:
LABORATORY RESULTS
AND DISCUSSION

Chapter 3 of the thesis is targeted to give a clear idea about the characteristics of the greywacke rocks based on laboratory testing, which is reported in the first section of this chapter, and in the second section the data obtained during the experiments will be discussed and they will be put in context with previous data from other authors.

In New Zealand, the "greywacke" definition is applied to the very well indurated, slightly metamorphosed, interbedded mudstone and muddy sandstones that make the basement rock of the country.

The tests that have been carried out (Tables 3.1 and 3.2) are targeted to describe the physical properties of this material and their relation to fluid flow. Data on strength, seismic wave velocity, permeability, and porosity have been acquired, and are accompanied by information about the rock composition. Graphs and pictures will be shown in this part as examples, with the purpose to support what is written and to give a better idea on the data.

In a second section the results will be discussed and comparisons of the results are made with the purpose to give better comprehension of the similarities or differences between previously acquired data and the new data generated during this work. The interpretation of the laboratory results is the main way to characterize the greywacke basement in TVZ, in terms of physical properties.

3.1. LABORATORY RESULTS

The laboratory results are illustrated in these sections. Subsections are focused to evidence every kind of study that has been made in this project, describing the in details the characteristic of this greywacke sandstone.

The objectives of the petrological investigation are to characterize the intact greywacke rock (mineralogy, modal proportions, grain size) and natural fractures (width, fill, fragments). In addition, experimental deformation features, shear fractures developed during the triaxial testing, and the style of fracturing from the Brazilian tests, are described for comparison with observed natural deformation features.

The five thin sections examined here are of three different greywacke samples from three separate sites: Taotaoroa Quarry (three thin sections, same greywacke sample), Blue Rock Quarry and Waotu Quarry, which are all different lithological units.

3.1.1. GREYWACKE

Greywacke sequences, following Begg & Mazengarb (1996), generally consist of interbeds of:

- Sandstone: from coarse to medium grained, and from medium to dark grey. The individual grains are poorly sorted and consist of angular quartz and feldspar, plus lithic fragments of metamorphic and igneous rocks. The intergranular filling consists of clay minerals formed during induration or low grade metamorphism.

- Mudstone: layers of clay, silt or mud, generally dark to black in color, although occasionally red when there is a high content of iron bearing minerals.

The proportions between mudstone and sandstone are spatially variable.

Sample	Uniaxial	Triaxial	Brazilian	Vp - Vs	Porosity	Permeability	Thermal	SEM	XPL	S.F.	Density
WHGW_11_3									✓		
BRGW_11_2									✓		
TTGW_11_3_H1160									✓		
TTGW_11_3_H1161									✓		
TTGW_11_3_4_triax		✓		✓	✓	✓		✓	✓		
TTGW_11_2_1	✓										
TTGW_11_2_2	✓										
TTGW_11_2_3	✓										
TTGW_11_2_4	✓										
TTGW_11_3_1					✓						
TTGW_11_3_2					✓						
TTGW_11_3_3					✓						
TTGW_11_3_5					✓	✓ (x18)				✓	
TTGW_11_3_6	✓				✓						
TTGW_11_3_7					✓						
TTGW_11_3_8			✓ (x3)		✓						
TTGW_11_3_10				✓	✓						

Table 3.1: This table is a detailed list of what tests have been applied and on which sample. The abbreviation "S.F." indicates "Single Fracture", namely the samples on which the single fracture has been created and tested. The numbers between brackets (e.g. (x3)) indicate the number of the same test on that sample.

Sample	Uniaxial	Triaxial	Brazilian	Vp - Vs	Porosity	Permeability	Thermal	SEM	XPL	S.F.	Density
TTGW_11_3_11	✓										✓
TTGW_11_3_12	✓			✓							✓ *
TTGW_11_3_13	✓			✓							✓
TTGW_11_3_14	✓			✓							
TTGW_11_3_16					✓						
TTGW_11_3_17					✓	✓ (x18)		✓		✓	
TTGW_11_3_18			✓ (x3)		✓						
TTGW_11_3_19					✓						
TTGW_11_3_20			✓		✓						
TTGW_11_3_21			✓		✓						
TTGW_11_3_22					✓						
TTGW_11_3_23			✓ (x2)		✓						
TTGW_11_3_therm							✓				

Table 3.2: This table is a detailed list of what tests have been applied and on which sample. The voice "Thermal" indicates all the thermal analysis that have been done, namely the "thermomechanical analysis" (TMA) and the "simultaneous thermal analysis" (STA). The sign asterisk (*) indicates the crack density calculation.

3.1.2. PETROLOGY

Petrological descriptions of the greywacke samples used in this study are made using an optical microscope and a scanning electron microscope (SEM). Utilizing the "Dott Sandstone Classification" we have established an indicative percentage of the ratio of grains to matrix (Table 3.3).

3.1.2.1. Natural microstructures

The Waipapa Greywacke samples studied in this work have a coarse grain size and an andesite-dacite composition (Downs et al., 2014; Milicich et al., 2016). In fact most of the lithic fragments observed in this work (~50-60%) have volcanic in origin.

Sample	Coarse Grains (%)	Matrix (%)	Quartz (%) (Coarse)	Feldspar (%) (Coarse)	Lithic Fragments (%) (Coarse)
WHGW_11_3	35	65	10	20	70
BRGW_11_2	55	45	30	20	50
TTGW_11_3_H1160	80	20	10	20	70
TTGW_11_3_H1161	80	20	10	20	70
TTGW_11_3_4_triax	80	20	10	20	70

Table 3.3: Composition percentages for five samples of greywacke from both Waipapa and Torlesse Terranes, including percentages of coarse grains vs matrix, and percentage amounts of quartz, feldspar and lithic grains, which are all related to the coarse grains only. For "coarse grains" in this work are ≥ 0.0625 mm (1/16 mm). These percentages are indicative of the composition of the rocks used for laboratory experimentation in this project and they are all approximated. The method utilized to determine percentage composition of the grains has been the Dott Sandstone Classification.

The sample WHGW_11_3 - Waotu Quarry (Waipapa Terrane) (Fig. 3.1) consists of a fine to medium-grained sandstone composed of sub-angular to sub-rounded quartz, feldspar, plagioclase, volcanic and siltstone clasts, surrounded by a fine to very fine (occasionally coarse), indurated, clay/silt matrix. The percentage for the coarse grains is 35%, and 65% for the matrix. The thin section of this greywacke sample presents: quartz (10%), feldspar (20%) and abundant lithic fragments (70%). The

volcanic clasts, which are made of ferromagnesian minerals likely pyroxene and hornblende, are also part of the lithic fragments together with big quartz grains (up to ~0.3 mm). This sandstone is matrix supported with some clasts present. Two fractures are present in this thin section. One is a large antitaxial vein, showing consistent width of ~2.4 mm. The fracture walls are very straight, smooth, and parallel to each other. The mineral fill in this fracture consists of assorted material; bigger quarz/feldspar grains (~0.8 mm) and a finer cement material (cryptogranular) of chlorite and clay minerals, likely the result of hydrothermal alteration. The quartz-feldspar grains in the fracture are larger in size compared to the grains of the rock. Looking at the grain size and composition of the filling, it is clear that the material within the fracture does not come from the rock, likely it is related to the fluid precipitation and/or to the growth of minerals. The fracture is totally sealed.

The second fracture observed has a tortuous and thin morphology, with a maximum width of ~20 µm. The fracture is sealed and the fill consists of very fine cement, the composition of which cannot be inferred from microscopy investigation.

Fractured, damaged mineral grains are observed in this greywacke thin section. They occur more frequently closer to the fractures. This greywacke sample visually has a very low porosity, though this is higher in comparison to the porosity in the filled fractures.

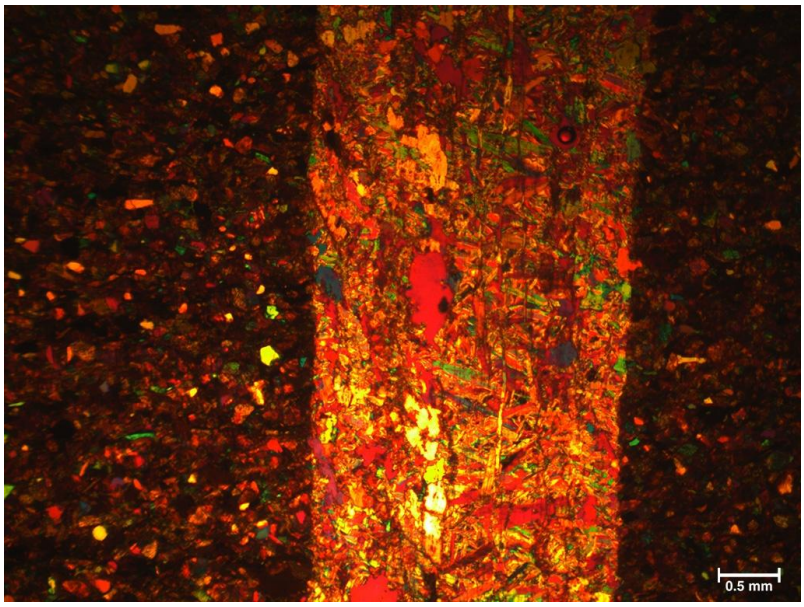

Figure 3.1: Crossed polarizers image acquired through XPL optical microscope, it shows the antitaxial vein in the thin section WHGW_11_3 and the composition of the rock and its grain size.

The greywacke sample BRGW_11_2 - Blue Rock Quarry (Torlesse Terrane) (Fig. 3.2) consists of a fine-grained sandstone composed of sub-angular to sub-rounded quartz, feldspar, plagioclase, volcanic and siltstone clasts, surrounded by a fine to very fine (sometimes coarse), indurated, clay/silt matrix. The percentage of coarse grains is 55%, while the matrix accounts for 45% of the sample. This thin section presents modal abundances of quartz (30%), feldspar (20%) and lithic fragments (50%). The lithic fragments consists of volcanic clasts made of ferromagnesian minerals, likely pyroxene and hornblende, and bigger quartz grains (0.1 mm - 0.3 mm). This sandstone is clast supported.

One fracture was observed within this thin section. It has a rough and thin morphology, with a maximum width of ~90 µm. The fill is a very fine-grained cement.

The greywacke minerals and grains show no preferential orientation in this sample except for the volcanic lithic fragments (Fig. 3.3 and Fig. 3.4) which show a preferred alignment. Fractured minerals have been observed without the thin section. This thin section visually shows a very low porosity. However, the porosity is higher than that of the filled fractures.

Figure 3.2: PPL image acquired through XPL optical microscope, it shows a natural fracture in the thin section BRGW_11_2 and the composition of the rock and its grain size.

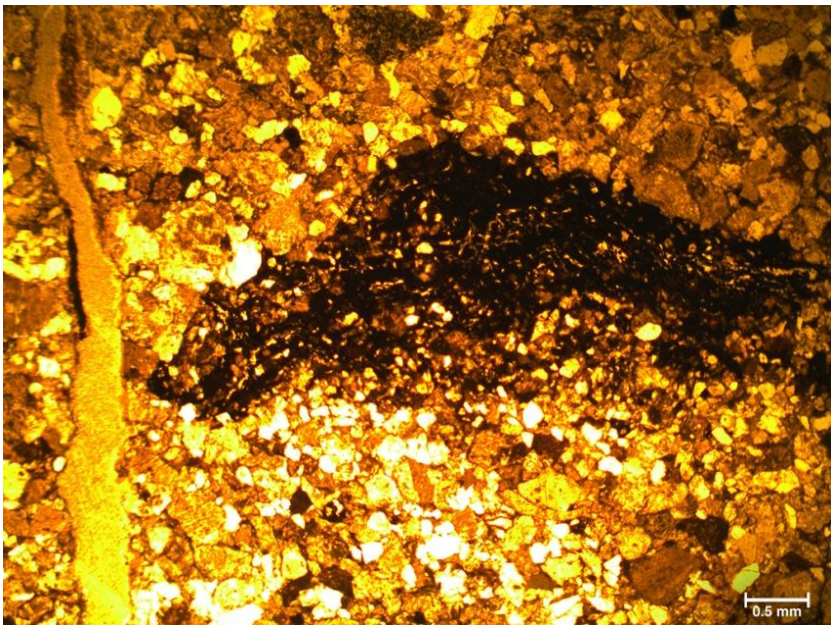

Figure 3.3: Image acquired in plane polarized light (PPL) of the thin section TTGW_11_3_4_triax after failure. It is evident the presence of a volcanic clast around 5 mm long. On the left side is visible the fracture created during the triaxial test.

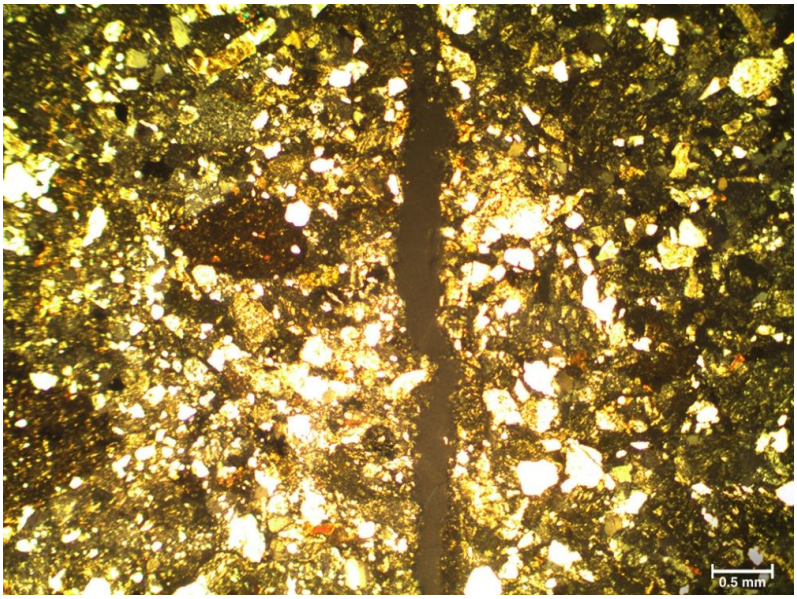

Figure 3.4: Image acquired through XPL with one polarizer inserted of a detail of the thin section TTGW_11_3_4_triax after the failure. It is evident the presence of volcanic clasts. In the center is visible the fracture created during the triaxial test.

The sample TTGW_11_3_H1160 - Taotaoroa Quarry (Waipapa Terrane) (Fig. 3.5) consists of a fine-grained sandstone composed of sub-angular to sub-rounded

quartz, feldspar, plagioclase, volcanic and siltstone clasts (often big clasts, >1mm), surrounded by a fine to very fine (occasionally coarse), indurated, clay/silt matrix. The percentage for the coarse grains (quartz (10%), feldspar (20%) and abundant lithic fragments (70%)) is around 80%, while for the matrix around 20%. Lithic fragments consist of volcanic clasts, composed of ferromagnesian minerals, likely pyroxene and hornblende, and together big quartz grains (up to ~0.5 mm across). This sandstone is clast supported and matrix poor. The matrix is thin and composed of indurated clay/silt.

Three fractures were found on this thin section. Two of them are parallel to each other and the distance between them is ~1 mm. The fractures are tortuous, rough, and thin in morphology, with a maximum width of ~80 µm for the smaller fracture, and ~150 µm for the larger one. The fill is a very fine calcite cement, however in several sectors the fractures have no aperture. The third fracture presents the same morphological characteristics of the others. From the thin sections it is evident that the volcanic clasts play an important role in relation to the propagation of the fractures such that the fractures do not cut across these volcanic clasts, implying they are stronger than the matrix and grains surrounding them.

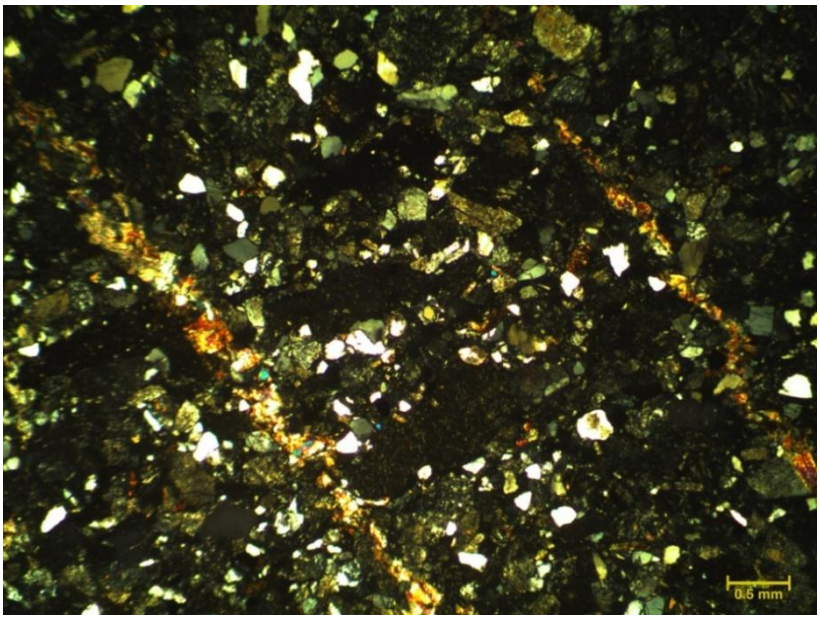

Figure 3.5: Cross polar (XPL) image acquired through XPL optical microscope, showing two natural fractures in the thin section TTGW_11_3 and the composition of the rock and its grain size.

The lithic fragments show a weak alignment, however there is no preferential orientation observed for the minerals or grains within this greywacke sample. Fractured minerals have been observed throughout the thin section. This greywacke sample thin section visually shows a very low porosity. However, the porosity is higher in comparison to the filled fractures.

The sample TTGW_11_3_H1161 - Taotaoroa Quarry (Waipapa Terrane) consists of a fine to medium grained sandstone composed of sub-angular to sub-rounded quartz, feldspar, plagioclase, volcanic and siltstone clasts (often big clasts, >1mm), surrounded by a fine matrix, sometimes till a coarse silt. The percentage for the coarse grains is 80%, while for the matrix 20%. It is assumed that the thin section presents: quartz (10%), feldspar (20%) and lithic fragments (70%). This sandstone is clast supported and matrix poor. The matrix is thin and composed of indurated clay/silt.

One fracture was found on this thin section. It is tortuous, rough and thin, with a maximum width of ~300 μm. The filling is fine cement, however in several sectors the fracture has zero aperture.

Moreover, there is no preferred orientation for the minerals or grains. Fractured minerals are present in the thin section. This thin section shows visually a very low porosity. However, the porosity is higher in comparison to the filled fractures.

3.1.2.2. Experimentally produced microstructures

The sample TTGW_11_3_4_triax - Taotaoroa Quarry (Waipapa Terrane) consists of a fine to medium grained sandstone composed of sub-angular to sub-rounded quartz, feldspar, plagioclase, volcanic and siltstone clasts (often big clasts, >1mm; the biggest: ~5mm length, ~2mm max width), surrounded by a fine matrix. The percentage for the coarse grains is 80%, while for the matrix 20%. The thin section contains: quartz (10%), plagioclase (20%) and lithic fragments (70%). This sandstone is clast supported and matrix poor. The matrix is thin and composed of indurated clay/silt.

A fracture was generated in this sample during a triaxial test (with constant confining pressure at 20 MPa). The fracture morphology is rough and it has a maximum width of ~0.7 mm. While there is no mineral precipitation in this artificially generated fracture, it is filled with cataclastic fragments over a length of ~6 mm (Fig. 3.6). The damage material that fills the fracture here has variable size, from cryptogranular cement to big grains (≥0.5 mm), which are themselves in turn fractured/damaged. On release of the pressure after the test, the damage material inside the fracture may have been moved, the same could have occurred during the sample preparation for SEM. A network of smaller fractures can be observed to have developed around the main fracture (Fig. 3.6).

Moreover, there is no preferred orientation for the minerals or grains of this greywacke sample. Fractured minerals have been observed in the thin section. This thin section shows visually a very low porosity. However, the porosity is higher in comparison to the filled fractures.

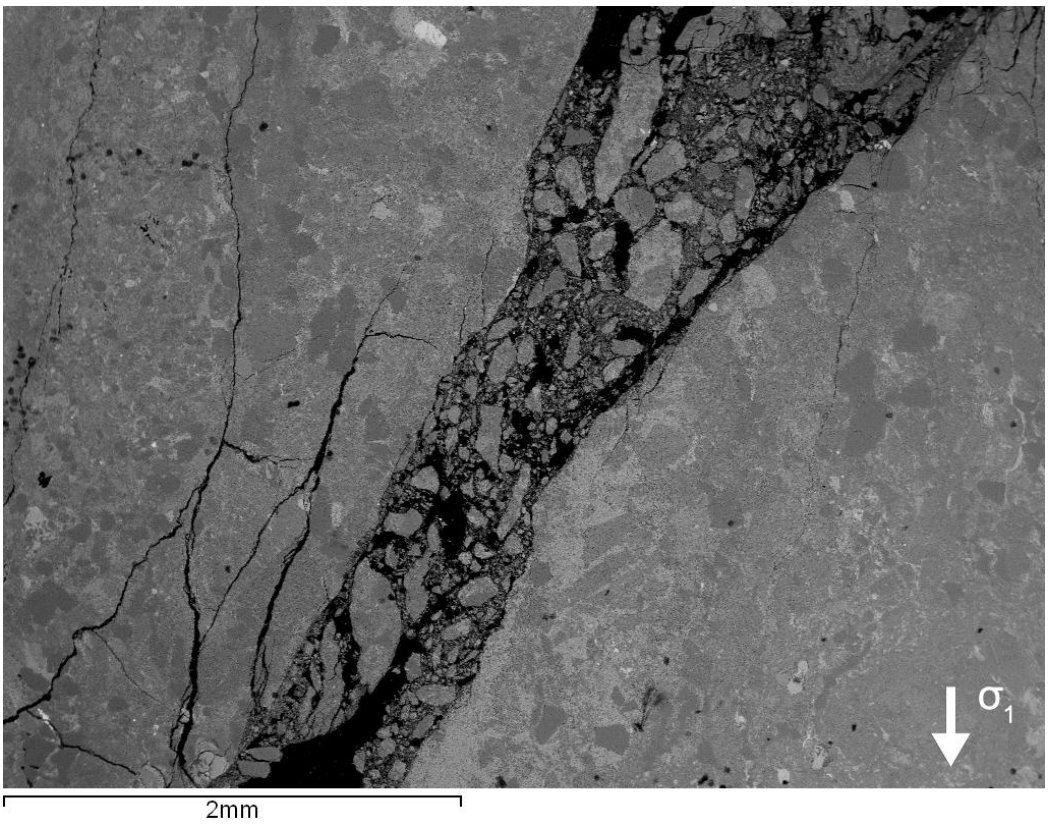

Figure 3.6: Image of thin section acquired through SEM, it shows an inducted fracture in the thin section TTGW_11_3_4_triax, its filling and the fractured zones. It has been obtained by triaxial test.

SEM observation of an artificially generated shear fracture in the greywacke sample TTGW_11_3_4_triax - (block) - Taotaoroa Quarry (Waipapa Terrane) (Fig. 3.7) allows the determination of the sense of shear (top to the left in Fig. 3.7). The generated fracture plane is at a ~30° angle with the core long axis, which corresponds to the main compressive stress (σ_1) direction.

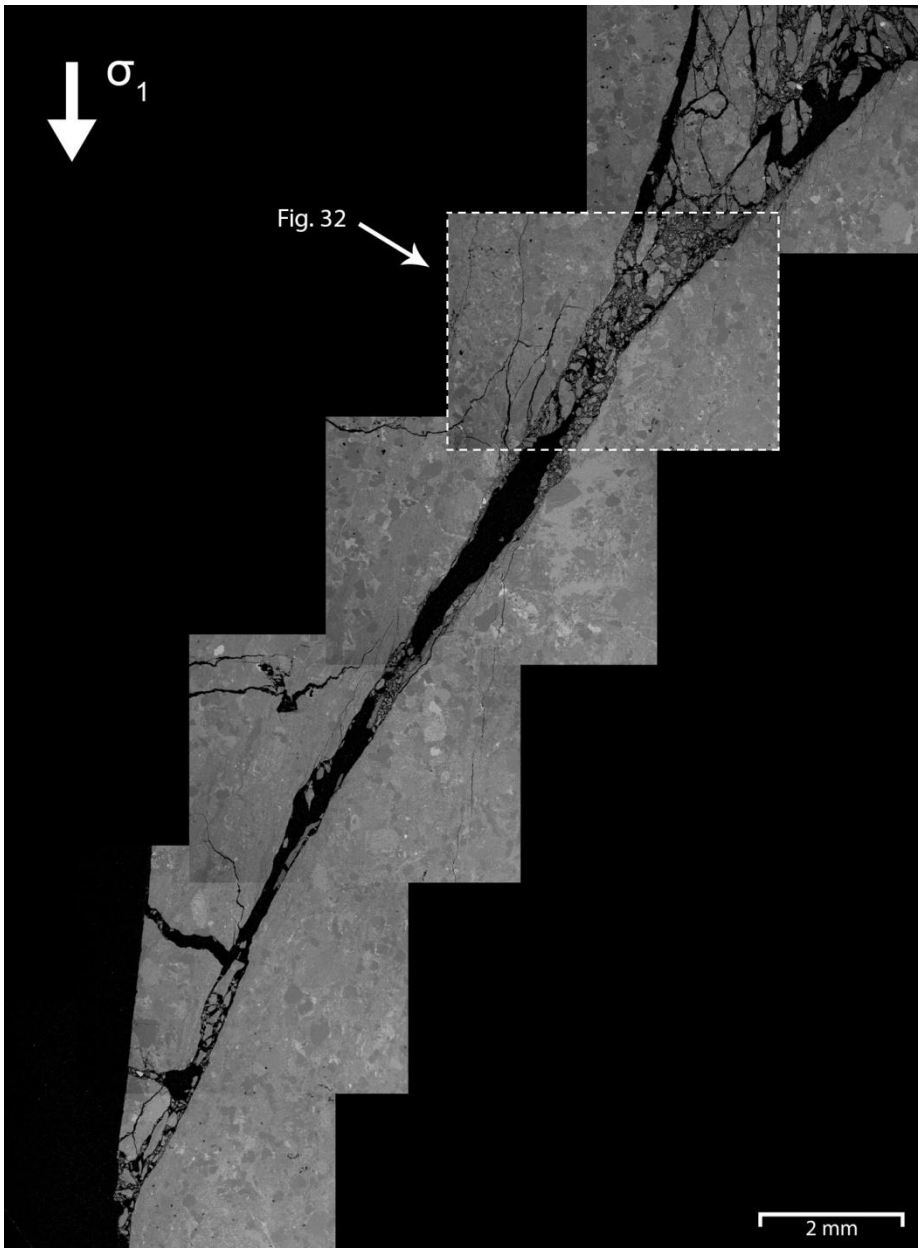

Figure 3.7: This image is the result of an assembly of images that have been acquired using the SEM. It shows an inducted shear fracture in the core TTGW_11_3_4 (the same core/fracture of Fig. 3.6), its filling and the fractured zones. It has been obtained by triaxial test.

The fracture is filled with damaged greywacke material generated during the failure of the sample under stress. The upper part of the fracture has a triangular shape, filled with large greywacke fragments, and with a finer matrix (from ~200 µm cement downwards). The fracture walls are alternatively rough and smooth, and overall the fracture displays low tortuosity. The maximum width of the fracture occurs in the triangular zone, which is ~3.5 mm wide. The porosity in the fracture is definitely higher than the filled and intact fracture, this has been observed visually.

A network of fractures develops on both sides of the main rupture, and often these smaller cracks intercept preexisting porosity elements of the greywacke sample. This fracture network is variable, and includes a wide single fracture, similar in appearance to the main rupture, as well as families of narrower cracks that propagate in the same direction as the larger structures. There is no obvious geometrical relation between the subordinate fracture network and the main fracture. In fact the minor fractures show a random orientation in all directions and different angles, variable length, width and shape.

The sample TTGW_11_3_17_braz - (block; Fig. 3.8) - Taotaoroa Quarry (Waipapa Terrane) was subjected to deformation in a Brazilian jig and a fracture was generated within it perpendicular to the main compressive stress σ_1. SEM investigation of the generated fracture shows that it is mostly unfilled, with just two fragments of the greywacke sample located at one end of the generated structure.

The fracture walls are alternatively tortuous and straight, and rough and smooth. The width along the whole structure is ~25 µm. There is no development of a damage zone or network of fractures around the main rupture, as is observed in the triaxial test, except for the central section where thinner fractures (~10 µm) can be observed. The length, as well as their width and shape of these subordinate structures, is variable.

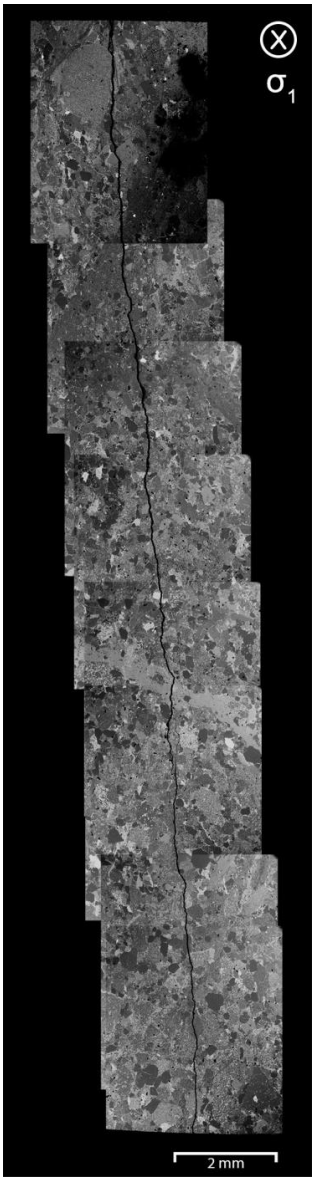

Figure 3.8: This image is the result of an assembly of images that have been acquired using the SEM. It shows an induced fracture in a greywacke disk (TTGW_11_3_17_braz) using the Brazilian jig. The image shows no fracture fill. The fracture looks linear and maintains constant thickness. There are no fracture networks or single fractures emanating from the main crack.

3.1.3. STRENGTH

In order to characterize the mechanical behavior of the Taotaoroa greywacke, several samples were loaded in compression to failure through uniaxial compression tests and Brazilian tests. A triaxial test was also performed, under a constant condition

of confining pressure where $\sigma_2 = \sigma_3$. In the following paragraphs the results obtained from these tests are shown. All the samples tested in this work show brittle failure. Understanding the strength of the rock and its behaviour in terms of stress and strain is important for predictions about the fracturing of the rock *in situ* and the reopening of filled fractures.

3.1.3.1. Uniaxial compressive strength (UCS)

From the uniaxial tests the stress applied on the samples and both axial and radial strain was recorded. The dataset shows a wide range of UCS, from 205 to 384 MPa for the 10 tested samples (Table 3.4). The general trend of stress-strain behavior of the greywackes is very similar for all the samples, as shown in Fig. 3.9. This figure shows the curves that best represent the overall dataset and behavior of the greywacke under uniaxial compression. The axial strain (red line) begins with a small and short upward trend, then it displays a very linear form up to failure (which occurred at ~220 MPa). The radial strain (green line) shows directly a linear trend to failure. The volumetric strain (blue line) is the result of both axial and radial strain (determined as described by Equation 2.4). Static Young's moduli (determined as described by Equation 2.5) range between 54 and 85 GPa and static Poisson's ratios (determined as described by Equation 2.6) vary between 0.19 and 0.36. The elastic region 40-120 MPa has been chosen as a range in which the elastic properties are calculated. In the Table 3.4 the elastic properties determined from the uniaxial tests are summarized. The value of failure for each sample is also stated. The series identified as TTGW_11_2 shows lower values of failure than the series TTGW_11_3. These two series of samples come from two different blocks of greywacke from the same quarry (Taotaoroa), the only difference is that the TTGW_11_2 appears more fractured (filled fractures) than the other.

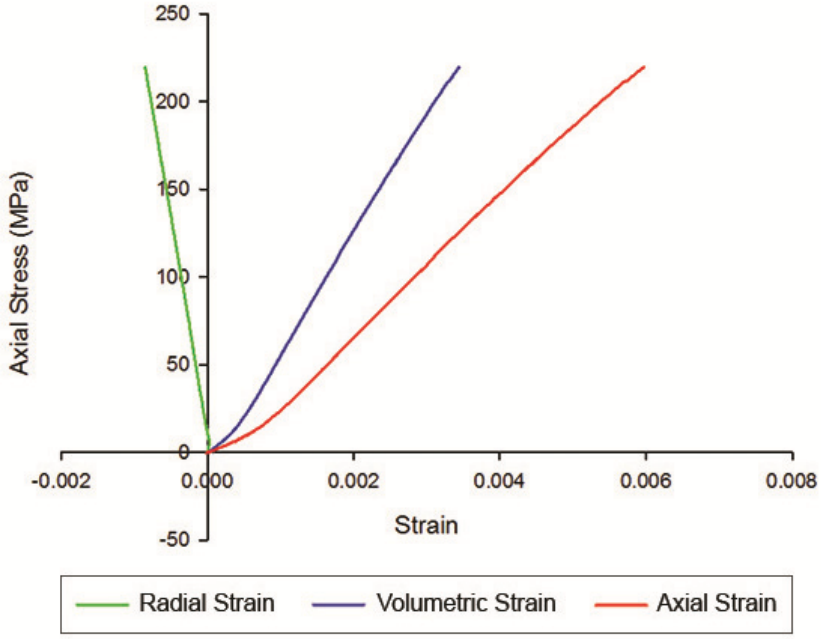

Figure 3.9: Stress-strain curves obtained from the uniaxial test of the greywacke sample TTGW_11_2_2.

Sample	UCS (MPa)	Young's Modulus (GPa)	Poisson's Ratio
TTGW_11_2_1	205.12	54.6	0.19
TTGW_11_2_2	219.58	71.05	0.215
TTGW_11_2_3	240.57	67.02	0.542
TTGW_11_2_4	239.13	68.08	0.345
TTGW_11_3_1	384.57	82.37	0.333
TTGW_11_3_6	353.45	85.79	0.364
TTGW_11_3_11	317.6	74.25	0.221
TTGW_11_3_12	265.9	68.03	0.285
TTGW_11_3_13	312.16	77.92	0.306
TTGW_11_3_14	346.18	78.61	0.359

Table 3.4: For every sample tested in the uniaxial test are shown the UCS and the elastic property values. The Poisson Ratio for the sample TTGW_11_2_3 appear high, probably probably due to slip along existing fractures (Blake and Faulkner, 2016). Sample variability of uncertainty no more than: UCS = 31.1% ; Young's Modulus = 21.4% ; Poisson's Ratio = 55.7%.

Property	Waipapa Terrane Greywacke	# of Tests
Tensile Strength (MPa)	14.37 - 32.42	10
UCS (MPa)	205 - 384	10
Poisson's Ratio (υ_{Stat})	0.19 - 0.54	10
Young's Modulus (E_{Stat}) (GPa)	54 - 85	10
Poisson's Ratio (υ_{Dyn})	0.28 - 0.30	3
Young's Modulus (E_{Dyn}) (GPa)	80 - 84	3
Density (ρ) (kg/m^3)	2.727	3

Table 3.5: Summary of elastic properties from uniaxial tests and tensile strength range values. Static and dynamic properties are identified in this table with the subscript "Stat" and "Dyn" respectively; in the rest of this thesis, if the elastic properties are mentioned without the subscript it means that it is referring to the static values. The value of the density is an average obtained from three greywacke cores.

Property	Waipapa Terrane Greywacke	# of Tests	Torlesse Terrane Greywacke	# of Tests
Tensile Strength (MPa)	20.3 - 35.7	8	-	-
UCS (MPa)	301 - 310	2	164 - 225	2
Poisson's Ratio (υ)	0.28 - 0.29	2	0.11 - 0.17	2
Young's Modulus (*E*) (GPa)	65 - 70	2	23 - 60	2

Table 3.6: Summary of static elastic properties from uniaxial test, UCS and tensile strength range values achieved by McNamara et al. (2014).

3.1.3.2. Tensile Strength

The dataset shows a large range of tensile strength, from 2.51 to 32.42 MPa for 10 samples. The value for the sample TTGW_11_3_20 should not be considered for statistical reasons because 2.51 MPa is too far out of the range. Probably it is due to the fractures contained within this sample.

However, studies about the precision and reproducibility have been made by ASTM testing multiple specimens of different rocks (ASTM, D3967 - 08). They calculated that the probability that two tests obtained in the same laboratory and on the same material will not differ by more than the repeatability limit - around 95%. The same probability, around 95%, applies to two tests obtained in different laboratories on the same material. To give a reference point, the following table (Table 3.7) shows four examples of tested lithologies by ASTM in relation to the repeatability limit and reproducibility limit.

Splitting Tensile Strength (MPa)	**Berea Sandstone**	**Salem Limestone**	**Tennessee Marble**	**Barre Granite**
Average Value	3.85	4.92	9.39	13.66
Repeatability Limit	1.24	1.56	3.63	4.31
Reproducibility Limit	1.37	1.74	5.38	4.98

Table 3.7: Values of splitting tensile strength for the average values, repeatability limit and reproducibility limit of several rocks tested by ASTM (ASTM, D3967 - 08).

Sample	Tensile Strength MPa
TTGW_11_3_8a	14.37
TTGW_11_3_8b	20.80
TTGW_11_3_8c	25.73
TTGW_11_3_18a	32.42
TTGW_11_3_18b	18.20
TTGW_11_3_18c	23.7
TTGW_11_3_20	2.51
TTGW_11_3_21	20.44
TTGW_11_3_23a	28.15
TTGW_11_3_23b	24.76
Average	**23.17**
Range	**14.37 - 32.42**

Table 3.8: Values in MPa from Brazilian test for each sample and as an average. TTGW_11_3_20 has been removed from the calculation for statistic reasons (Sample variability of uncertainty: 64.5%). Considering all the measurements the sample variability of uncertainty will be 70.9%.

The variability of values in tensile strength tests is very common (Gale and Holder, 2008), in fact the tensile strength data of this project show variable values (Table 3.8). They corroborate the results obtained by McNamara et al., (2014) on Waipapa greywackes (Table 3.6), which show to be strong rocks also looking at the tensile strength.

3.1.3.3. Triaxial compressive strength

During the measurement of the compressive strength under triaxial conditions, other measurements on the greywacke sample were performed. Overall the test lasted eight days, due to the slow loading rate chosen, the measurement of V_p and V_s for every step (Section 2.3) and, primarily for the measurements of permeability. Since the Waipapa greywacke is a quite impermeable rock, permeability measurements (Section 2.3) took around 50 hours to make. Hence, there are pauses in the loading and data

collection. These are shown by shifting of the line in several points, and the most evident of them is at ~120 MPa axial stress (Fig. 3.10 and Fig. 3.13). Mainly it is associated with the change of the temperature conditions in the laboratory while keeping the sample in the rig overnight (Fig. 3.10 and Fig. 3.13).

The triaxial test was performed with a constant confining pressure of 20 MPa and a constant pore pressure of 5 MPa (effective pressure of 15MPa). Fig. 3.10 illustrates the differential stress versus displacement for the triaxial test conducted on Waipapa greywacke. As it was found for the uniaxial tests, the stress-strain curves for these greywackes shows the typical behavior described previously.

In the beginning a hint of upward concavity is seen (Fig. 3.10), then the trend is very linear till the failure, which occurred at 314 MPa. The curve does not show a yield point (situation similar to what has been seen in the uniaxial curves), and after the failure the axial stress dropped to ~85 MPa. Therefore, after the failure in order to check the residual strength and the permeability, the core was loaded again up to ~1 mm of displacement. One further permeability measurement was taken. Finally, an extra force was applied to generate a further displacement of ~0.5 mm, with the same purpose of the previous displacements.

The total displacement (corrected for the elasticity of the machine) during the triaxial test reached 2.42 mm. The failure of the sample occurred at 0.187 mm (Fig. 3.10), then the reloadings occurred at 0.79 mm and 1.95 mm.

Also if the test does not show a yield point before the failure, the reloading shows the shear crack was reactivated. Moreover, a yield point is visible during the first reloading, at 120 MPa and for a displacement of 0.95 mm. The same behaviour occurred for the second reloading, from circa 139 MPa and 1.9 mm of displacement to 154.4 MPa and 2.39 mm of displacement.

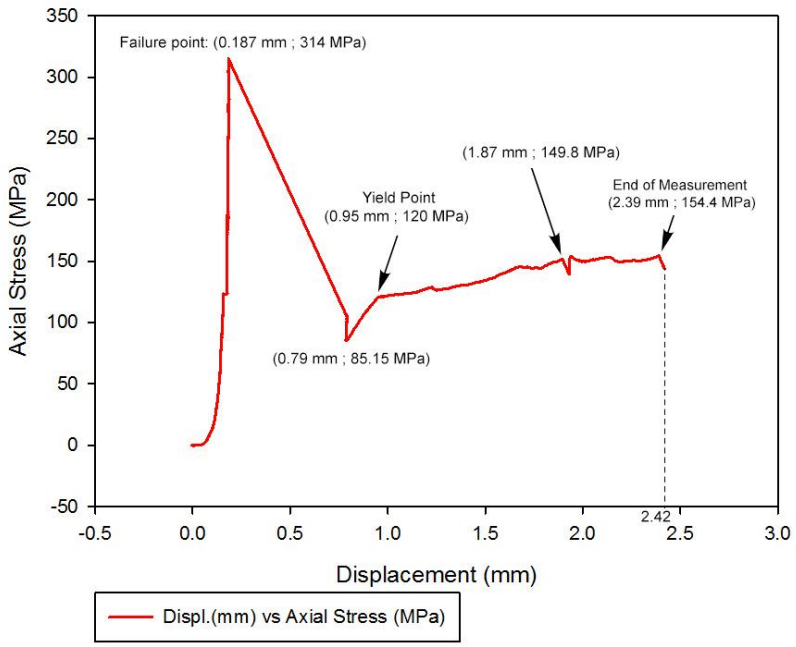

Figure 3.10: Stress-strain curve obtained from the triaxial test. The stress drop after the failure and the re-load phases are also shown.

Figure 3.11 shows the pore volume versus the differential stress. The volume is the amount of pore fluid that moves in or out of the sample during the deformation as measured by the volumometer and represents the connected crack volume. Assuming there is a relatively high density of connected microcracks in the sample, then it is possible to use the volume of water that enters or leaves the sample measured by the volumometer as a substitute for relative porosity change. Plotting the volume versus the differential stress it is possible to see the change in volume during the triaxial test.

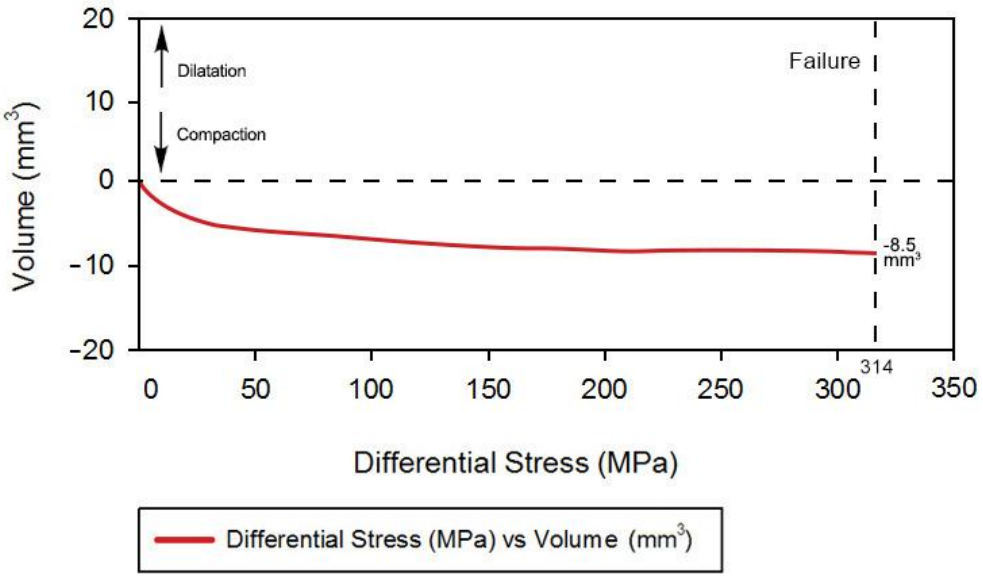

Figure 3.11: This graph shows the variation of the pore volume increasing the differential stress during the triaxial test. The data of this graph have been smoothed.

During the triaxial test, as the stress increases the volume varies negatively from 0 mm^3 to a final value of -8.5 mm^3. Thus, it has been observed a contraction phase, due to the increasing of the stress. The trend shows a constant decrease of pore volume which imply that there is no dilatation phase before the failure. In general, the reduction of the pore volume indicates compaction. The low variation of volume reflects a low crack density, and it is confirmed by the very low permeability and porosity.

3.1.4. PERMEABILITY AND POROSITY

This chapter is based on permeability measurements, which are fundamental data to understand the characteristics of the rock in the geothermal environment. The permeability measurements have been carried out for the greywacke sample during the triaxial test and for greywacke samples on which a macrofracture was artificially produced in order to understand the hydraulic flow through it under pressure. Moreover,

the porosity has been measured for 17 samples, including the two samples with the macrofractures (Tables 3.1 and 3.2).

3.1.4.1. Permeability and porosity data

The permeability measurements performed during the triaxial test have been carried out both before and after the failure of the core (with 15 MPa effective confining pressure conditions) (TTGW_11_3_4). In Figure 3.12, the blue coloured symbols correspond to the measurements taken during the experiment; the white symbols are the measurements effectuated after the failure of the core (Section 3.1). The permeability is plotted against differential stress (Fig. 3.12) and then versus the displacement (Fig. 3.13). These two graphs show a similar trend: the permeability begins almost at 10^{-21} m^2, then fluctuating it decreases to between 10^{-22} m^2 and 10^{-23} m^2, and finally before the failure the permeability corresponds to 10^{-17} m^2. Permeability values around 10^{-19} m^2 and 10^{-20} m^2 are also seen for the post-failure measurements (Fig. 3.12 and Fig. 3.14).

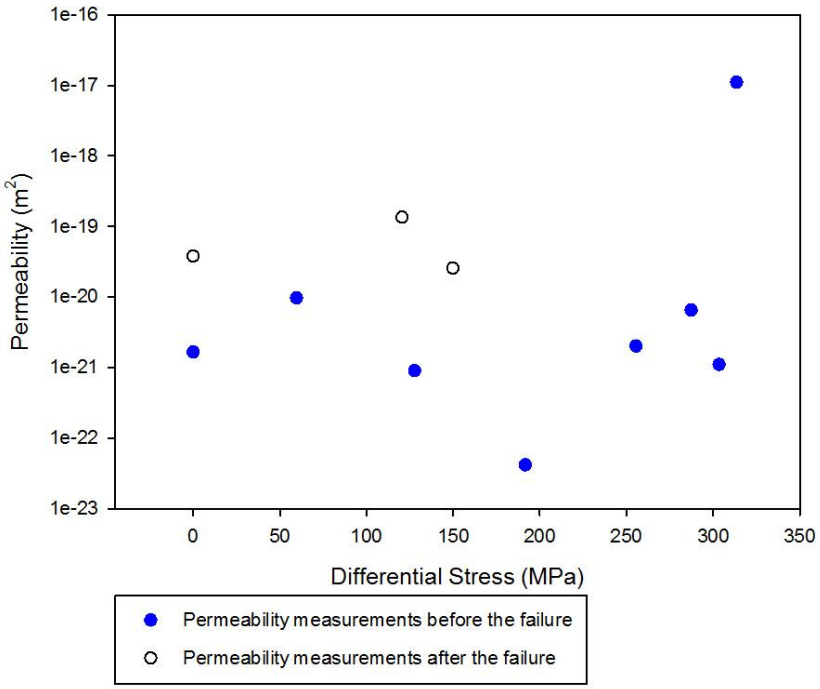

Figure 3.12: Scatter plot of permeability values measured during the triaxial test versus the differential stress. Both measurement series are illustrated, before and after failure.

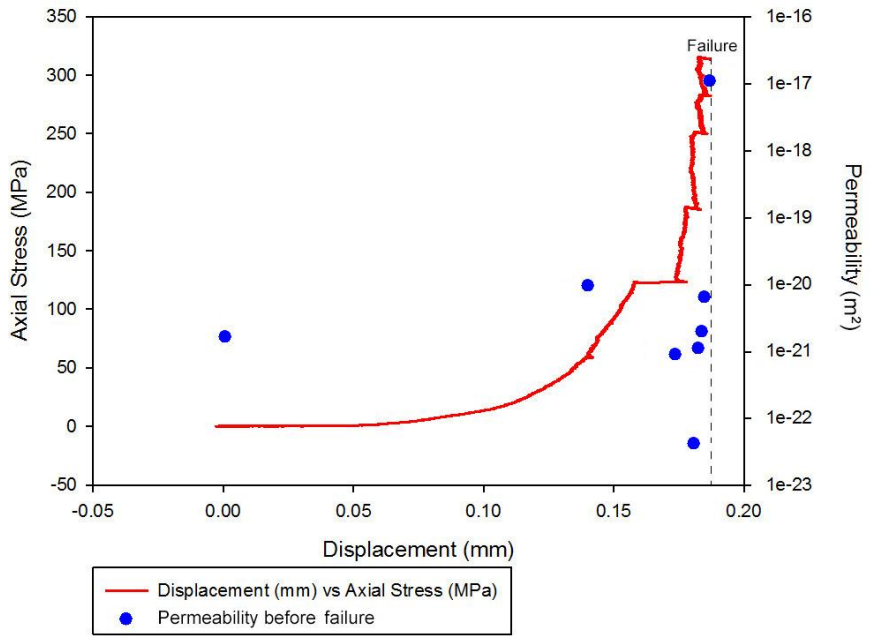

Figure 3.13: Scatter plot of permeability values measured during the triaxial test versus the displacement. The stress-curve is also shown in order to give better idea on the distribution of the measurements.

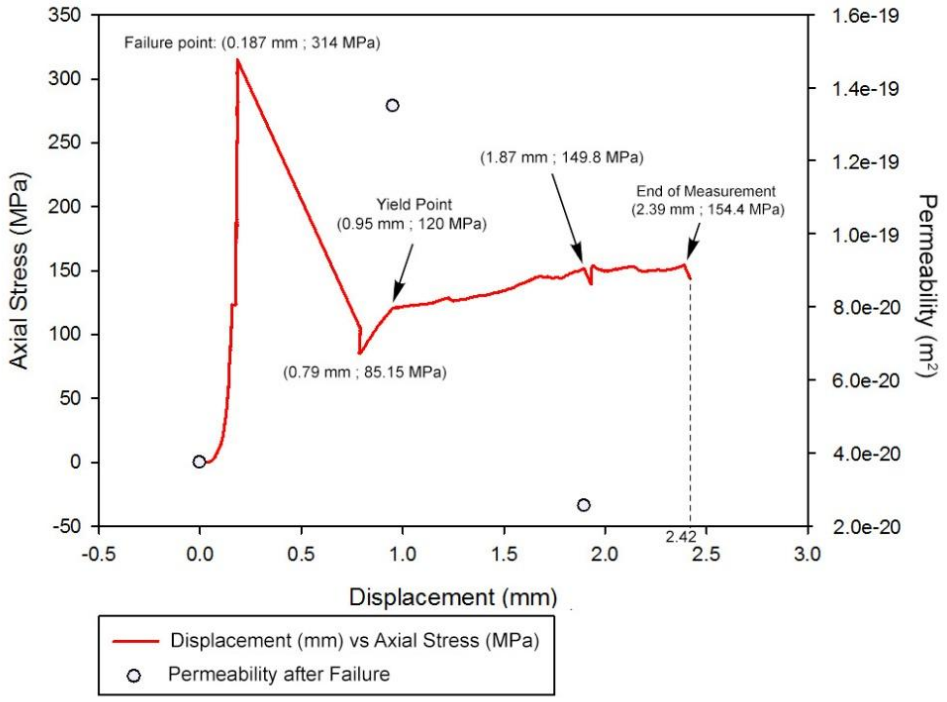

Figure 3.14: Scatter plot of permeability values measured during the triaxial test versus the displacement. The curve stress-strain from triaxial test is also plotted on in order to give a better reference to the evolution of the permeability.

Sample	Porosity (%)
TTGW_11_3_1	0.841 %
TTGW_11_3_2	0.953 %
TTGW_11_3_3	1.304 %
TTGW_11_3_4	1.040 %
TTGW_11_3_5	0.988 %
TTGW_11_3_6	0.889 %
TTGW_11_3_7	0.994 %
TTGW_11_3_8	1.146 %
TTGW_11_3_10	1.234 %
TTGW_11_3_16	0.924 %
TTGW_11_3_17	0.855 %
TTGW_11_3_18	1.215 %
TTGW_11_3_19	1.196 %
TTGW_11_3_20	0.874 %
TTGW_11_3_21	0.888 %
TTGW_11_3_22	1.071 %
TTGW_11_3_23	1.182 %
Average	**1.035 %**

Table 3.9: Values of connected porosity (vol%) for 17 samples of Waipapa greywacke. Sample variability of uncertainty: 22.4%.

3.1.4.2. Hydraulic conductivity of a single fracture

This test has been carried out for two samples having a cylindrical shape and on which an artificially generated, very thin fracture axially bisects the core (Section 2.1) (Nara et al., 2011).

In the graph in Fig. 3.15 are plotted confining pressure versus permeability for this generated fracture. It is shown that initially, while increasing the confining pressure, there is a decrease in permeability. The first permeability measurement has been performed at 40 MPa confining pressure, then a new measurement has been taken every

5 MPa till 110 MPa. After that, the measurements occurred at 120, 130 and 150 MPa. This has been done for two samples (TTGW_11_3_5 and 17; Fig. A24). Both samples reveal a similar trend, the first permeability measurement (at 40 MPa) results are between 10^{-16} m^2 and 10^{-17} m^2, and the last measurement (at 150 MPa) around 10^{-19} m^2.

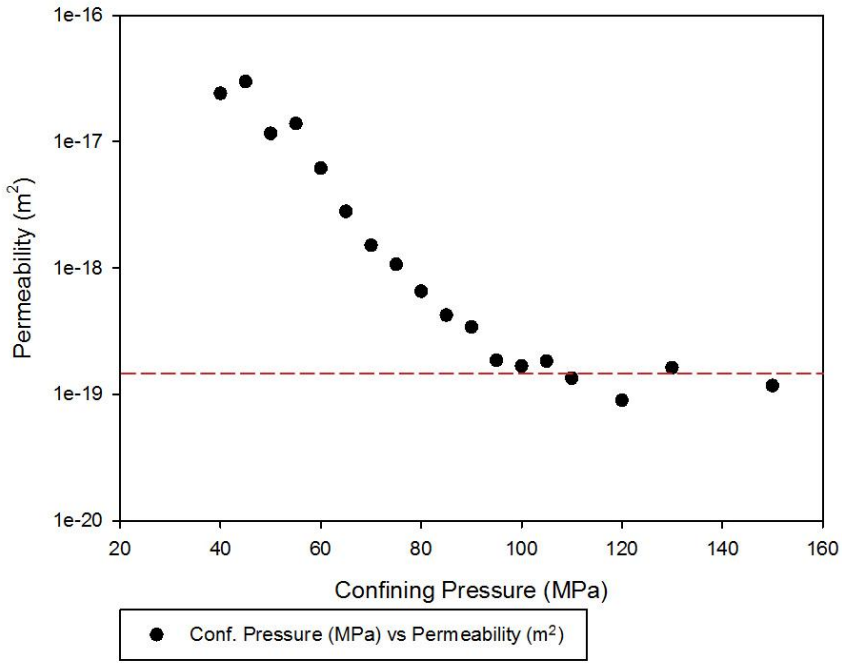

Figure 3.15: It shows the permeability through the single fracture of the sample TTGW_11_3_5. Every black spot is a measurement of permeability and can be noted how the permeability decrease increasing the confining pressure. The dashed line indicates where the permeability becomes stable, signing the moment whereby the fracture is closed (but not totally sealed).

3.1.4.3. Permeability models

Thermal fracturing and dissolution/precipitation depend on the temperature, confining pressure, fluid pressure and deviatoric stress (also if the deviatoric stress could work in the opposite way creating microcracks producing an increase of permeability). They promote the reduction of porosity and permeability through kinetic processes (Guéguen and Palciauskas, 1994).

It is essential to underline the importance of quantifying how different fracture populations can influence the permeability in the rocks. Furthermore, it should be highlighted that the permeability is not determined by the porosity, but by the porosity microstructure (e.g. the connectivity of the pore network).

To find the best model to calculate the permeability in the most accurate way, factors that influence the fluid flow must be considered. The difference is in the interpretation of what controls the value for permeability. Since in this case a single crack is studied, the suitable relation for the permeability of a crack Guéguen and Palciauskas (1994) is:

(Equation 3.1)

$$k = \frac{4\pi}{15} f \frac{\bar{w}^3 \bar{c}^2}{\bar{l}^3}$$

where:

k = permeability (m^2)
f = percolation factor
$\bar{w}$ = average of the half-widths of the apertures (μm**)**
$\bar{c}$ = average of the radiuses of the apertures (μm**)**
$\bar{l}$ = average of the distance between two cracks (μm**)**

The percolation factor f can change in relation to other two variables: p and p_c; where:

p = probability that two cracks are interconnected
p_c = percolation threshold

So, if:

$p < p_c$ then $f = 0$
$p \approx p_c$ then $f \sim (p - p_c)^2$
$p » p_c$ then $f = 1$

Equation 3.1 is applied supposing the presence of a crack population, and so it has to be modified to be applied for a single fracture. The problem is that the macrofracture cuts through the entire rock core, and hence the fluid does not flow through the whole surface but only through the fracture. Therefore, by varying the sample diameter and the aperture width, the cross sectional area will be varied but it will not represent the permeability calculated using Equation 2.25 that assumes the fluid flow occurs over the whole sample cross-sectional area. Hence for samples containing macrofractures, it means that the formula is scale-dependent.

However, I chose to determine the permeability for the single fracture using the formula of Equation 3.2, derived from Equation 2.25, so that a correlation between permeability values from the single fracture and the permeability values from an intact single core might be compared. In this way, the pressure at which macrofracture closure occurs can be easily recognized.

(Equation 3.2)

$$k = \frac{\lambda}{\left(\frac{1}{V_1}+\frac{1}{V_2}\right)}\left(\frac{\eta\beta L}{A}\right)$$

3.1.5. SEISMIC WAVES VELOCITIES

Studying the behaviour of seismic waves is useful in order to support studies concerning the mechanical behavior of rocks. Vp and Vs depend on the density and elastic properties of the materials (Schubnel et al., 2003; Vinciguerra et al., 2005; Nasseri et al., 2009) and are often related to other physical properties.

In this project the velocity of P and S waves have been acquired during the uniaxial and triaxial tests. Measurements were carried out under uniaxial stress conditions, hydrostatic conditions and triaxial stress conditions.

The following graphs (Fig. 3.16 and Fig. 3.17) are examples of the typical trend of Vp and Vs shown by Waipapa greywacke during uniaxial testing, while the graphs of Fig. 3.18 and Fig. 3.19 show the trends of Vp and Vs during the triaxial test under a confining pressure condition of 20 MPa. The data show an initial rapid increase in P and

S wave velocity as the differential stress is increased, after which the P and S wave velocities plateau and show little change up to the point of failure.

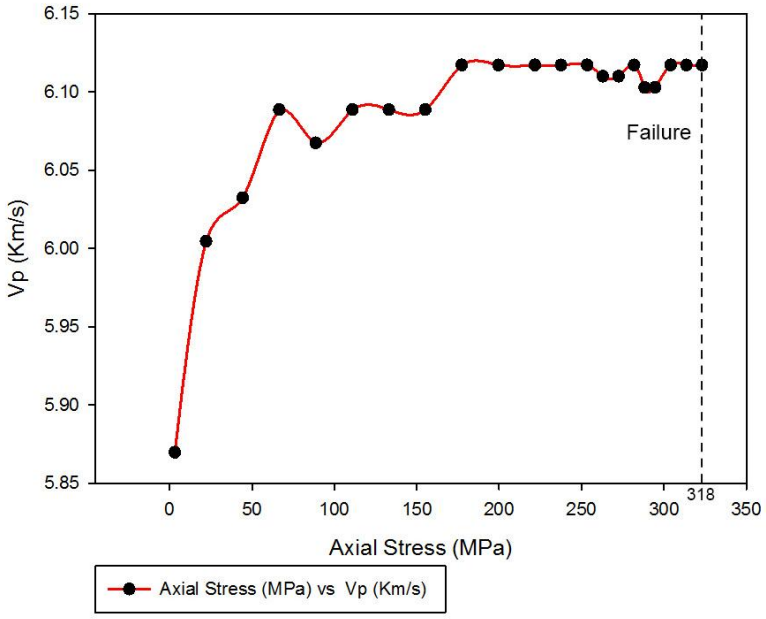

Figure 3.16: Velocities of P waves acquired during the uniaxial test for the sample TTGW_11_3_11.

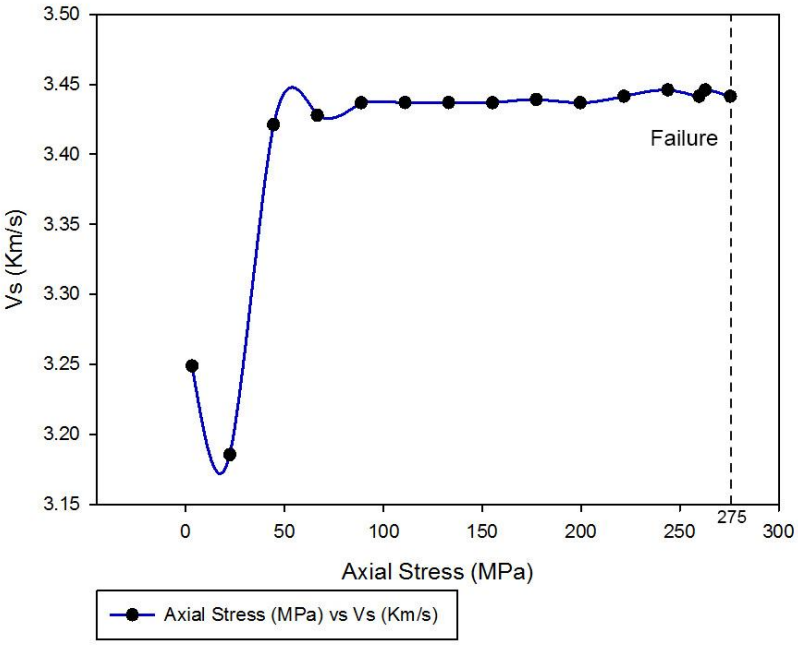

Figure 3.17: Velocities of S waves acquired during the uniaxial test for the sample TTGW_11_3_10.

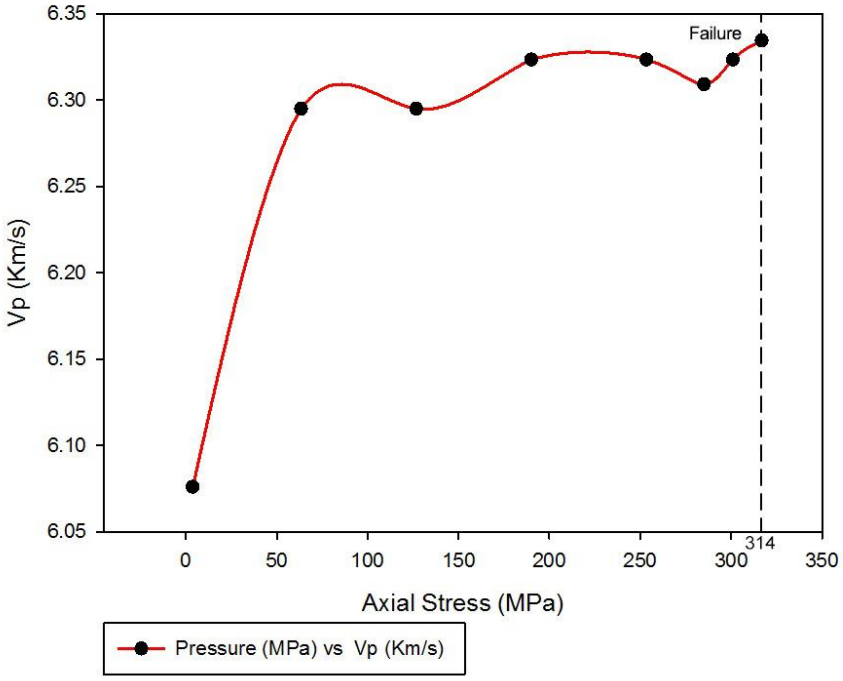

Figure 3.18: Velocities of P waves acquired during the triaxial test (20 MPa confining pressure) for the sample TTGW_11_3_4_triax.

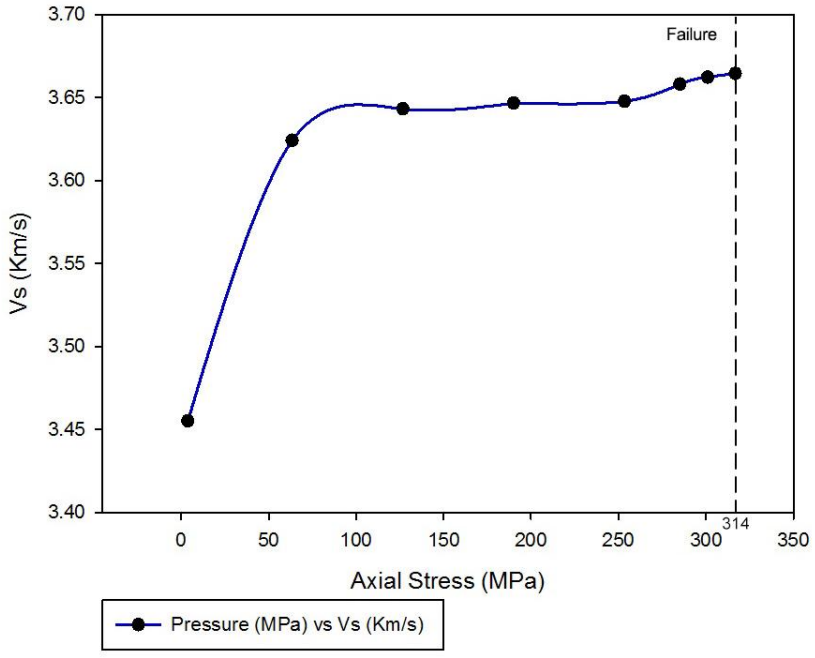

Figure 3.19: Velocities of S waves acquired during the triaxial test (20 MPa confining pressure) for the sample TTGW_11_3_4_triax.

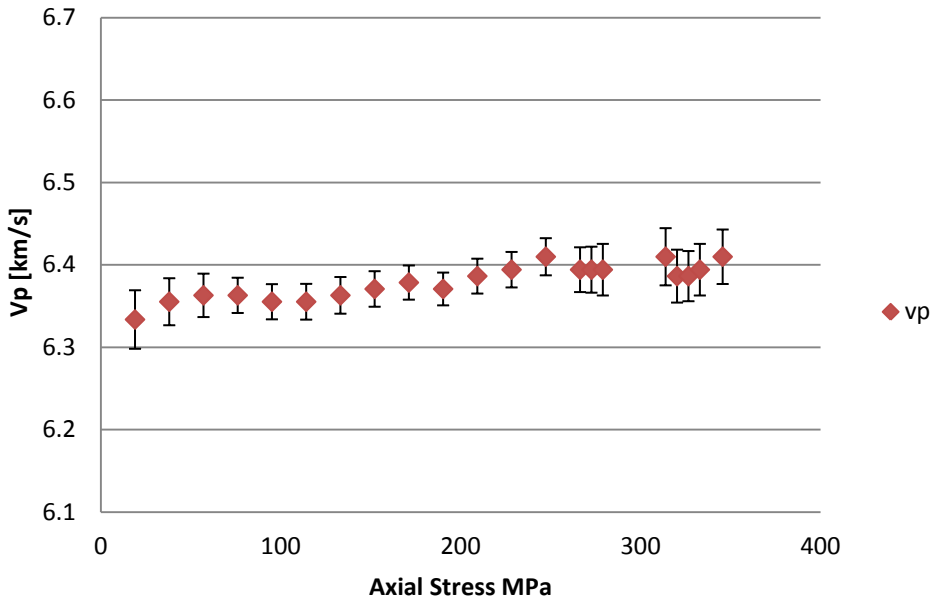

Figure 3.20: Graph showing the error bars in relation to the Vp measurements from the uniaxial tests.

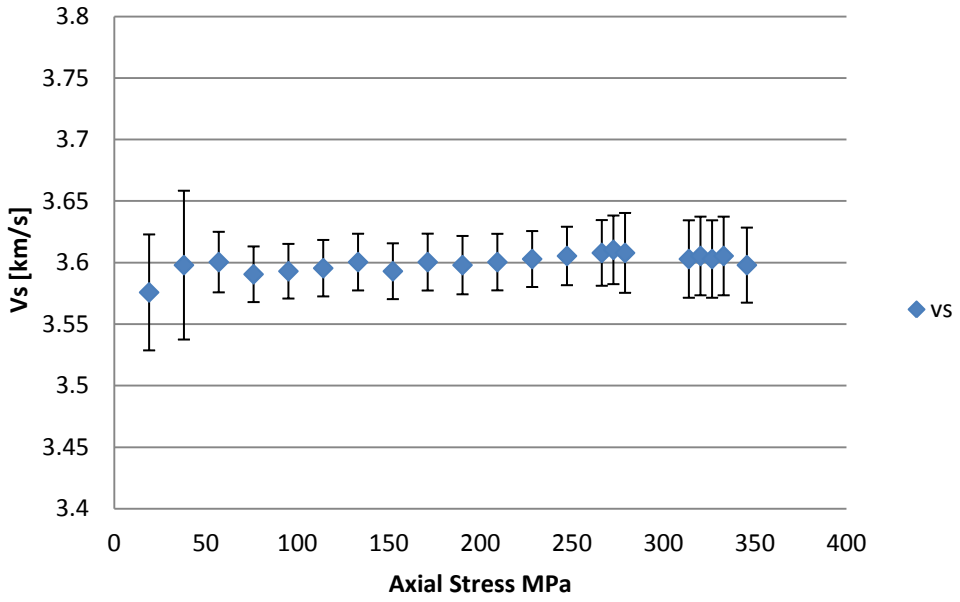

Figure 3.21: Graph showing the error bars in relation to the Vs measurements from the uniaxial tests.

3.1.6. THERMAL DEFORMATION

Knowledge of the thermal properties of geothermal reservoir rocks is indispensable to plan field projects that include considerations of wellbore stability, reservoir predictions, and stimulation procedures. To obtain information about the thermal properties in the geothermal reservoir, thermal measurements were carried out on core samples (Section 2.1) (from TTGW_11_3_therm) of Waipapa greywackes.

3.1.6.1. Greywacke thermal expansion coefficient

Physically, thermal expansion is the tendency of a material to change in shape, area and volume in response to a change of temperature, through the transfer of the heat.

The linear expansion coefficient is the fractional change in length per degree of temperature change. The linear expansion coefficient α is expressed as:

(Equation 3.3)

$$\alpha_L = \frac{1}{L}\frac{\delta L}{\delta T}$$

where:

L = reference length of the sample at initial temperature T_0;

δL = difference in length of the sample induced by temperature change;

$\delta T = T_1 - T_0$ where T_1 is the higher measured temperature (small change in temperature).

In order to obtain values of α, small (infinitesimal) ranges of δT and δL/L are measured at around a given temperature (Fig. 3.22 and Fig. A19).

600°C has been chosen as target temperature in relation to the geothermal gradient for the future aims of geothermal fields, which should reach depths till 6 - 8 km. The total change in length over this temperature range is 0.0334 mm.

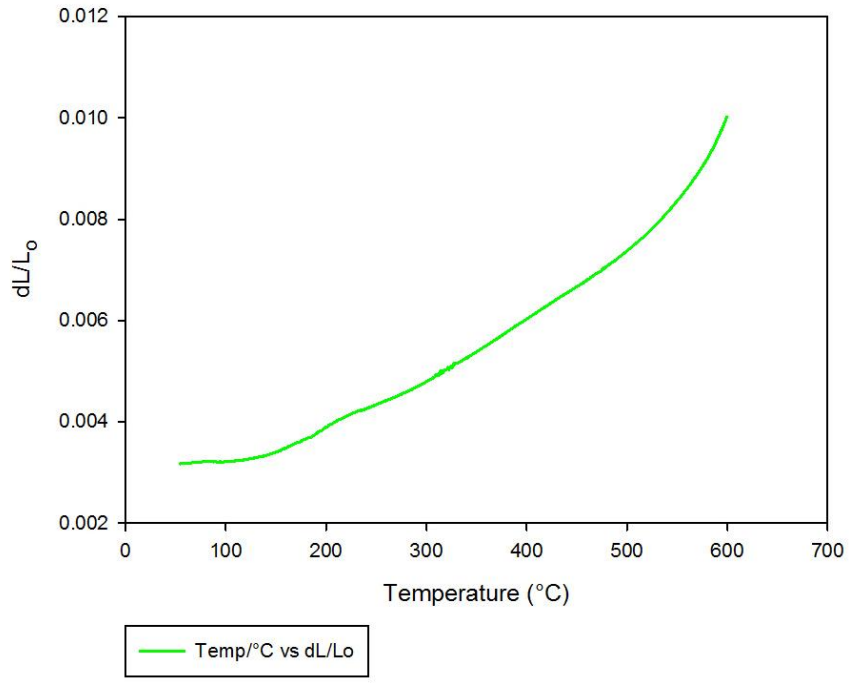

Figure 3.22: Linear displacement curves for Waipapa greywacke ($\delta L/L_0$) during linear thermal expansion testing.

From the thermo-analysis experiments (Section 2.3) graphs showing the variation of the linear thermal expansion coefficient (α) in relation to the increase of the temperature are plotted (Fig. 3.23 and Fig. A20).

From a starting temperature of 25°C the experiment was carried out to a temperature of 600°C. The variation of α is from 0 up to $5 \cdot 10^{-5}$ °C^{-1} and this progression evolves in an overall upward trend.

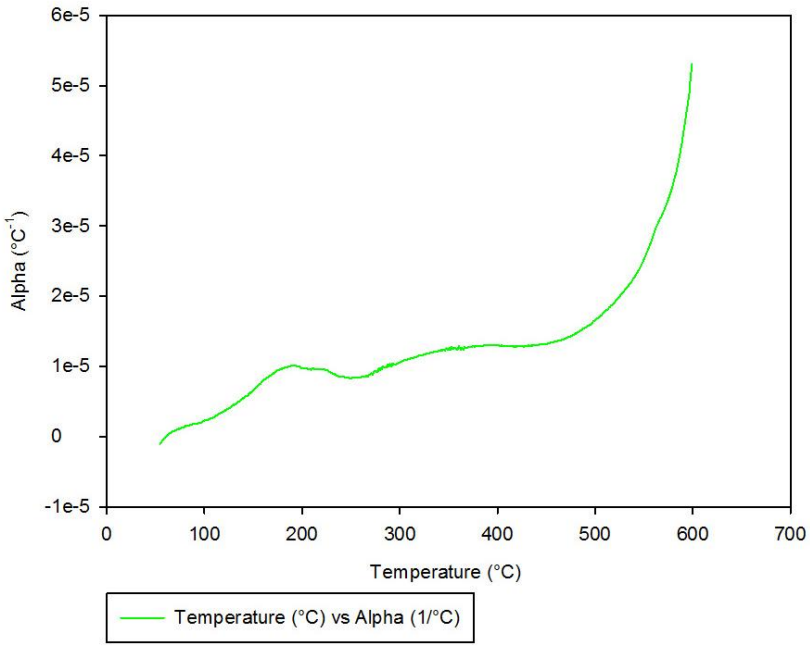

Figure 3.23: Linear expansion coefficient α for Waipapa greywacke plotted versus temperature.

3.1.6.2. Simultaneous thermal analysis

The thermogravimetric analysis (TG) shows the variation of the mass with the increase of the temperature (Section 2.3). The temperature has been raised to 1000 °C and then the cooling phase took place (Fig. 3.24).

To determine the precise nature of these reactions, a reference to the component major minerals that make up the Waipapa greywacke must be made. Optical and geochemical analysis (established through SEM analyses) of the greywacke indicate that quartz and clay minerals, predominantly chlorite, are important components of the hydrothermally altered rock (Section 3.1). A relevant presence of calcite has also been detected in veins through optical and electron microscopy (Section 3.1).

The greywacke displays relative mass stability from the beginning of the test at 25°C to the commencement of significant mass loss at around 580°C.

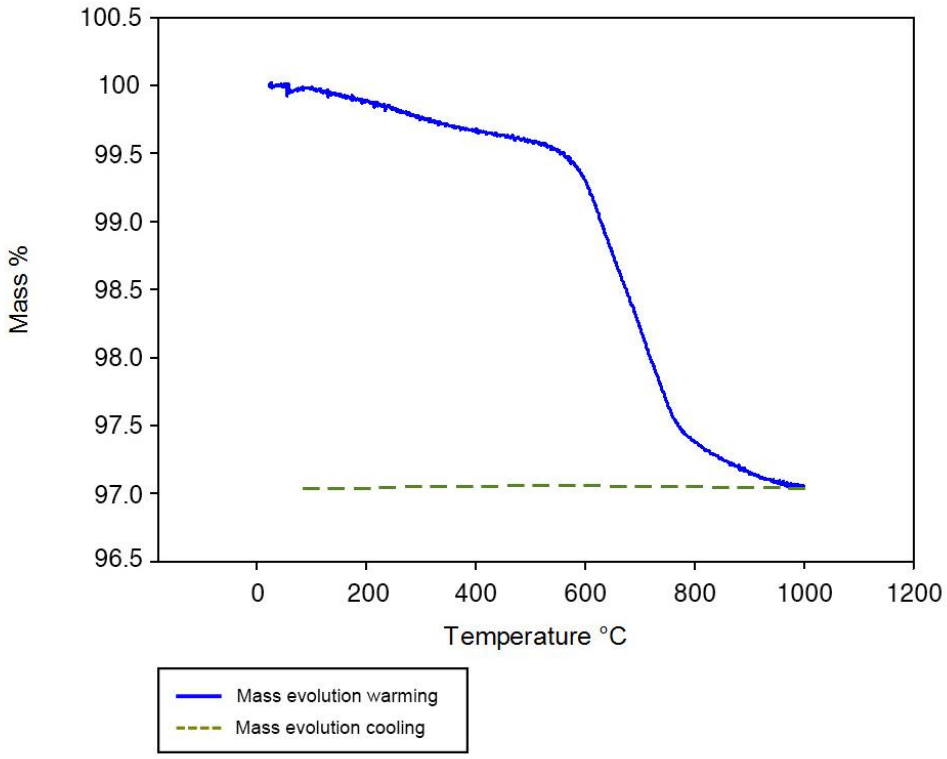

Figure 3.24: Thermogravimetric analyses. As temperature is increased, mass is lost. There is no variation of mass during the cooling phase.

The ~0.5% of the mass lost till here (Fig. 3.24) could be due to the release of water content from clay minerals, such as chlorite, which notoriously breaks down around 350 - 400°C (Grim, 1968). After that, the mass continues to decrease with a steeply sloping until it becomes stable around 1000°C. In this second stage the mass lost is ~2.5%. This endothermic reaction can be identified as decarbonization of calcite, with CO_2 released. Then the cooling phase starts, represented by the horizontal line from right to left, which represents the decrease of the temperature and the (possible) change of the mass, which does not occur.

The specific heat capacity (or just specific heat) is the ratio between the heat added to (or removed from) an object and the resulting temperature change per unit mass of a material ($\frac{J}{g \cdot K}$) (Halliday, David; Resnick, Robert; (2013)). The specific

heat capacity was calculated at constant pressure (Cp) and it shows a variation from 550°C to 800°C (Fig. 3.25) with an upper limit of 2.0 J/(g·K). The specific heat capacity starts to become stable apart from a further small variation that occurs around 900°C. Finally it decreases as temperature increases to 1000°C. The specific heat starts at around 0.5 J/(g·K) and reaches values of around 1.3 J/(g·K) at the highest temperatures.

During the cooling phase, between 1000° and 970° some reactions are occurring but, as well as in the beginning of the warming phase, these early reactions can be ignored since they are related to the method: this is an artifact, it is systematic of the testing methodology and is related to thermal equilibrium of the system (sample holder and gas argon). Then, the only reaction during the cooling phase is shown by the peak at 573°C, which likely corresponds to the alpha / beta quartz transition. Finally, the specific heat decreases slowly until it stops around 0.83 J/(g·K).

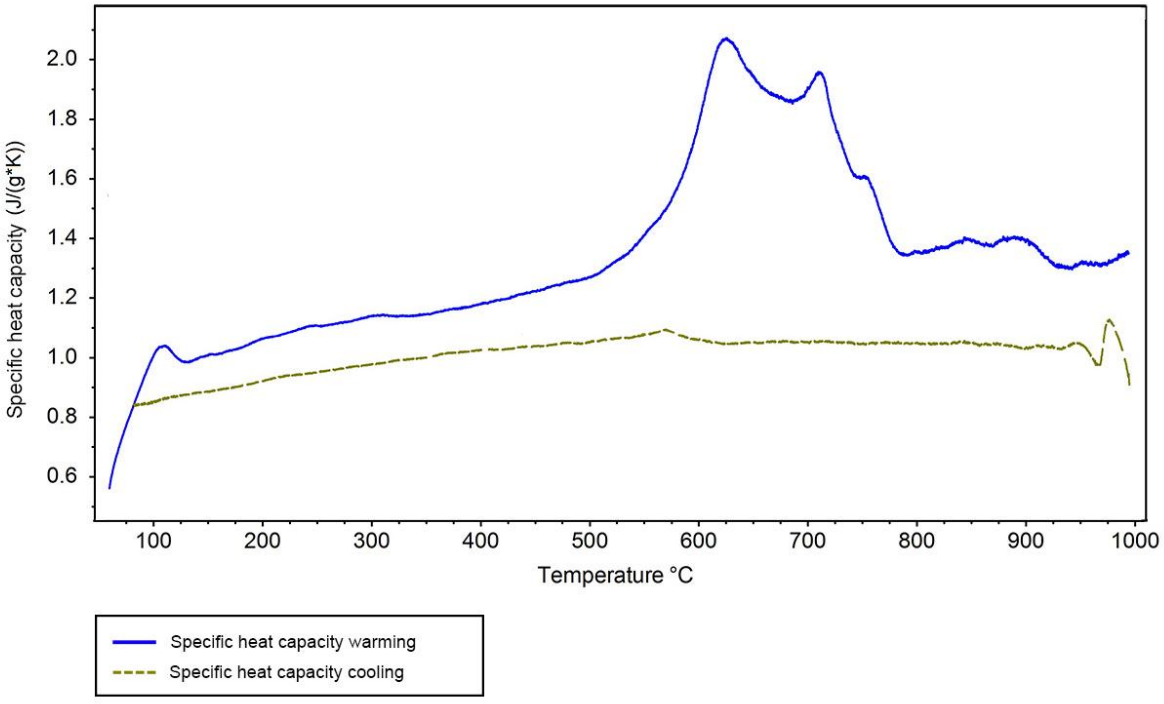

Figure 3.25: Specific heat capacity for warming and cooling phases. In the warming phase endothermic reactions occurred (high peaks between 600°C and 720°C). For the cooling phase a reaction at 573°C can be seen.

The differential scanning calorimetry (DSC) is plotted against the temperature (Fig. 3.26). It shows how (always after an initial endothermic systematic peak due to the methodology, visible around 110°C) the relevant reaction occurs around 550°C and finishes around 755°C. The highest peak reaches 0.24 μV/mg and the reaction ends at 1000°C with ~0.088 μV/mg (where: 1 μV is equal to $1 \cdot 10^{-6}$ J/C).

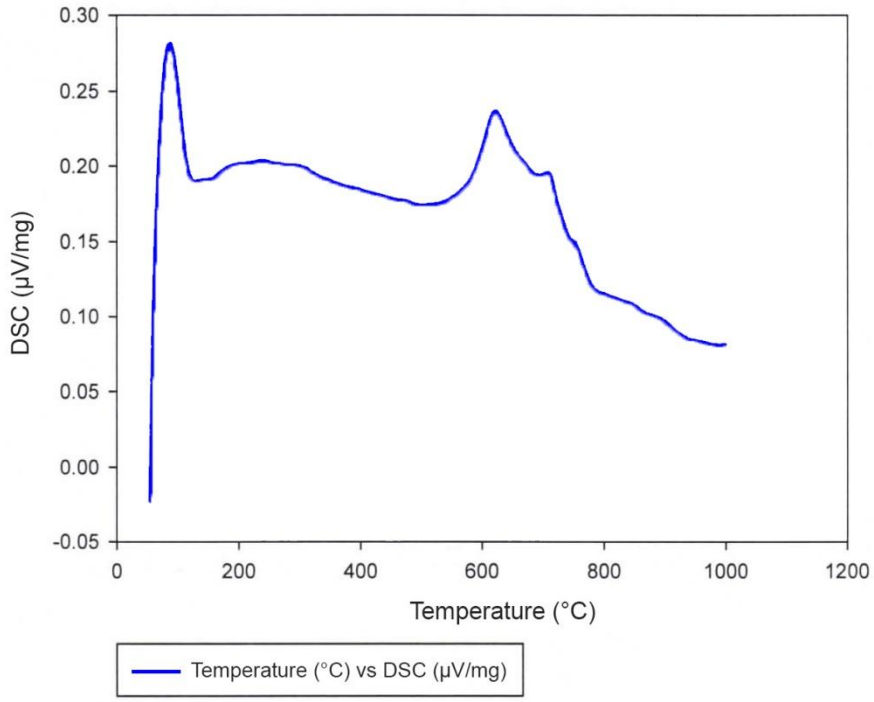

Figure 3.26: Differential scanning calorimetry (DSC). The highest value is a machine effect starting the test, the biggest endothermic reaction occurs between 550°C and 700°C. 1 μV is equal to $1 \cdot 10^{-6}$ Joule/Coulomb.

3.2. DISCUSSION

This section is divided into several sub-sections. The first one addresses the petrology, in particular the analysis and discussion of the thin sections. The second section is related to the understanding of the strength of the rock and its behavior in terms of stress and strain. The data obtained from uniaxial, triaxial and Brazilian tests will be shown, discussed and compared with previous data from other work. In the third

section the permeability and porosity are considered. In the fourth section the seismic data are shown and described for both uniaxial and triaxial tests. Finally, the fifth section is dedicated to the thermal deformation, the results from thermo-analysis will be shown and they will be discussed. Comparisons of the results are made with the purpose of understanding the similarities or differences between previously acquired data and the new data generated here. The interpretation of the laboratory results is important in order to have a better idea about the greywacke basement, in terms of physical properties. Final considerations of the data shown through the whole chapter are placed as last section.

3.2.1. UNIAXIAL COMPRESSIVE STRENGTH INTERPRETATION

The widespread damage of the rock by dilational microcracks strongly influences the strength of the rock and its macroscopic elastic properties (Walsh, 1965; Brace, 1965; Heap and Faulkner, 2008). Several researchers have examined the stress–strain relationship and evolution of brittle rocks under a compressional force. The failure process can be divided into a series of phases (Fig. 3.27) identified by variations in the axial and circumferential strain response observed during the uniaxial compression tests (Bieniawski, 1967; Martin and Chandler, 1994; Eberhardt et al., 1999; Jaeger et al., 2007). These stages consist of: OA, a region in which the stress–strain response is concave upwards; AB, a region where the stress–strain behavior is almost perfectly linear; BC, a region in which the stress–strain response is concave downwards; and after C, post-failure / post-peak behavior, which is also influenced by the stiffness of the testing machine.

The elastic properties of materials are commonly acquired from the region AB of the curve, where the linear elastic constants can be determined. However, the relationship does not always need to be linear. A reproducible association between stress and strain, for instance, indicates a perfectly elastic material (where "perfect elasticity" means that during the operations of loading and unloading the same path is followed)

(Heap and Faulkner, 2008). However, the curve of the axial strain in Fig. 3.9 has similar behaviour to the following graph (Fig. 3.27):

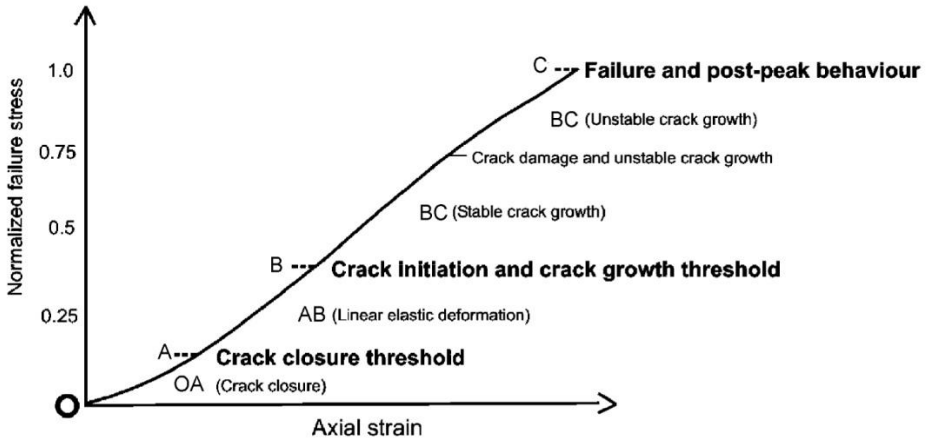

Figure 3.27: Diagram showing the shape of the stress-strain curve in a typical uniaxial experiment. The approximate positions of the stages of crack evolution in brittle rock under uniaxial compression are also illustrated (from Heap and Faulkner, 2008).

The OA region corresponds to the region in which the closure of the cracks occurs. Successively, the AB linear region describes where linear elastic deformation takes place. After that there is BC, which is the region where the cracks reopen and grow as stable cracks, until they become unstable (Griffith, 1920) with the increase of the damage. Finally, C is where crack coalescence occurs, which leads to the failure of the core.

For the dynamic elastic properties the AB region has been considered. Commonly, static and dynamic elastic properties are linked by the following equation (Landau and Lifshitz, 1986):

(Equation 3.4)

$$E_S = E_T + \frac{E_T^2 \, \beta^2 \, \mathrm{T}}{9 \, C_p}$$

where:

$\boldsymbol{E_S}$ = dynamic Young modulus

$\boldsymbol{E_T}$ = static Young modulus

$\beta = \left(\frac{\boldsymbol{d \ln V}}{\boldsymbol{dT}}\right)_p$

C = heat capacity

V = volume

T = temperature

p = pressure

Equation 3.4 is a theoretical relationship for linear elastic material, where for the ultrasonic measurements the process is isothermal while for the static measurements is adiabatic (Landau and Lifshitz, 1986). Clearly, in presence of cracks and pores Equation 3.4 would be more complicated.

An understanding of the difference between static and dynamic elastic properties is important, and several studies have tried to identify a relationship between them (Vanheerden, 1987; Wang, 2000; Mockovčiaková and Pandula, 2003). However, determining an universal relationship has proved elusive, it is not just about adiabatic and isothermal processes, in fact several reasons being suggested for the differences between the two methods of measurement. These include the magnitude of the strain amplitude applied, the rate of the application of the stress (leading to adiabatic loading for static measurements and isothermal loading for dynamic measurements), the presence of microfractures , the frequency at which the moduli is determined, whether the sample is dry or saturated, and the type of pore fluid (Hammond et al., 1979; Jizba, 1991; Adam and Batzle, 2008; Müller et al., 2010). Further reasons can be that rocks are often inelastic, affected, for example, by frictional sliding across microcracks and grain boundaries. More inner deformation can occur during a large-strain experiment than over very small-strain cycles. The strain magnitude relevant to geomechanical processes, such as hydrofracturing, is of the order of 10^2, while the strain magnitude due to elastic wave propagation is of the order of 10^7 or less. This large strain difference affects the difference between the static and dynamic moduli. Another factor is

considered by Blake and Faulkner (2016), they demonstrate that the influence of stress-induced anisotropy, produced by the application of an elastic axial load, is the effect of which will be sampled differently by static loading and elastic waves and it may lead to differences if isotropy is assumed. In this work, since the seismic wave have been utilized on the cores only for the axial direction, it has been assumed that these greywacke samples are isotropic and, indeed, there are several differences between the dynamic and static elastic properties, as shown in Table 3.10. Therefore, it is not surpirising that the dynamic and static elastic properties measured in this work show differences between each other (Table 3.10). The Poisson's ratio and Young's modulus results are higher for dynamic than the static measurements, except for the Poisson's ratio of TTGW_11_3_13, which is higher for the static measurement.

Static Elastic Properties			Dynamic Elastic Properties	
Poisson Ratio	Young's Modulus (GPa)	Sample	Poisson Ratio	Young's Modulus (GPa)
0.22	74	TTGW_11_3_11	0.29	82
0.23	68	TTGW_11_3_12	0.30	84
0.30	78	TTGW_11_3_13	0.28	80

Table 3.10: Comparison between the static and dynamic elastic properties. In general the Poisson ratio and Young's modulus results are higher for dynamic than the static measurements, except for the Poisson's ratio of TTGW_11_3_13, which is higher for the static measurement.

However, when the graph of Figure 3.9 is compared with a typical stress-strain curve, it can be seen that the subdivision of these curves into some of the regions as previously described is possible. Basically, the difference occurs as the sample approaches failure. At low stress, the stress-strain response is concave upward for the first 30 MPa of stress (crack closure), then it becomes quite linear until the failure. This trend means that the compaction and linear elasticity is dominating.

As can be observed in Figure 3.28 a characteristic region is where cracks grow. Region BC is undoubtedly curved and concave downward, in contrast to the region from O to B, which are almost straight. This indicates that, for the greywacke samples, before

failure there is negligible dilatancy, and consequently it means that there is no significant development of cracks before failure. This is clearer if Westerly granite radial and volumetric strain are compared with the greywacke one. For the greywacke samples all the curves in the graphs show linearity up to failure, whereas for the granite the radial and volumetric strain gradient with respect to the stress change drastically in the BC (unstable crack growth) zone. Both strains evolve as curves with a downward concavity and in the same direction. It means that, looking at the volumetric strain overall, the radial deformation becomes dominant.

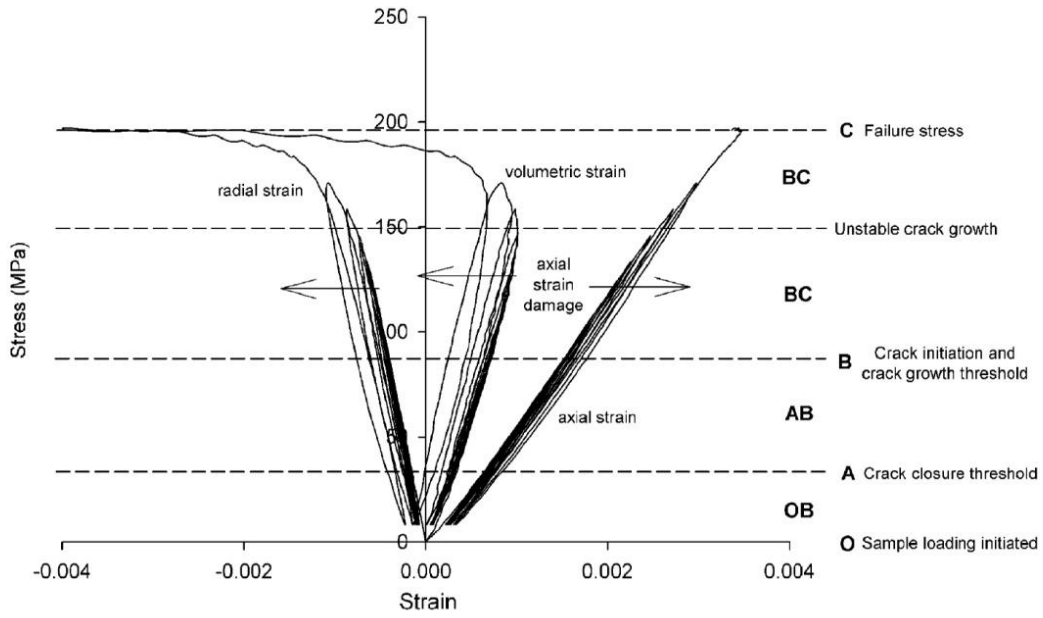

Figure 3.28: Representative stress-strain curves for Westerly granite under increasing-amplitude cyclic loading. The stress-strain steps are in refer to Fig. 3.27. The arrows indicate how the strain cures change during the accumulation of microcrack damage during the experiment (Heap and Faulkner, 2008).

From all this, it can be interpreted that in these greywackes there is little crack growth before failure, almost avoiding the stage identified as BC and without showing a yield point. Instead, for the graph in Figure 3.28 it is clear that the region BC is crack-growth dominated.

The tests performed in this project on samples from the Waipapa basement have shown that these rocks are mechanically very strong, as illustrated in Table 3.4. If these rocks are compared to values calculated for other crystalline lithologies, for example

Westerly Granite (which shows an UCS ≈ 200 MPa (Heap and Faulkner, 2008) and a tensile strength around 10 MPa (Homand - Etienne and Houpert, 1989), as well as basalt or andesite, which claim an UCS ≈ 50 - 150 MPa and tensile strength included in a range between 10 and 25 MPa (Dinçar et al., 2004; Siratovich et al., 2012)), it is evident how similar or stronger the Waipapa greywacke is (Table 3.5).

Also comparing the unconfined strength data between Waipapa and Torlesse terranes (which have a finer grain size), as illustrated by McNamara et al. (2014), the Waipapa is systematically stronger than the Torlasse greywacke. This is also further evidenced by the elastic properties (less compressible and stiffer) as shown in Table 3.5 and Table 3.6.

Moreover, from the UCS experiments conducted in this project, having tested the Waipapa terrane on rocks from the same quarry but with a different density of fracturing (determined by hand specimen-scale observations of the rocks/samples), it has been observed that the strongest series (TTGW_11_3 series) is the less fractured. This can be established because the highest value of the weakest series (TTGW_11_2) is lower than the lowest value of the strongest series (Table 3.4). Since the more the core is fractured (sealed fractures) and the sooner the failure occurs, these data show that as the cracks density increases, the UCS of the rock decreases. The crack density can be calculated and there are many ways to do it (Budiansky & O'Connell 1976; Jaeger et al. 2009; Mavko et al. 2009). For example Budiansky & O'Connell (1976) give the crack density Γ as a function of the Poisson's ratio of the uncracked material v and the cracked material v_c for penny shaped cracks to be:

(Equation 3.5)

$$\Gamma = \frac{45}{16}\frac{(v-v_c)(2-v_c)}{(1-v_c^2)[10v-v_c(1+3v)]}$$

Using the Equation 3.5, the Waipapa Greywacke crack density has been calculated from the only sample TTGW_11_3_12 and it results approximately equal to

0.06. However, also several experimental studies have verified that the elastic properties depend on the extent of fracture damage inside the rock (Eberhardt et al., 1999; Lau and Chandler, 2004).

Siratovich et al., (2014) performed uniaxial compressive tests on Rotokawa andesite (Fig. 3.29). In Figure 3.29 is possible to see how the curves assume a linear trend, overall for the axial strain, and only before the failure there is a small variation, which probably reflects the opening of the cracks. This is better described by the volumetric strain.

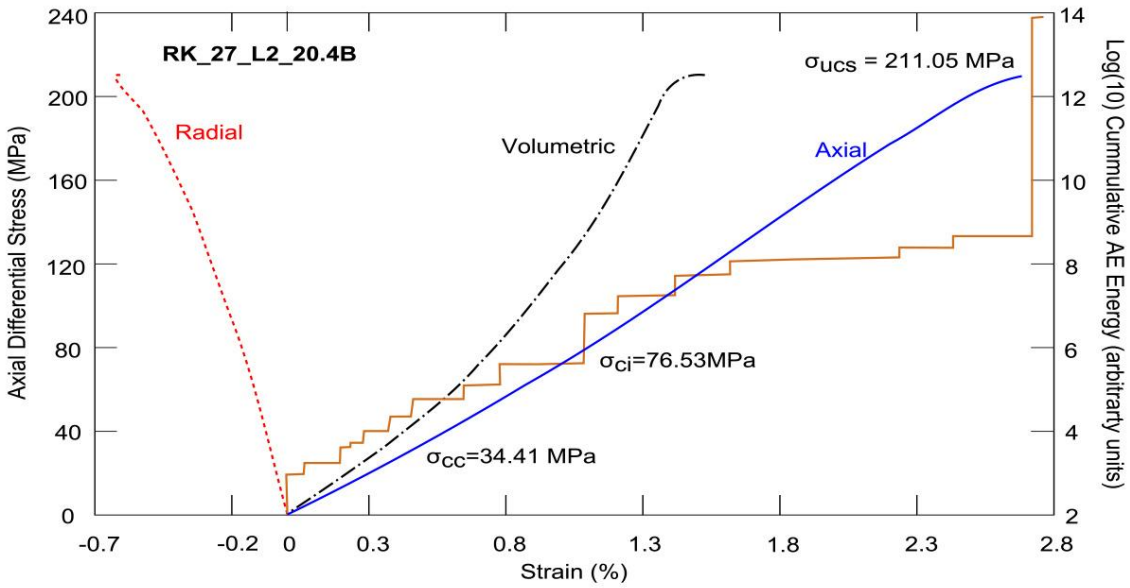

Figure 3.29: Stress-strain curves for Rotokawa andesite. On the right side it is also shown the cumulative AE Energy (Siratovich et al., 2014).

Siratovich et al., (2014) showed how for Rotokawa andesite the samples with low UCS usually develop a single fracture plane, samples with medium UCS develop several fracture planes and samples with very high UCS (as in the case of Waipapa greywacke) showed explosive and catastrophic failure into some large and small pieces of rock with no distinct failure plane (Fig. 3.29), as here observed for the greywackes during the uniaxial tests. Siratovich et al., (2014) show for this last kind of failure a stress-strain curve (Fig. 3.29) with UCS equal to 211 MPa, similar to the TTGW_11_2

samples (Table 3.4). All the greywacke samples tested in this work had similar or stronger failure. Moreover, the Rotokawa andesite trends of the stress-strain curves are comparable to the Waipapa greywacke trends (Fig. 3.9 and Figures from A1 to A10). In fact, they both show a very similar behaviour, only before the failure there is some small difference. From all this could be also inferred that the large stress drop during the failure creates macrofractures, in laboratory experiments as well as in the field.

3.2.2. TRIAXIAL TEST INTERPRETATION

Mitchell and Faulkner (2008) tested Westerly granite in comparison with the Cerro Cristales Granodiorite. They performed triaxial tests at variable effective pressures of 10, 15 and 20 MPa, with the peak stresses reaching 278, 330 and 356 MPa respectively (Fig. 3.30). The stress-strain behaviour for all the effective pressures begins with an upward concavity for the first 40 MPa of stress, then it evolves as linear elastic up to the yield point and finally it ends with a concave down until the sample failure.

Comparing the triaxial test results with Mitchell and Faulkner's (2008) triaxial tests it is evident how different the evolution of the curve is. After a similar evolution in the beginning (crack closure) and in the central portion (linear elastic behavior) the curves differ. In Mitchell and Faulkner (2008) there are yield points for each curve and consequently a portion of the curve with downward concavity (Fig. 3.30), which is missing in the triaxial tests of the greywacke (in the "before failure phase", Fig. 3.10). It indicates a relevant difference in plasticity between the granite and the Waipapa greywacke. In fact, while the granite has a plastic behavior after the yield point, the greywacke reaches directly the brittle fracture showing a direct passage from elasticity to failure. In this case we can assume that the yield point coincides with the failure point.

It is important say why the greywacke behaves in a brittle fashion. Probably the answer lies in the porosity and in the size of the flaws in the material. There will be a critical flaw size above which the material will behave in a brittle fashion.

For brittle failure in tension:

(Equation 3.6) $$\sigma_{fail} = \frac{K_{IC}}{\sqrt{\pi a}}$$

where:

K_{IC} = fracture toughness (or critical stress intensity factor) (MPa $\cdot\ m^{\frac{1}{2}}$)

(Equation 3.7) $$K_{IC} = P_{min} \cdot x$$ (Guo et al. 1993)

with:

P_{min}= local minimum of the loading (obtained from the load-deformation curve)

x = a number which is the result of geometrical parameters and a constant

And for plastic failure:

(Equation 3.8) $$\sigma_{fail} = \sigma_y$$

Therefore, setting the equations 3.6 and 3.8 equal to each other:

(Equation 3.9) $$a_c = \frac{K_{IC}^2}{\pi \sigma_y^2}$$

where:

a = fracture length (mm)

a_c= critical fracture length (mm)

Thus, above the critical value of flaw size (a_c) the material will behave in a brittle way and below it will deform plastically. This can give an explanation why the greywacke is so brittle compared to granite. With higher porosity rocks there is a shear

enhanced compaction that results in work hardening. However, from permeability measurements can be deduced the growth of new cracks (supposedly growth of "wing cracks" (McClintock and Walsh, 1962)) before the failure. The mineralogy between Cerro Cristales granodiorite, Westerly granite and Waipapa greywacke is similar, but most probably what makes the difference in the trend evolution can be related to a number of causes (e.g. initial crack density, cementation resulting from circulation of hydrothermal fluids, how the rocks were exhumed, induration via low grade metamorphism of the greywacke matrix) that influence the greywacke mechanical properties. Moreover, another factor is the grain size. The grain size not only controls the length of microcracks (Mitchell and Faulkner, 2008) but (as has been petrographically observed in this work (Section 3.1) that it controls also the pathways and directions of the microcracks, which could contribute to a control on rock strength.

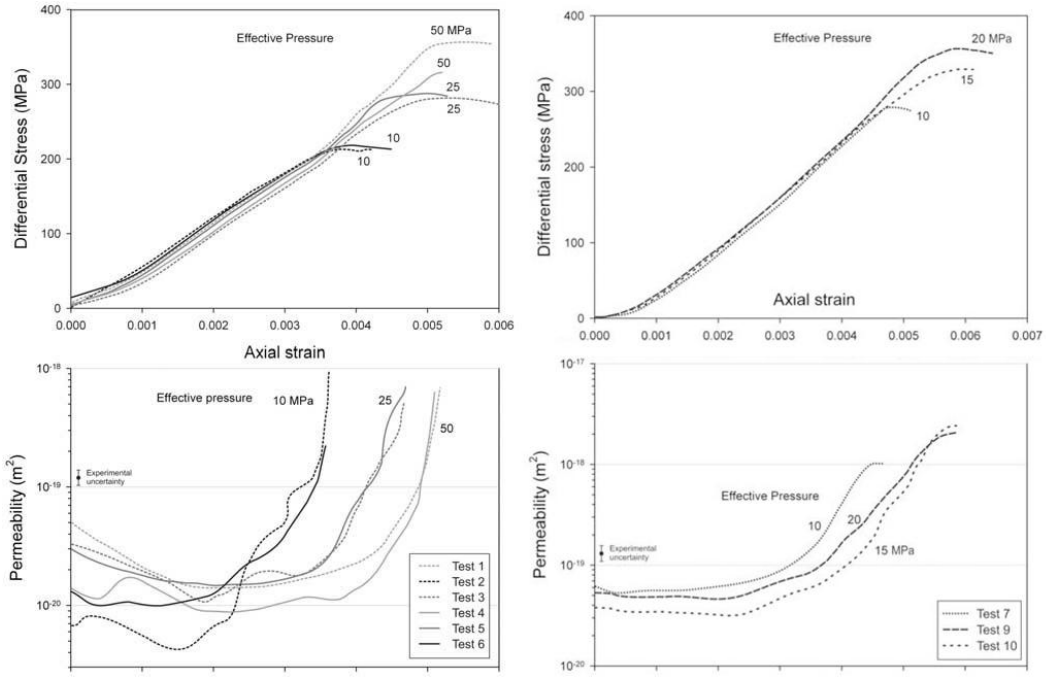

Figure 3.30: Experimental data for Cerro Cristales Granodiorite (left) and Westerly Granite (right) performed by Mitchell and Faulkner (2008). The differential stress and permeability are plotted versus axial strain. The effective pressures are indicated, and pore fluid pressure was maintained constant at 50 MPa.

Comparing the volume evolution to Mitchell and Faulkner (2008) it is evident that there is a similar compaction trend to the beginning of the experiments and towards the end the curves increase rapidly assuming positive values (Fig. 3.31).

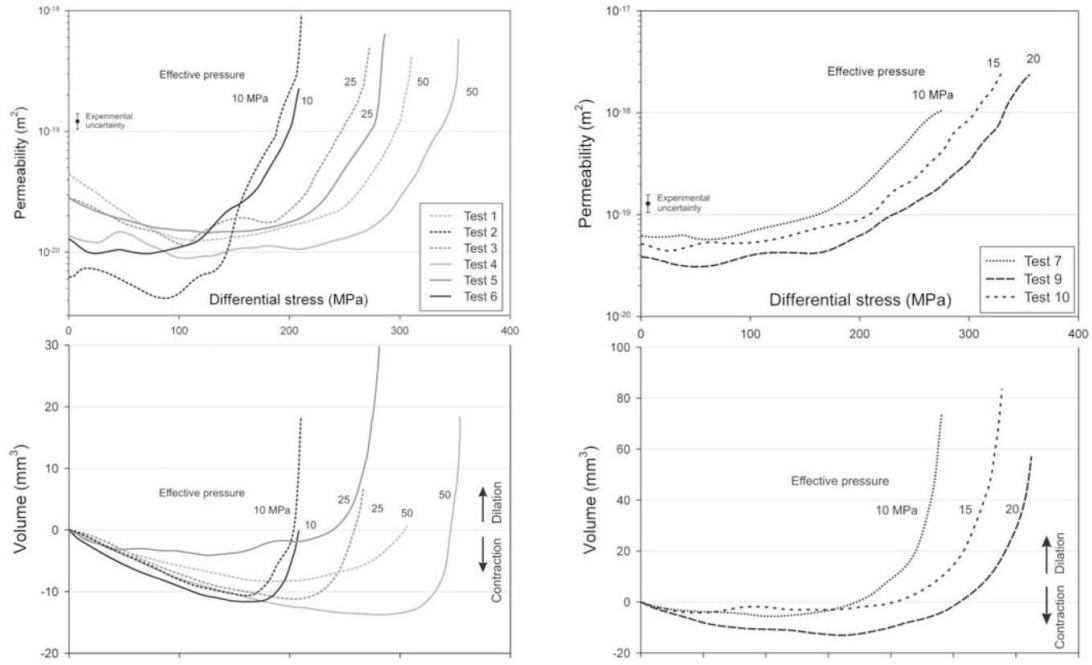

Figure 3.31: Permeability and sample volume change as functions of differential stress for Cerro Cristales granodiorite (left side) and Westerly granite (right side). Water pore pressure is maintained at 50 MPa (from Mitchell and Faulkner, 2008).

For granodiorite, the compacted pore volume shows values between around -3 mm^3 and -13 mm^3 before it increases. The final peaks of the volume show values between 0 mm^3 and 30 mm^3. For granite the volume shows values between around -2 mm^3 and -16 mm^3 before increasing abruptly. The final peaks of the volume have values between ~57 mm^3 and ~84 mm^3, definitely higher than Cerro Cristales granodiorite and the Waipapa greywacke (Fig. 3.31).

To sum up, all the three rocks Cerro Cristales granodiorite, Westerly granite and Waipapa greywacke show a compaction in the beginning. Before failure the crystalline rocks (Cerro Cristales granodiorite and Westerly granite) are subjected to an increase of pore volume, which likely indicates the presence of new fractures. The greywacke does not show this trend, as before explained, therefore probably in the greywacke there is

not a relevant presence of cracks before the failure. This can be confirmed also from uniaxial data and stress-strain curve from triaxial data (Fig. 3.10).

3.2.3. PERMEABILITY MEASUREMENT INTERPRETATION

For Westerly granite, the pore volume-stress curves illustrate how the volume at the start of loading decreases, and thus also the porosity decreases, up to an inflection point that corresponds with the onset of steepening gradient of the permeability curve. This is in contrast with the results of the Cerro granodiorite which showed that the permeability began to increase slightly before that the volume began to increase (Fig. 3.31). However, as it can be observed in the results of Mitchell and Faulkner (2008), sometimes the inflection point of the volume-stress curves, where the porosity stops decreasing and begins to increase, does not coincide with the inflection point of the permeability-stress graph, suggesting that the permeability is increasing distinctly at a considerably lower strain. This is an important factor and since compaction and dilatancy are not reciprocally exclusive processes. The microfractures having orientations at high angles in relation to σ_1 continue to close while new dilatant cracks grow subparallel to σ_1 Mitchell and Faulkner (2008). The axial orientation of the new born dilatant cracks contributes more to the permeability with an axial pathway than the compacting of radial cracks. Thus, the increase in permeability precedes the increase in overall crack volume.

The permeability results show some similarities between Westerly granite, Cerro granodiorite and Waipapa greywacke. With increased differential stress and strain, there seems to be an initial transient decrease in permeability. The initial decrease is associated to the nonlinear increasing stiffness part of the stress-strain curve, most probably due to the closure of microcracks orientated obliquely and transversely to the applied force. The crack closure causes a decrease in porosity and related decrease in permeability (Mitchell and Faulkner, 2008). Westerly granite does not reveal significant decrease in permeability in the crack closure phase, which suggests that the crack network is not hydraulically well-connected (Mitchell and Faulkner, 2008).

The permeability data are mostly coherent to the strain data to the uniaxial and triaxial loading and the variation of volume. The same for the seismic waves, as it is shown in Section 3.1. The only contrast is due to the last *k* measurement before the failure, indeed this value ($1.10 \cdot 10^{-17}$ m^2) looks higher than it was expected. A possible explanation for this behaviour could be that the permeability measurement was performed while the core was going to fail. In fact, with the stress stable at 314 MPa (which means a high quantity of stress acting on the core) the cracks tend to be opened, and this allows more fluid flowing through the cracks. Instead, if we want to compare this value with the next measurement (the white spot at 0.95 mm of displacement, after the failure, in Fig. 3.14), we can see that also if the core is already failed, at 120 MPa the permeability results to be between 10^{-19} m^2 and 10^{-20} m^2, higher by around one and half order of magnitude than the previous measurements made of the intact rock.

McNamara et al., (2014) performed a fluid flow test through a sample of Torlesse greywacke at confining pressure of 20 MPa. They recorded a very low permeability value: $\sim 4.824 \cdot 10^{-22}$ m^2. This value is comparable with the measurements performed in this work on Waipapa greywackes and, consequently, with the very low porosity measured. If we compare this value from Torlesse greywacke and the Waipapa values with the Rotokawa Andesite tested by Siratovich et al., (2014) (Fig. 3.32), which shows an order of permeability of 10^{-17} m^2, it is clear that the greywackes are highly impermeable with a difference of around 4 - 5 orders of magnitude compared to the Rotokawa andesites.

A key relationship typically occurs between permeability and porosity. The dependence of the permeability on porosity is normally explained by the assumption that a more connected pore space (pores and cracks) offers more capable pathways for fluid migration (Costa, 2006; Chaki et al., 2008), and this underlines the importance of the microstructures. In relation to the microstructures, Siratovich et al., (2014) have shown that the porosity is related to the crack surface area, consequently the increasing of the crack density corresponds to a sample with a higher permeability, but at the same time they demonstrated that it is possible to have mesofractures that increase the permeability without modifying significantly the porosity. The samples tested by Siratovich et al., (2014) have shown higher average permeability in relation to their porosity, which leads

to the conclusions of Stimac et al., (2008), namely that mesofractures and macrofractures are fundamental in controlling the permeability of geothermal reservoirs. Definitely the macrofractures are essential for the fluid production from the geothermal reservoirs but, on the other hand, the microstructures of the host rock have to be considered in relation to the fluid flow, storage capacity and total permeability of the reservoir (Jafari and Babadagli, 2011).

In this work permeability and porosity are related, both have consistently very low values (Table 3.9), but are not strongly related as is suggested by Stimac et al., (2008) for other geothermal studies. This can be deduced from the permeability measurements after the failure where, with the addition of macrofractures through the specimen, the permeability remains low (10^{-19} m^2 - 10^{-20} m^2) (Fig. 3.14). This likely indicates a poorly connected pore/micro-crack network inside the greywacke sample.

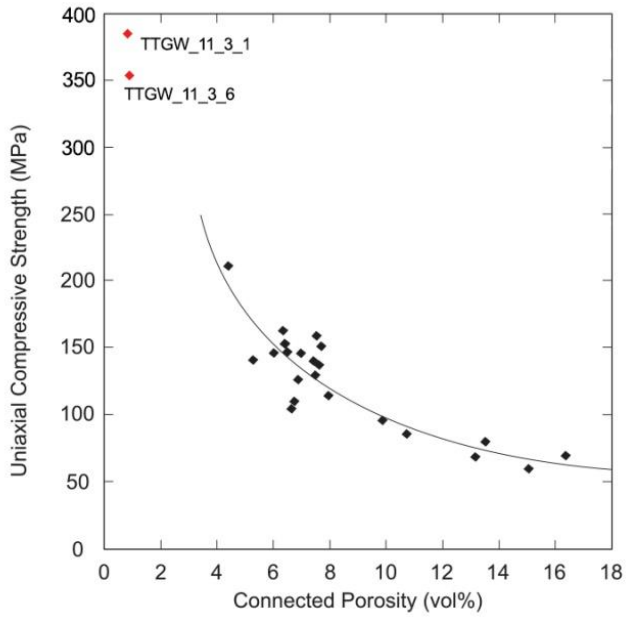

Figure 3.32: UCS vs porosity for Rotakawa andesite, from Siratovich et al., (2014). The graph has been modified inserting two UCS vs porosity values from Waipapa greywacke (in red). Note the higher values for the UCS of greywacke samples than the andesite samples.

3.2.4. HYDRAULIC CONDUCTIVITY OF A SINGLE FRACTURE

With a natural permeability of ~10^{-21} m^2 for the intact rock (Fig. 3.13), the Waipapa greywacke is a very impermeable lithology. This is confirmed also by the very low porosity, ~1% for these greywacke samples (Section 3.1). To modify the permeability of the intact rock the differential stress has to be increased. When the force is applied in the beginning there is a further decrease of the permeability, but when the stress reaches the level to create a network of microfractures before that the failure occurs, the permeability increases steeply (Fig. 3.13) showing a variation of up to six orders of magnitude (from 10^{-23} m^2 up to 10^{-17} m^2).

It is not known exactly the stress level in the geothermal reservoir, due to a lack of *in situ* stress measurements, but it is known that with increasing compressive stress the fractures can be closed. Therefore, in order to maintain an enough permeability level for the exploitation of the reservoirs typically cold water (~25°C) is injected in the wells with the purpose to change the field stress and to induce fracture of the rock.

Another way to modify the permeability is to generate a macrofracture. Obviously, in the macrofracture the fluid flow will be faster and more abundant than to go through a microcrack network, and it is an important detail that makes the macrofracture as a fundamental target to achieve for the control of the permeability in the greywackes.

To study this behaviour, a single macrofracture along the vertical axis of a cylindrical sample was created (Section 2.1 and 2.3) and measurements of the permeability at different increasing levels of confining pressure have been performed, following the method utilized by Nara et al., (2011).

It is important to understand when the closure of the macrocrack happens and under which conditions. Nara et al., (2011) experimented with the method of the fluid flowing through a single fracture on basalt rocks. Their results (determined by the pressure sensitivity of the micro/macrofracture networks) show that the closure of the fracture occurs at 40 MPa.

A similar behavior has been observed in the two experiments performed in this project. For TTGW_11_3_5, a relevant change of the trend can be noted at 95 MPa, which is the moment when the fracture is closed. Also in these tests the fluid continues to flow after the shutting of the fracture. In fact the permeability is stable around 10^{-19} m^2 between 95 and 150 MPa. This value of permeability is 2 orders of magnitude higher than the natural value identified in the previous experiments, which was located around 10^{-21} m^2 (Fig. 3.13). For TTGW_11_3_17, it is hard to identify a closure point; it most likely occurs at 112 MPa, but following measurements at higher pressure do not show stability in permeability (Fig. A18). In general, for this sample the permeability is a bit lower than TTGW_11_3_5.

Analyzing the situation, it could be supposed that the reason for why the fractures are not totally closed is the presence of grain fragments inside the fractures. Such grains are observed from petrographic studies of natural and induced shear fractures (Fig. 3.5 and Fig. 3.6). The presence of these grains within the fracture plane would prop open the fracture, preventing it from completely closing. These "propping" grains are widespread along all the shear fracture planes, with several zones with higher proportions of them. In the macrofracture (a mode I fracture) prepared with the Brazilian jig (Fig. 3.8) there are no grains like this that could serve to prop open the fracture under increasing confining pressures. Consequently, it has to be deduced that the grains are not the reason why permeability within these fractures is high at high confining pressures.

In relation to the presence of grains, Nara et al., (2011) affirm that due to their low aspect-ratio, the macrofractures are easier to close as the effective pressure is increased, so that their total influence on the permeability decreases at higher pressures. On the contrary, while a distributed network of microfractures exerts a smaller influence on the total permeability at low pressures, their influence is high on the permeability when the sample is held at higher effective pressures, because their low aspect-ratio makes them harder to close. However, in nature the rocks contain fractures at different scales (for example both microfractures and macrofractures).

Therefore, for a material containing both microfractures and macrofractures, the closure of macrofractures dominates the permeability reduction at relatively low pressure, the closure of microfractures is influenced by the higher pressures. Looking at

Nara et al., (2011)'s experiments and the experiments of this project, what can be deduced is that to close the fractures completely, ~40 MPa is not enough for the basalt and ~95 MPa is not enough for the greywacke (Fig. 3.7), in order to maintain a permeability for confining pressures greater than 100 MPa.

Considering the fact that there is no presence of grains in the macrofracture obtained by the Brazilian jig, other causes for the lack of closure of the fracture plane must be considered. In the opinion of Guéguen and Palciauskas (1994) there are two ways so that a significant permeability can be preserved at elevated pressures: the first one is to have an interconnected porosity consisting of isotropic pores; the second one is that the fractures have to present offsets, so that the fracture surfaces are not perfectly matched and accordingly there are gaps. This last option, whereby the macrofractures created with the Brazilian jig could not be sealed due to variation in the two fracture wall morphologies, is considered the most likely explanation for the data collected in this work. Moreover, Gangi (1978) affirms that even smoothly-ground surfaces do not have perfect fits. When the fractures cannot be totally closed (for any reason) as shown in this experiment and in Nara's et al., (2011) experiment, it seems that there are only two ways to close them: one is increase the stress field, the other is related to the precipitation of hydrothermal minerals situated in the fluid flowing through the cracks. However, Bernabe (1987) affirms that with pressure cycling this kind of fracture can be closed, but in this work pressure cycles were not employed.

The temperature influences the permeability through two separate processes: thermally inducing microfractures first, and second the dissolution/precipitation reactions. Dissolution/precipitation processes are controlled by temperature, pressure, and deviatoric stress gradients. At the large scale, the effects of temperature and pressure can promote fluid circulation and for the transfer of material from places with elevated solubility to places having reduced solubility. At small scale, the processes of dissolution/precipitation are governed by "stress concentrations" at grain contacts and contribute to the progressive compaction of the rock and to the cementation.

3.2.5. THERMAL FRACTURING INTERPRETATION

As previously noted, thermally generated microfractures result from the differential dilation of anisotropic crystals. It is due to two causes: the strong temperature gradient or differences in the mineral thermal expansion coefficient. The resulting permeability increase will be a function of the density and geometry of the induced microcracks (Guéguen and Palciauskas, 1994).

In physics it is known that the increase of the temperature produces the thermal expansion of the minerals, which generates an internal stress since the minerals increasing the dimensions as they push on each other. Consequently, the stress exceeds the tensile strength and cracks occur.

In the low temperature range of testing (50-550°C) there is no significant change in the sample mass or calorimetric deviation. An endothermic artifact (between 50 and 120°C in Fig. 3.25 and Fig. 3.26) is present in the DSC reaction. From this, it is possible infer that no significant reactions went on below 550°C.

However, the beginning of a considerable thermally driven reaction occurs near 580°C confirmed by the commencement of mass loss (Fig. 3.24) and also the endothermic peak (Fig. 3.26). This reaction causes a change of the sample length, which is associated with the rapid increase in the measured thermal expansion coefficient (Fig. 3.23). The estimated thermal expansion coefficient has appreciably increased from ~$1.2 \cdot 10^{-5}$/°C to ~$5.3 \cdot 10^{-5}$/°C (in the range 450–600°C; where 600°C is the maximum of the temperature reached for alpha). Certainly the measurement performed at 600°C in the laboratory cannot be totally applicable in nature, because in the laboratory test an axial load of 3 kN only is applied, whereas in nature the stress acts from all the directions and will be much higher.

As previously discussed, devolatilization of mineral phases and the breakdown of fluid inclusions during the heating (or cooling) are processes that have been attributed to the formation of microfractures in samples (Lin, 2002; Keshavarz et al., 2010). The greywacke shows that these processes are not happening under 550°C. This has a significant geothermal interest, because the limit for the thermal fracturing in Waipapa greywacke could be established.

3.2.6. FINAL CONSIDERATIONS

The main purpose of this project is to understand what controls the fluid flow in the greywacke geothermal reservoirs. To achieve this, information from a range of experiments on greywacke rock samples have been acquired and analysed. The permeability of the intact rock was shown to be low, with values around 10^{-21} m^2, indicating that the only way that the fluid flow could occur through the greywacke is via the development of microscopic and/or macroscopic fractures.

In nature, there are two ways to produce fractures in rocks: failure under differential stress conditions, and thermal fracturing. In this geographic area the stress conditions are controlled by the overall tectonics, which plays a dual role: to metamorphose the greywackes making them stronger, and to stress them resulting in deformation and fracturing (creation of fractures and faults) making them weaker. From the laboratory test results it is observed that to reach failure a high differential stress is required: for unconfined conditions approximately between 205 and 240 MPa for rocks with sealed fractures, and up to 300 MPa for the less fractured rocks, with a peak of 384 MPa. However, at moderate differential stress (AB segment in Fig. 3.27 and Fig. 3.28), the greywacke has very low permeability (10^{-22} and 10^{-23} m^2), because the fractures are closed and the already very low porosity is further reduced by confinement.

Thermal fracturing under geothermal conditions is one way to increase permeability. From the laboratory results it can be shown from differential scanning calorimetry that breakdown of the minerals occurs from temperatures ~550°C and higher. The thermo-mechanical analysis has been performed to a maximum temperature of 600°C, a temperature expected at ~6 km depth, which is about the target depth for future geothermal wells in the TVZ geothermal fields. At 600°C the thermal expansion coefficient is $5.4 \cdot 10^{-5}$, enough to induce thermal fracturing.

The presence of fracture networks must be sufficiently developed to allow a good circulation of heat flow through the basement. However, in the fractures observed in natural samples the width is usually between 80 and 300 μm (likely due to the growth of the minerals inside the fractures), only few exceptions past this range, such as the

observed antitaxial vein with an average width around 2.4 mm (Fig. 3.1). It has been noted that usually these cracks are filled with clay minerals or calcite, products of the precipitation from thermal fluid transport.

From the fractures generated with the Brazilian jig (Fig. 3.8) it is evident how much higher the permeability is for greywackes containing a macrofracture, ranging between 10^{-16} and 10^{-17} m^2, compared to the intact greywacke. It shows also how it is hard to close the fracture. Under a confining pressure of 150 MPa the single fracture is still not totally closed (with a permeability of 10^{-19} m^2), This is most likely because of the presence of grains or because of offsetting of the fracture and the tortuosity of the walls. For a similar study on basalt by Nara et al., (2011), at 40 MPa of confining pressure the fracture was completely closed. Therefore, an easier way for these cracks to be closed is to be filled via mineral precipitation.

As stress conditions in the reservoir change, reactivation of the sealed fractures could occur. The UCS tests show that rocks containing sealed fractures are much weaker than the intact rocks.

The walls of the boreholes were also studied with borehole televiewers (McLean and McNamara, 2010; McNamara et al., 2015) with the purpose to understand the nature of the fracture permeability. These techniques provide detailed information on the position, orientation, nature of the fracture and stress orientation inside two wells drilled into greywacke reservoirs at Kawerau Geothermal Field (Wallis et al., 2012), giving a prediction on the fracture state of the reservoir.

Another way to explore the reservoir status *in situ* or estimate the fracture state is to observe the behavior of seismic waves (Budiansky and O'Connell, 1976). The velocities of P and S waves can give an indication of the physical state of the rock (e.g. fracture density). There are different techniques to study the rocks through the wave velocities. In this work good results have been achieved studying their trends in relation to the increasing of differential stress.

Ultimately, all the studies in this project are aimed at understanding what the likely *in situ* permeability of the greywackes is, and how to produce it artificially if the natural permeability is not enough to satisfy the required flow conditions. Certainly the tectonic stress produces fracturing, as well as the thermal stress due to slow changes of

the temperature related to variations in the geothermal gradient, but a high permeability can be produced artificially by a large scale injection of cold water with the purpose of producing a significant thermal stress and the breakdown of rocks.

CONCLUSION

This study provides an evaluation of the physical and mechanical properties of the Waipapa greywacke. Through a multi-disciplinary approach, the Waipapa greywacke has been characterized from the microstructural to macroscopic scale via the determination of physical rock property datasets that provide insight into geothermal development of this reservoir type rock in New Zealand. A global understanding of how the relations of microstructural texture influence key physical properties such as strength and permeability have been investigated.

The conclusions of this project can be summarized as follows:

1) Uniaxial, triaxial and Brazilian tests have shown that the Waipapa greywacke rock, that is part of the greywacke basement terranes of geothermal systems in New Zealand, is mechanically very strong.

2) The natural greywacke samples that possess lower fracture density are stronger than the samples with higher fracture density.

3) The distribution of the fractures across the experimentally produced shear fractures is not uniform: one side is heavily damaged and the other one less.

4) Physically, the more indurated and compact a material is, the faster seismic waves can travel through it. Thus seismic wave velocity can be used as a proxy for fracture density. Observations of high seismic wave velocities (both Vp and Vs) in the Waipapa greywacke corroborate a high density and the low presence of cracks and microcracks.

5) Seismic wave velocities measured under confining pressure show slightly higher values than when it is measured without confining pressure. This small difference may be due to the closure of rare, yet present, micro-cracks in the greywacke under confining pressures.

6) Waipapa greywacke terrane has very low permeability (k_{nat} = ~10^{-21} m^2) and porosity (ϕ = 1.035%), confirming the dominant role of fractures in the control of fluid flow.

7) Permeability is noted to decrease with increasing effective pressure. During triaxial loading the permeability remains very low indicating that a lack of the development of any fracture network. There is a permeability increase, but only immediately before failure. This may be related to the quick growth of new fractures.

8) For greywacke samples with induced single fractures, the permeability decreased when confining pressure was increased. However, even at high confining pressures, these structures were still capable of providing fluid flow.

9) The thermo-analysis shows that the first important endothermic reaction in greywacke basement rocks occurs around 550°C. Up to 550°C thermal fracturing occurs. Between 550°C and 700°C, according to the endothermic reactions, a change of phase occurs. From 700°C onwards the melting phase takes place. The thermal expansion coefficient has been estimated: $\alpha_L = 11.617 \cdot 10^{-6} \cdot C^{\circ -1}$.

APPENDICES

APPENDIX A: GRAPHICAL INTERFACES

UNIAXIAL TEST - GRAPHS:

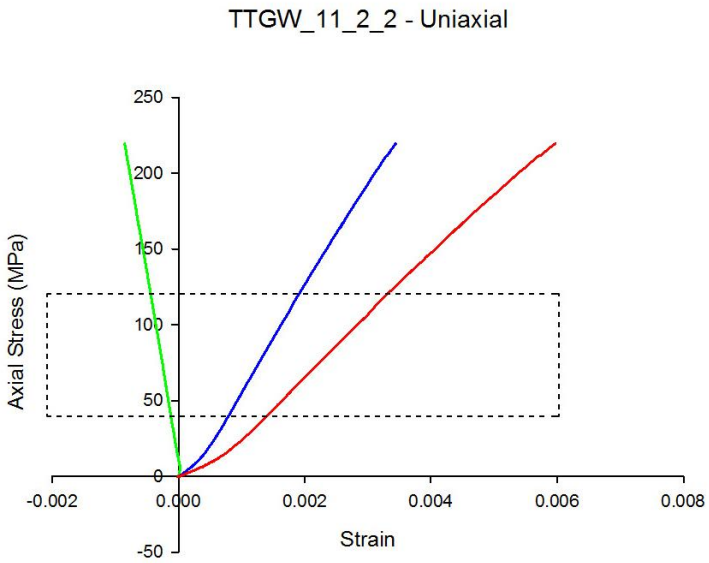

A 1: This graphs refers to Figure 3.9. The box puts in evidence the range on the stress-strain curves from where the elastic properties were taken. The same range has been applied for all the graphs related to the uniaxial tests.

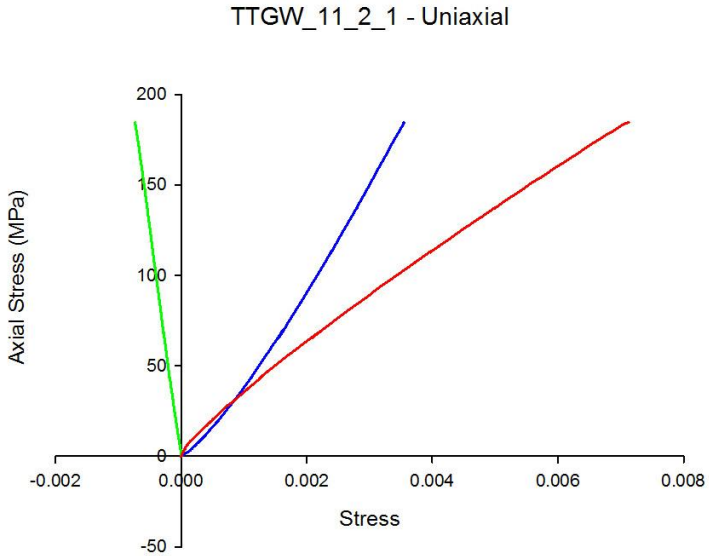

A 2: Stress-strain curves. The trends are linear, similar to Fig.3.9. The axial strain curve is affected by errors due likely to the strain gauges.

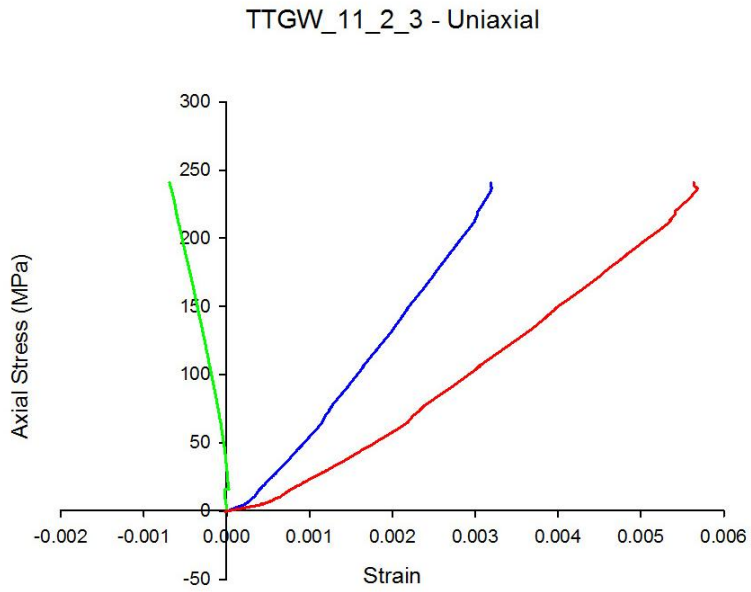

A 3: Stress-strain curves. The trends are linear, similar to Fig.3.9. The stress-strain curves are affected by errors/noise due likely to the strain gauges.

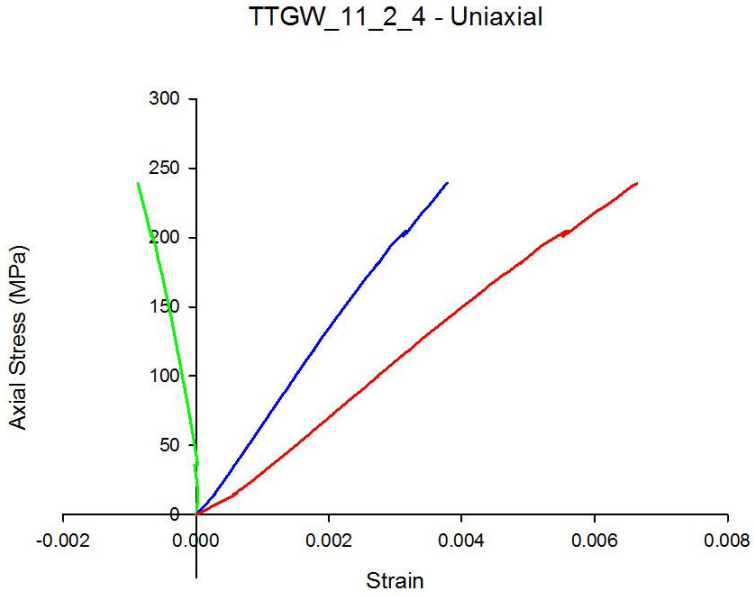

A 4: Stress-strain curves. The trends are linear, similar to Fig.3.9. The stress-strain curves are affected by errors/noise due likely to the strain gauges.

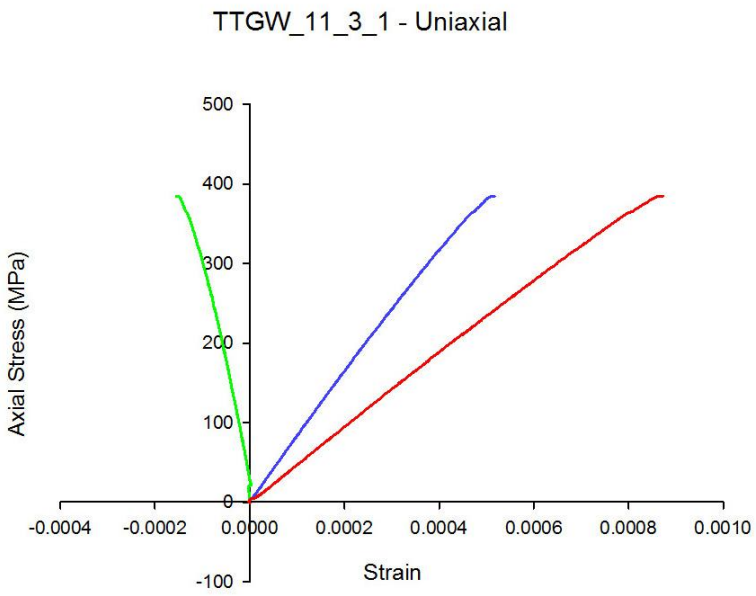

A 5: Stress-strain curves. The trends are linear, similar to Fig.3.9. The stress-strain curves do not appear affected by errors/noise due likely to the strain gauges.

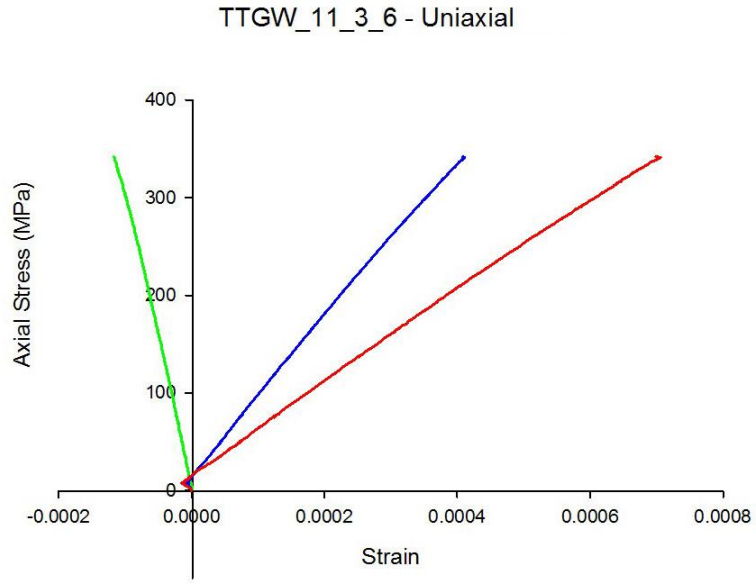

A 6: Stress-strain curves. The trends are linear, similar to Fig.3.9. The stress-strain curves do not appear affected by errors/noise due likely to the strain gauges.

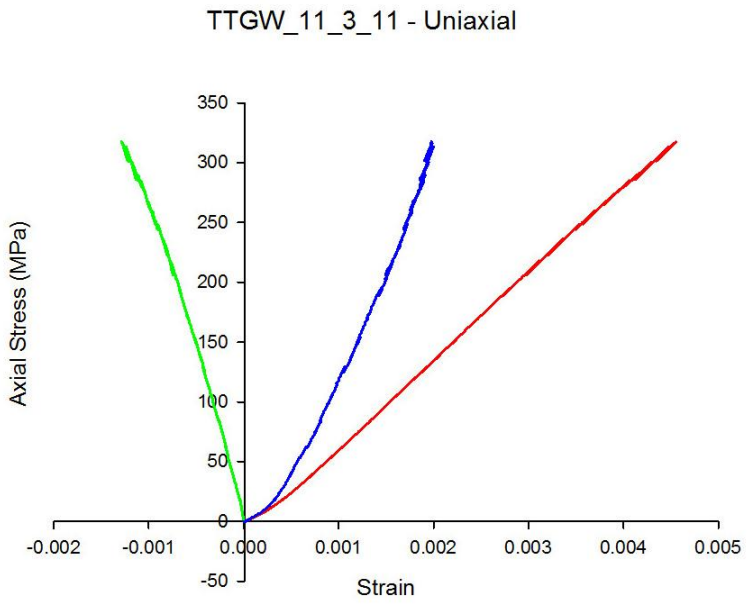

A 7: Stress-strain curves. The trends are linear, similar to Fig.3.9. The stress-strain curves do not appear affected by errors/noise due likely to the strain gauges.

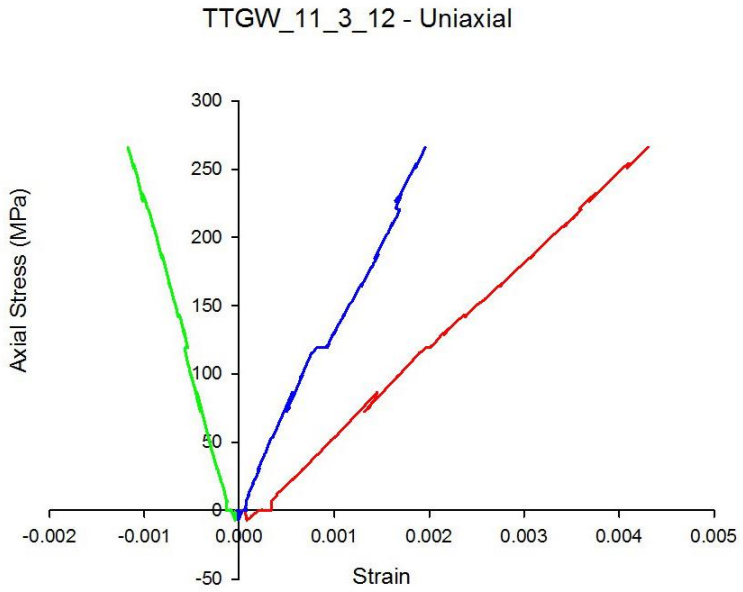

A 8: Stress-strain curves. The trends are linear, similar to Fig.3.9. The stress-strain curves are affected by errors/noise due likely to the strain gauges.

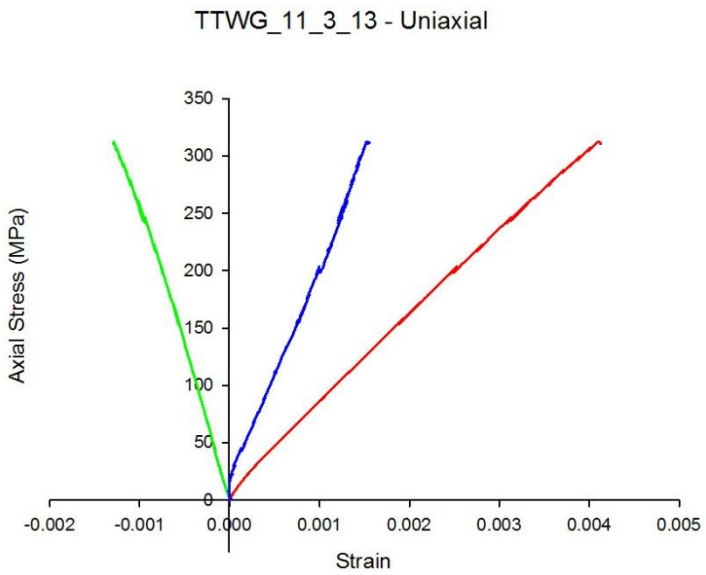

A 9: Stress-strain curves. The trends are linear, similar to Fig.3.9. The stress-strain curves are affected by errors/noise due likely to the strain gauges.

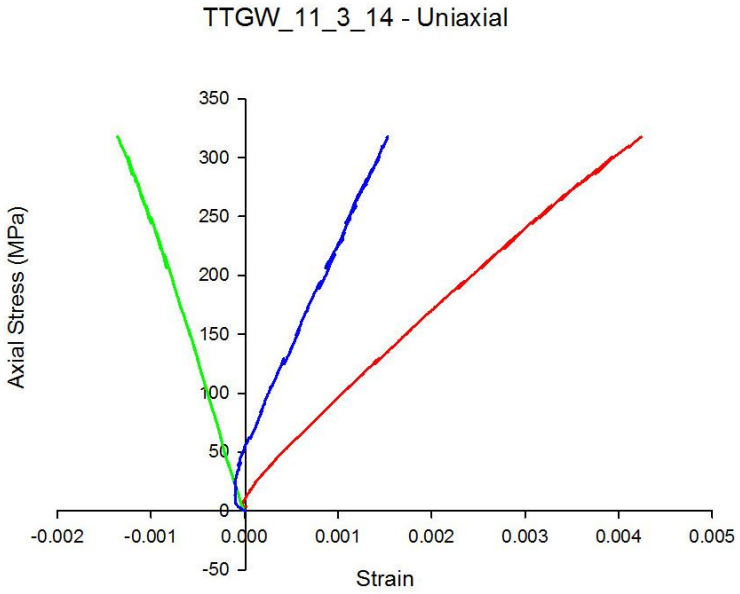

A 10: Stress-strain curves. The trends are linear, similar to Fig.3.9. The stress-strain curves are affected by errors/noise due likely to the strain gauges.

SEISMIC WAVES - GRAPHS:

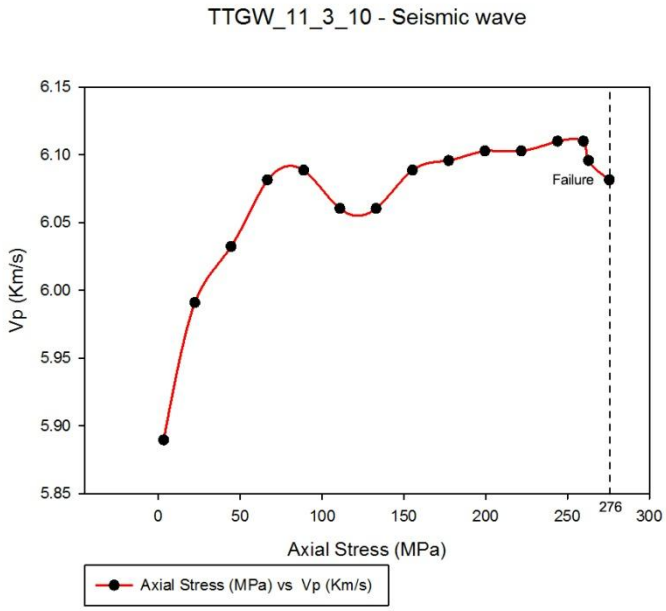

A 11: Vp: the velocity increases increasing the axial stress. The trend increases swinging and gets stability around up to 6.10 km/s. It shows a small decrease before the failure.

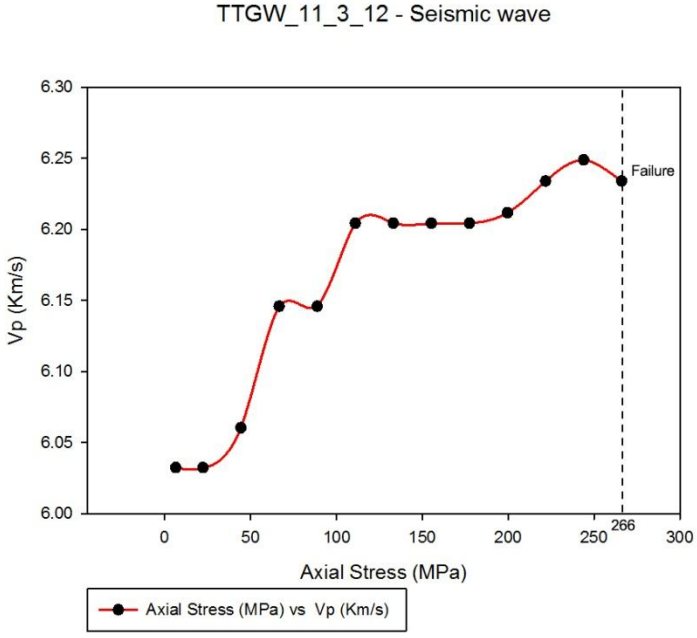

A 12: Vp: the velocity increases increasing the axial stress. The trend looks like to have a "step evolution".

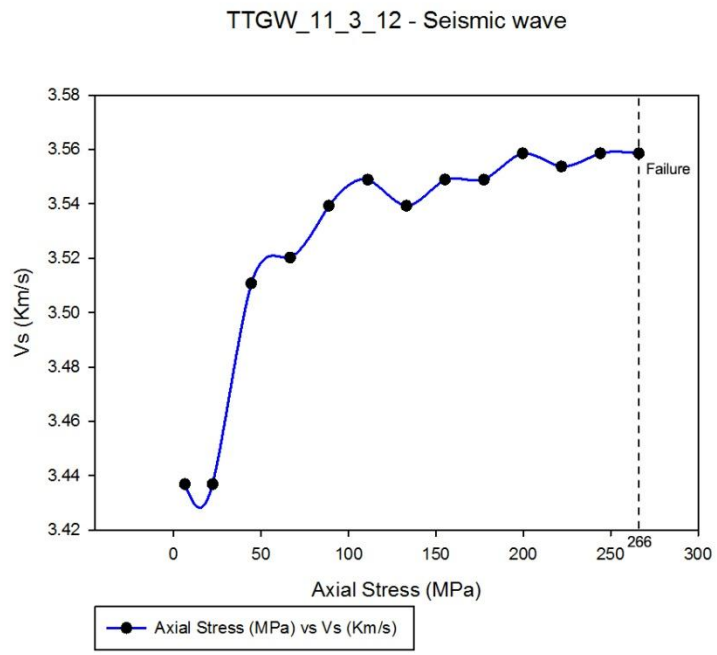

A 13: Vs: the velocity increases increasing the axial stress. The trend looks like to get a stability up to 3.54 km/s.

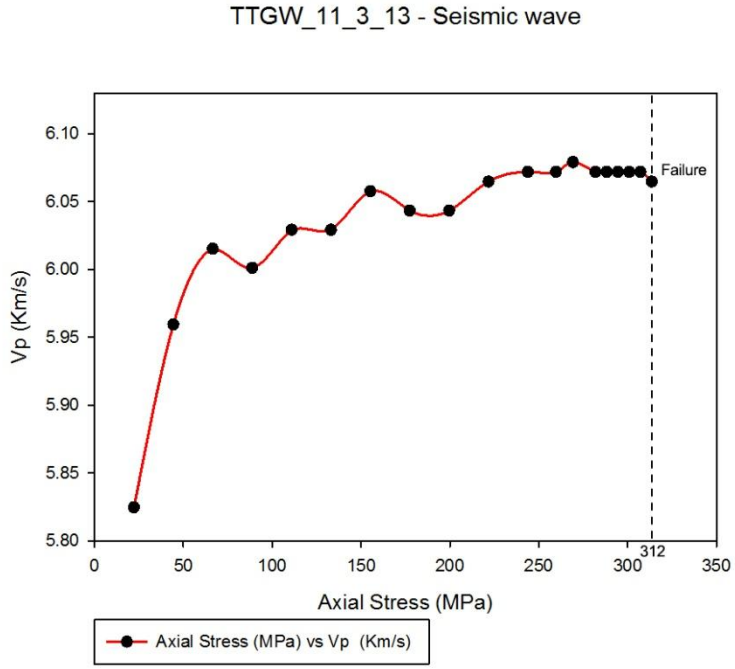

A 14: Vp: the velocity increases increasing the axial stress. The trend increases swinging and gets a stability up to 6.05 km/s.

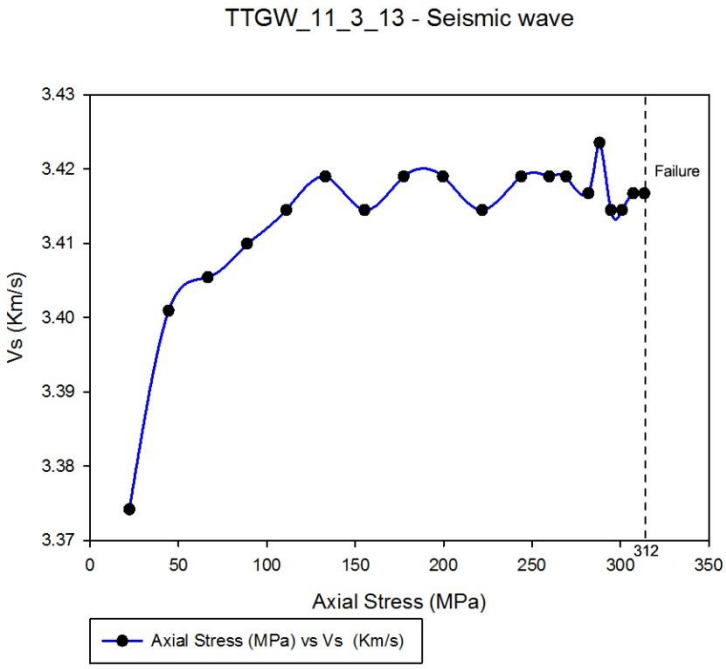

A 15: Vs: the velocity increases increasing the axial stress. It shows a swinging trend.

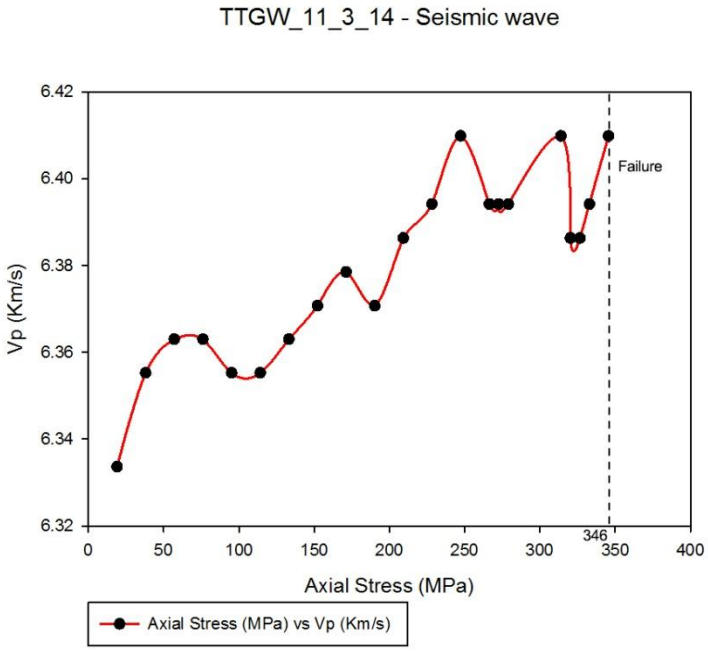

A 16: Vp: the velocity increases increasing the axial stress. The trend shows large swinging.

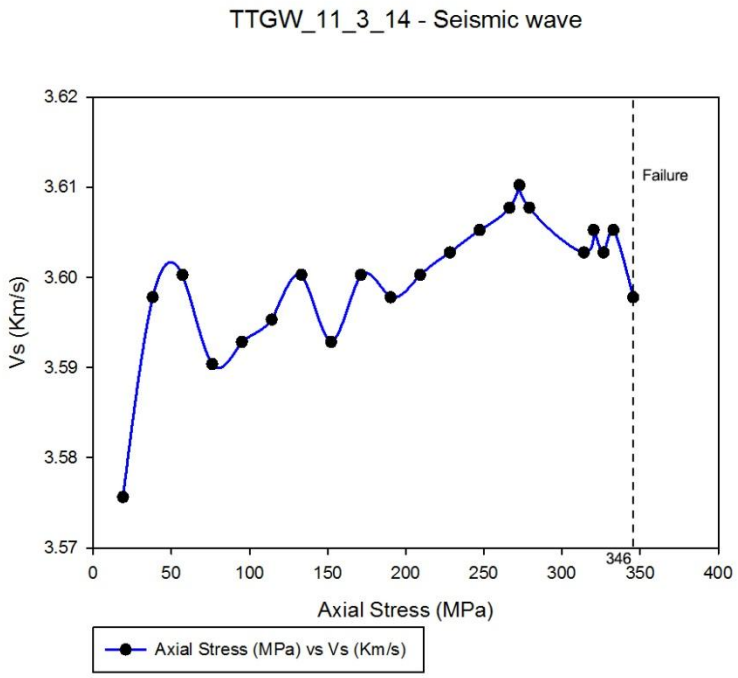

A 17: Vs: the velocity increases increasing the axial stress. The trend shows large swinging.

PERMEABILITY - GRAPH:

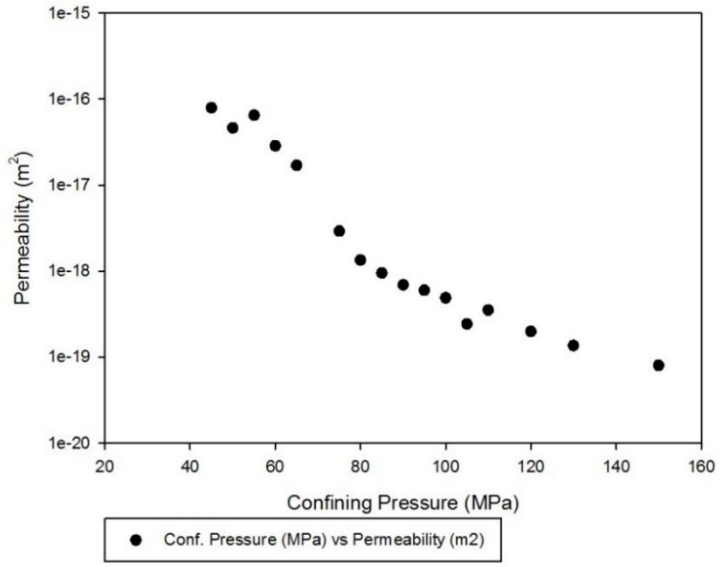

A 18: Permeability through the single fracture for the sample TTGW_11_3_17. Each black spot is a measurement of permeability and can be noted how the permeability decrease increasing the confining pressure. The dashed line indicates where the permeability becomes stable, signing the moment whereby the fracture is closed (but not totally sealed).

THERMO ANALYSIS - GRAPHS:

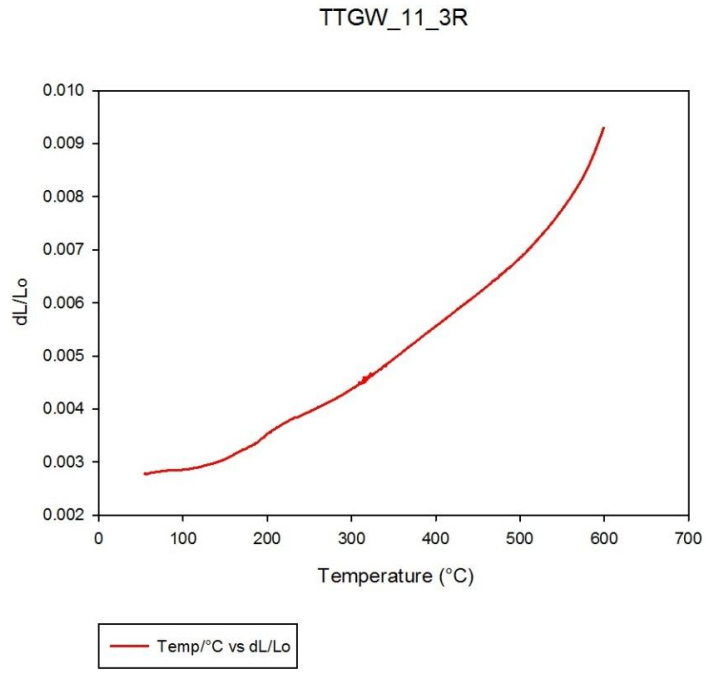

A 19: Linear displacement curves for Waipapa greywacke ($\delta L/L_0$) during linear thermal expansion testing.

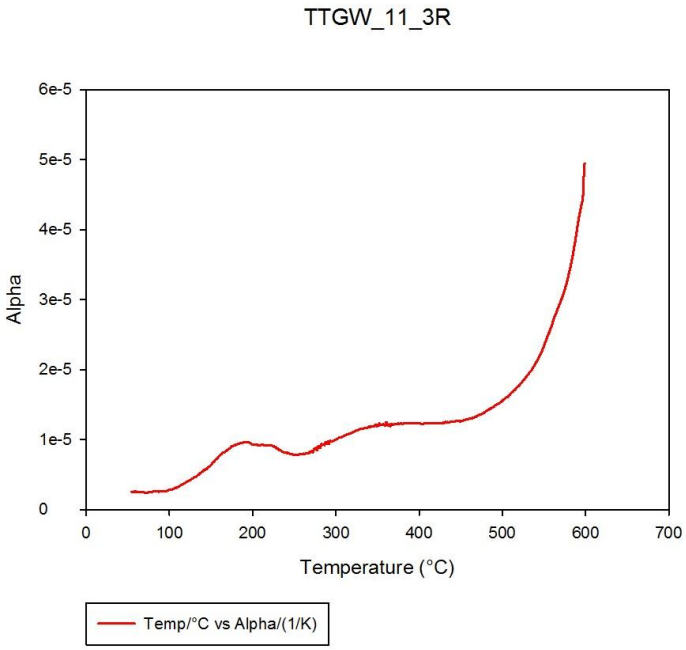

A 20: Linear expansion coefficient α for Waipapa greywacke plotted versus temperature.

APPENDIX B: FIGURES

SAMPLES:

A 21: Greywacke cored samples.

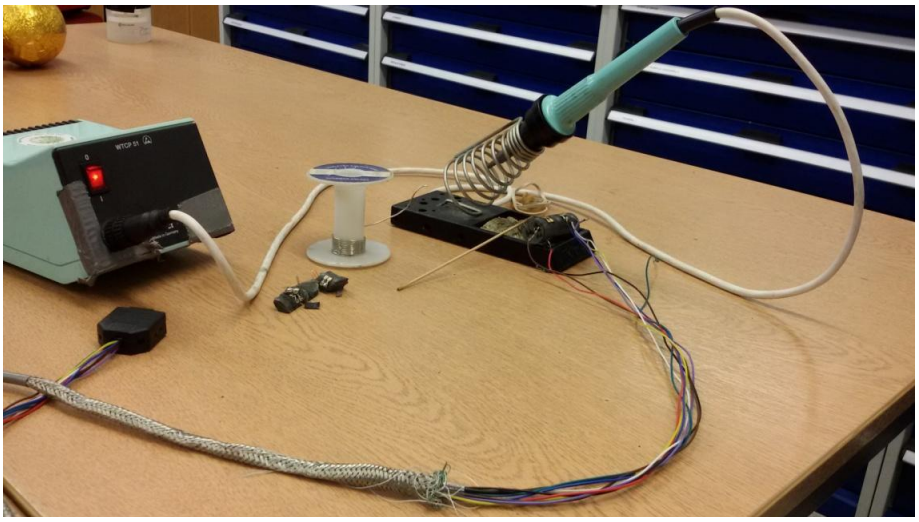

A 22: Welding equipment used to solder the connector cables to the strain gauges in order to measure the deformation.

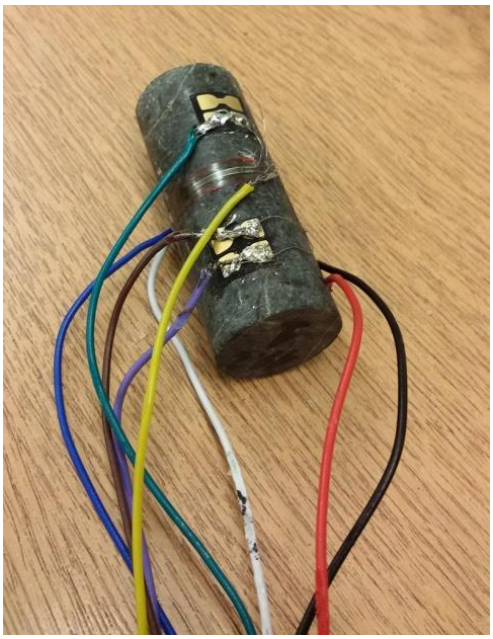

A 23: Strain gauges applied and welded to the cables.

A 24: Greywacke blocks obtained from the core tested in the triaxial test (right) and in the Brazilian jig (left) have been stuck with epoxy resin in order to be polished and observed to the SEM.

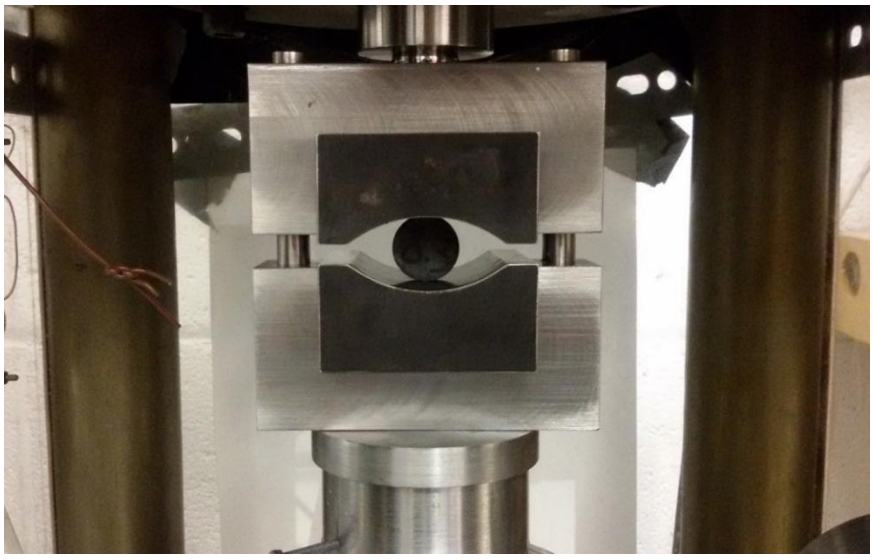

A 25: Frontal view of Brazilian jig inside the press during a Brazilian test.

BIBLIOGRAPHY

Acocella, V., Spinks, K., Cole, J.W., Nicol, A., 2003, Oblique back arc rifting of Taupo Volcanic Zone, New Zealand. Tectonics, 22, pp. 1178-1199.

Adam, L., and M. Batzle (2008), Elastic properties of carbonates from laboratory measurements at seismic and ultrasonic frequencies, Lead. Edge, 27, pp. 1026–1032.

Adams, C.J.; Graham, I.J., 1996, Metamorphic and tectonic geochronology of the Torlesse Terrane, Wellington, New Zealand, New Zealand Journal of Geology and Geophysics, 39, pp. 157-180.

Adams, C.J., Mortimer, N., Campbell, H.J., Griffin, W.L., 2009, Age and isotropic characterisation of metasedimentary rocks from the Torlesse Supergroup and Waipapa Group in the central North Island, New Zealand, New Zealand Journal of Geology and Geophysics, 52, pp. 149-170.

Alcaraz, S., A., Rattenbury, M., S., Soengkono, S., Bignall, G., Lane, R., 2012, A 3D multi-disciplinary interpretation of the basement of the Taupo Volcanic Zone, New Zealand. Proceedings: Thirty-Seventh Workshop on Geothermal Reservoir Engineering, Stanford University, Stanford, CA, pp. 294-301.

Allan, A.S.R., Baker, J.A., Carter, L., Wysoczanski, R.J., 2008, Reconstructing the Quaternary evolution of the world's most active silicic volcanic system: insights from an ~1.65 Ma deep ocean tephra record sourced from Taupo Volcanic Zone, New Zealand, Quaternary Science Reviews, 27, pp. 2341–2360.

Allan, A.S.R., Wilson, C.J.N., Millet, M.-A., Wysoczanski, R.J., 2012, The invisible hand: tectonic triggering and modulation of a rhyolitic super eruption, Geology, 40, pp. 563–566.

Alloway, B., Westgate, J., Pillans, B., Pearce, N.J.G., Newnham, R.M., Byrami, M., Aarburg, S., 2004, Stratigraphy, age and correlation of middle Pleistocene silicic tephras in the Auckland region, New Zealand: a prolific distal record of Taupo Volcanic Zone volcanism, New Zealand Journal of Geology and Geophysics, 47, pp. 447–479.

Alloway, B.V., Pillans, B.J., Carter, L., Naish, T.R., Westgate, J.A., 2005, Onshore–offshore correlation of Pleistocene rhyolitic eruptions from New Zealand: implications for TVZ eruptive history and paleoenvironmental construction, Quaternary Science Reviews, 24, pp. 1601–1622.

ASTM, 1997a, Standard test method for laboratory determination of pulse velocities and ultrasonic elastic constants of rock (D2845-95). 1997 Annual Book of ASTM Standards, Vol. 4.08. American Society for Testing and Materials (ASTM), Philadelphia, pp. 254–259.

ASTM, 2008, Standard Test Method for Splitting Tensile Strength of Intact Rock Core Specimens (D3967−08), American Society for Testing and Materials (ASTM), West Conshohocken, pp. 1-3.

Bernabe, Y. (1987). The effective pressure law for permeability during pore pressure and confining pressure cycling of several crystalline rocks. Journal of Geophysical Research, 92, pp. 68-93.

Baechler, D., T. Kohl, and L. Rybach, 2003, Impact of graben‐parallel faults on hydrothermal convection: The Rhine Graben case study, Physics and Chemistry of the Earth, 28, pp. 431‐441.

Bauer, K., Moeck, I., Norden, B., Schulze, A., Weber, M., Wirth, H., 2010, Tomographic P wave velocity and vertical velocity gradient structure across the geothermal site Groß Schönebeck (NE German Basin): Relationship to lithology, salt tectonics, and thermal regime. Journal of Geophysical Research, 115, pp. 112-134.

Beetham, R.D.; Watters, W.A. 1985, Geology of Torlesse and Waipapa terrane basement rocks encountered during the Tongariro power development project, North Island, New Zealand, New Zealand Journal of Geology and Geophysics, 28, pp. 575-594.

Begg & Mazengarb, 1996, part Q27, scale 1:50,000. Lower Hutt: Institute of Geological & Nuclear Sciences. Institute of Geological & Nuclear Sciences geological map 22. 128 p. + 1 fold. Map.

Bibby, H., Caldwell, T., Davey, F., Webb, T., 1995, Geophysical evidence on the structure of the Taupo Volcanic Zone and its hydrothermal circulation, Journal of Volcanology and Geothermal Research, 68, pp. 29-58.

Bibby, H.M.; Caldwell, T.G.; Risk, G.F.; Bennie, S.L. 1999, The Matahana Basin resistivity anomaly: implications for geothermal exploration in the Taupo Volcanic Zone. IN: Simmons, S.F. (comp.); Morgan, O.E. (comp.); Dunstall, M.G. (comp.) Proceedings of the 21st New Zealand Geothermal Workshop 1999, Auckland, NZ: University of Auckland. Proceedings of the New Zealand Geothermal Workshop, 21, pp. 113-118.

Bishop, D.G.; Macfarlane, D.F.; Oliver, P.J. 1985, Geology of the lower Clutha region. IN: Gilchrist, C. (ed.) Research notes 1985, Lower Hutt: New Zealand Geological Survey. Record / New Zealand Geological Survey, 8, pp. 4-10.

Black, P.M., 1994, The "Waipapa Terrane", North Island, New Zealand: subdivision and correlation. IN: Wada, H. Memorial volume to the late Professor Teruhiko Sameshima. Shizuoka, Japan: Institute of Geosciences. Geoscience reports of Shizuoka University, 20, pp. 55-62.

Black, P.M., 1993, Basement terranes, northern North Island. IN: Froggatt, P. (ed.) Geological Society of New Zealand Inc 1993 Annual Conference, Victoria University of Wellington, 6 - 10 December: program and abstracts. [Lower Hutt]: Geological Society of New Zealand. Geological Society of New Zealand miscellaneous publication, 79a, pp. 40.

Blake O. O., 2011, Seismic Transport Properties of Fractured Rocks.

Blake O. O. and Faulkner D. R., 2016, The effect of fracture density and stress state on the static and dynamic bulk moduli of Westerly granite. Journal of Geophysical Research: Solid Earth, 121, pp. 2382–2399.

Brace, W., F., 1965, Relation of elastic properties of rocks to fabric. Journal of Geophysical Research, 70, pp. 5657–5667.

Brace, W. F., J. B. Walsh, and W. T. Frangos 1968, Permeability of granite under high pressure, Journal Geophysical Research, 73, pp. 2225 – 2236.

Brace, W. F. 1980, Permeability of Crystalline and Argillaceous Rocks, International Journal of Rock Mechanics and Mining Sciences, 17, pp. 241-251.

Bradshaw, J.D.; Andrews, P.B.; Adams, C.J. 1981, Carboniferous to Cretaceous on the Pacific margin of Gondwana: the Rangitata phase of New Zealand. IN: Cresswell, M.M.; Vella, P. (eds.) Gondwana five: selected papers and abstracts of papers presented at the Fifth International Gondwana Symposium. Rotterdam: A.A. Balkema, pp. 217-221.

Bradshaw, J.D. 1993, A review of the Median Tectonic Zone: terrane boundaries and terrane amalgamation near the Median Tectonic Line. New Zealand Journal of Geology and Geophysics, 36, pp. 117-125.

Brathwaite, R.L.; Wood, C.P.; Rosenberg, M.D.; Faure, K., 2002, Porosity and permeability in the basement rocks at the Kawerau and Ohaaki geothermal fields, New Zealand. IN: Soengkono, S.; Browne, P.R.L. (eds) Proceedings of the 24th New Zealand Geothermal Workshop, 2002. [Auckland]: University of Auckland. Proceedings of the New Zealand Geothermal Workshop, 24, pp. 49-54.

Bromley, C.J.; Glover, R.B., 1996, Changes in shallow hydrology of the Tauhara geothermal field. IN: Simmons, S.F.; Rahman, M.M.; Watson, A. (eds.) Proceedings of the 18th New Zealand Geothermal Workshop, 1996. Auckland: University of Auckland, pp. 63-68.

Bryan, C.J.; Sherburn, S.; Bibby, H.M.; Bannister, S.C.; Hurst, A.W., 1999, Shallow seismicity of the central Taupo Volcanic Zone, New Zealand: its distribution and nature, New Zealand Journal of Geology and Geophysics, 42, pp. 533-542.

Campbell, H.J., 1982, Halobia (Bivalvia, Triassic) and a gastropod from Torlesse Supergroup rock of Wellington, New Zealand. New Zealand Journal of Geology and Geophysics, 25, pp. 487-492.

Carslaw, H. S., Jaeger, J. C., 1959, Conduction of heat in solids. 2nd Edition, Oxford University Press.

Carter, L., Shane, P., Alloway, B., Hall, I.R., Harris, S.E., Westgate, J.A., 2003, Demise of one volcanic zone and birth of another – a 12 m.y. marine record of major rhyolitic eruptions from New Zealand, Geology, 31, pp. 493–496.

Carter, L., Alloway, B.V., Shane, P., Westgate, J.A., 2004, Deep-ocean record of major late Cenozoic rhyolitic eruptions from New Zealand, New Zealand Journal of Geology and Geophysics, 47, pp. 481–500.

Chambefort, I., Lewis, B., Wilson, C.J.N., Rae, A.J., Coutts, C., Bignall, G., Ireland, T.R., 2014, Stratigraphy and structure of the Ngatamariki geothermal system from new zircon U–Pb geochronology: implications for Taupo Volcanic Zone evolution. Journal of Volcanology and Geothermal Research, 274, pp. 51–70.

Christiansen, R.L., 2001, The Quaternary and Pliocene Yellowstone Plateau Volcanic Field of Wyoming, Idaho, and Montana. United States Geological Survey Professional Paper, 729-G., pp. 1–143.

Cole, J.W., 1979, Structure, petrology and genesis of Cenozoic volcanism, Taupo Volcanic Zone, New Zealand – a review, New Zealand Journal of Geology and Geophysics, 22, pp. 631–657.

Cole, J.W., Lewis, K.B., 1981, Evolution of the Taupo-Hikurangi subduction system. Tectonophysics, 72, pp. 1–21.

Cole, J.W., Thordarson, T., Burt, R.M., 2000, Magma origin and evolution of White Island (Whakaari) volcano, Bay of Plenty, New Zealand. Journal of Petrol, 41, pp. 867–895.

Cronin, S.J., Neall, V.E., 1997, A late Quaternary stratigraphic framework for the northeastern Ruapehu and eastern Tongariro ring plains, New Zealand. New Zealand Journal of Geology and Geophysics, 40, pp. 185–197.

Danisík, M., Shane, P., Schmitt, A.K., Hogg, A., Santos, G.M., Storm, S., Evans, N.J., Fifield, L.K., Lindsay, J.M., 2012, Re-anchoring the late Pleistocene tephro

chronology of New Zealand based on concordant radiocarbon ages and combined 238U/230Th disequilibrium and (U–Th)/He zircon ages, Earth Planet, Sci. Lett., 349, pp. 240–250.

Donoghue, S.L., Neall, V.E., Palmer, A.S., 1995, Stratigraphy and chronology of late Quaternary andesitic tephra deposits, Tongariro Volcanic Centre, New Zealand. Journal of the Royal Society of New Zealand, 25, pp. 115–206.

Downs, D.T., Rowland, J.V., Wilson, C.J.N., Rosenberg, M.D., Leonard, G.S., Calvert, A.T., 2014a, Evolution of the intra-arc Taupo-Reporoa Basin within the Taupo Volcanic Zone of New Zealand, Geosphere, 10, pp. 185–206.

Eastwood, A.A., Gravley, D.M., Wilson, C.J.N., Chambefort, I., Oze, C., Cole, J.W., Ireland, T.R., 2013, U–Pb dating of subsurface pyroclastic deposits (Tahorakuri Formation) at Ngatamariki and Rotokawa geothermal fields. IN: Proceedings, 35th New Zealand Geothermal Workshop, Rotorua, New Zealand, pp. 147-162.

Faulkner, D. R. 1997, The role of clay-bearing fault gouges in controlling fluid pressures in fault zones: implications for faults mechanics. Ph.D. Thesis, University of Manchester, UK, 1997, 279 pp.

Fischer, G. J. 1992, The determination of permeability and storage capacity: Pore pressure oscillation method, in Fault Mechanics and Transport Properties of Rocks, edited by B. Evans and T.-F. Wong, Academic, London, pp. 187– 212.

Gamble, J.A., Wright, I.C., Baker, J.A., 1993, Seafloor geology and petrology in the oceanic to continental transition zone of the Kermadec-Havre-Taupo Volcanic Zone arc system, New Zealand. New Zealand Journal of Geology and Geophysics, 36, pp. 417–435.

Gangi, A. F., 1978, Variation of Whole and Fractured Porous Rock Permeability with Confining Pressure. International Journal of Rock Mechanics and Mining Sciences & Geomechanics, Pergamon Press, Vol. 15, pp. 249-257.

Graham, I.J., Korsch, R.J., 1989, Rb-Sr resetting ages and chemical characterization of turbidites in an accretionary wedge: Torlesse Complex, Otaki Gorge, New Zealand. Geological Society of America Bulletin, 101, pp. 355-363.

Grant-Mackie, J.A., 1978, Mesozoic chronostratigraphy, New Zealand-New Caledonia: Project 8. IN: Basset, M.G. (ed.) International Geological Correlation Programme (IGCP): scientific achievements 1973-1977. Paris: Unesco, Geological correlation, Special issue, pp. 54-57.

Grant-Taylor, T.L.; Waterhouse, J.B. ,1963, Monotis from the Tararua Range, Wellington. New Zealand Journal of Geology and Geophysics, 6, pp. 623-627.

Gravley, D.M., Wilson, C.J.N., Rosenberg, M.D., Leonard, G.S., 2006, The nature and age of Ohakuri Formation and Ohakuri Group rocks in surface exposures and geothermal drill hole sequences in the central Taupo Volcanic Zone, New Zealand. New Zealand Journal of Geology and Geophysics, 49, pp. 305–308.

Gravley, D.M., Wilson, C.J.N., Leonard, G.S., Cole, J.W., 2007, Double trouble: paired ignimbrite eruptions and collateral subsidence in the Taupo Volcanic Zone, New Zealand, Geological Society of America Bulletin, 119, pp. 18–30.

Grim, R. E., 1968, Clay Mineralogy, 2nd ed. McGraw-Hill, New York.

Grindley, G.W., 1965, The Geology, Structure and Exploitation of the Wairakei Geothermal Field, Taupo, New Zealand, New Zealand Geological Survey Bulletin, 75, pp. 1-131.

Grindley, G.W.; Mumme, T.C.; Kohn, B.P. 1994, Stratigraphy, paleomagnetism, geochronology and structure of silicic volcanic rocks, Waiotapu/Paeroa range area, New Zealand, Geothermics, 23, pp. 473-499.

Guo H., Aziz N.I. and Schmidt L.C., 1993, Rock fracture-toughness determination by the Brazilian test. Engineering Geology, 33, pp. 177-188.

Hammond, J. P., L. T. Ratcliff, C. R. Brinkman, and J. C. W. Nestor (1979), Dynamic and static measurements of elastic constants with data on 2 I/4 Cr-1 Mo steel, types 304 and 316 stainless steels, and alloy 800H, ORNL-5442, Oak Ridge National Laboratory, Oak Ridge, Tenn., pp. 1-24.

Hauksson, E., and J. Unruh, 2007, Regional tectonics of the Coso geothermal area along the intracontinental plate boundary in central eastern California: Three-dimensional Vp and Vp/Vs models, spatial-temporal seismicity patterns, and seismogenic deformation, Journal Geophysics Research, 112, pp.72-86.

Healy, J., 1962, Structure and volcanism in the Taupo Volcanic Zone New Zealand. In: Macdonald, G.A., Kuno, H. (Eds.), Crust of the Pacific Basin. American Geophysical Union, Geophysical Monograph 6, Washington, DC, pp. 151–157.

Healy, J.; Hochstein, M.P. 1973, Horizontal flow in hydrothermal systems. Journal of hydrology, New Zealand, 12, pp. 71-81.

Heap, M.J. and Faulkner, D.R., 2008, quantifying the evolution of static elastic properties as crystalline rock approaches failure. International Journal of Rock Mechanics and Mining Sciences, 45, pp. 564-573.

Heap,M.J., Lavallée, Y., Laumann, A., Hess, K.-U., Meredith, P.G., Dingwell, D.B., 2012, How tough is tuff in the event of fire? Geology, 40, pp. 311–314.

Henneburger, R.C.; Browne, P.R.L. 1988, Hydrothermal alteration and evolution of the Ohakuri hydrothermal system, Taupo Volcanic Zone, New Zealand. Journal of Volcanology and Geothermal Research, 34, pp. 211-231.

Henrys, S.A. 1987, Structure of the Broadlands-Ohaaki Geothermal Field (New Zealand) based on interpretation of seismic and gravity data. PhD (Geology) thesis, University of Auckland.

Hochstein, M.P., 1995, Crustal heat transfer in the Taupo Volcanic Zone (New Zealand): comparison with other volcanic arcs and explanatory heat source models, Journal of Volcanology and Geothermal Research, 68, pp. 117–151.

Holt, K. 2007, Quaternary geology and uplift rates on Chatham Island. IN: Mortimer, N.; Wallace, L.M. (eds) Geological Society of New Zealand & New Zealand Geophysical Society Joint Annual Conference: launching International Year of Planet Earth, 26-29 November 2007, Tauranga: programme and abstracts. Lower Hutt: Geological Society of New Zealand. Geological Society of New Zealand miscellaneous publication 123A, pp. 73-89.

Hurwitz, S., Lowenstern, J.B., 2014, Dynamics of the Yellowstone hydrothermal system. Reviews of Geophysics, 51, pp. 375–411.

Jaeger, J.C., Cook, G.W. & Zimmerman, R. 2009. Fundamentals of rock mechanics. Blackwell, Oxford, pp. 282-320.

Jessop, A. M., Hobart, M. A., and Sclater, J. G., 1976. The world heat-flow data collection - 1975. Geothermal Series Number 5, Ottawa, Canada, 125, pp. 213-226.

Jizba, D., 1991), Mechanical and Acoustical Properties of Sandstones and Shales, Stanford University, pp. 260-275.

Jurado-Chichay, Z., Walker, G.P.L., 2000, Stratigraphy and dispersal of the Mangaone Subgroup pyroclastic deposits, Okataina Volcanic Centre, New Zealand, Journal of Volcanology and Geothermal Research, 104, pp. 319–383.

Keall, J. M., 1988, Volcanology and ignimbrite stratigraphy along the Paeroa Fault, Taupo Volcanic Zone, MSc (Geology) thesis, Victoria University of Wellington.

Kear, D., 1971, Basement rock facies: northern North Island, New Zealand Journal of Geology and Geophysics, 14, pp. 275-283.

Keshavarz, M., Pellet, F.L., Loret, B., 2010, Damage and changes in mechanical properties of a gabbro thermally loaded up to 1000 °C. Pure Applied Geophysics, 167, pp. 1511–1523.

Kimbrough, D.L.; Tulloch, A.J.; Coombs, D.S.; Landis, C.A.; Johnston, M.R.; Mattinson, J.M. 1994, Uranium-lead zircon ages from the Median Tectonic Zone, New Zealand, New Zealand Journal of Geology and Geophysics, 37, pp. 393-419.

Kuttruff, H., 1991, Ultrasonics fundamentals and applications. Elsevier, Science & Technology; New York.

Landau L.D. and Lifshitz E.M., Mechanics, 3rd ed., 1976, Pergamon Press, New York, pp. 192-195.

Lees, J., M., Wu, H., 1999a, Vp wave anisotropy, stress, and crack distribution at Coso geothermal field, California. Journal of Geophysical Research, 104, pp. 955–973.

Leonard, G.S., Begg, J.G., Wilson, C.J.N. (compilers), 2010, Geology of the Rotorua area: scale 1:250,000. Institute of Geological & Nuclear Sciences 1:250,000.

Lin, W., 2002, Permanent strain of thermal expansion and thermally induced microcracking in Inada granite, Journal of Geophysics Research, 107, pp. 2215-2229.

Lo, K.Y., Wai, R.S.C., 1982, Thermal expansion, diffusivity, and cracking of rock cores from Darlington, Ontario, Canada, Geotechnical Journal, 19, pp. 154–166.

Lockner, D.A., 1995, Rock failure, T.J. Ahrens (Ed.), Rock Physics and Phase Relations: A Handbook of Physical Constants, The American Geophysical Union, pp. 127–147.

Luyendyk, B.P., 1995, Hypothesis for Cretaceous rifting of East Gondwana caused by subducted slab capture. Geology, 23, pp. 373–376.

MacKinnon, D.I., 1983. A late Middle Cambrian orthide-kutorginide brachiopod fauna from Northwest Nelson, New Zealand. New Zealand Journal of Geology and Geophysics, 26, pp. 97-102.

Manning, D.A., 1995, Late Pleistocene tephrostratigraphy of the Eastern Bay of Plenty Region, New Zealand, Victoria University, Wellington, New Zealand.

Manning, D.A., 1996, Middle–late Pleistocene tephrostratigraphy of the eastern Bay of Plenty, New Zealand, Quaternary International, 36, pp. 3–12.

Manville, V.R., 2001, Environmental impacts of large-scale explosive rhyolitic eruptions in the central North Island: field trip FT2. IN: Smith, R.T. (ed.) Geological Society of New Zealand annual conference 2001, 27-29 November, Hamilton: Advances in geosciences: fieldtrip guides. [Wellington]: Geological

Society of New Zealand. Geological Society of New Zealand miscellaneous publication, 110, pp. 19-34.

Manville, V.R.; Wilson, C.J.N. 2004, The 26.5 ka Oruanui eruption, New Zealand: a review of the roles of volcanism and climate in the post-eruptive sedimentary response, New Zealand, Journal of Geology and Geophysics, 47, pp. 525-547.

Mavko, G., Mukerji, T. & Dvorkin, J., 2009. The rock physics handbook: tools for seismic analysis of porous media, 2nd ed., Cambridge University Press, Cambridge, pp. 185-190.

McLean, K.; McNamara, D. 2010, Refinement of feed zone interpretation from completion testing using AFIT. IN: Hoskin, P.; Hikuroa, D.; Eccles, J. (conveners) GeoNZ 2010: geoscience, geothermal: abstract volume: Auckland, 21-24 November 2010, Wellington: Geoscience Society of New Zealand, Geoscience Society of New Zealand miscellaneous publication 129A, pp. 189-203.

McLean, K.; McNamara, D. 2011, Fractures interpreted from acoustic formation imaging technology: correlation to permeability. IN: Proceedings, thirty sixth Workshop Geothermal Reservoir Engineering, January 31 - February 2, 2011, Stanford University. Stanford, Calif.: Stanford University, Stanford Geothermal Program Workshop report SGP-TR-191, pp. 103-112.

McNamara et al, 2014, McNamara, D.D.; Faulkner, D.; McCarney, E. 2014 Rock Properties of Greywacke Basement Hosting Geothermal Reservoirs, New Zealand: preliminary results. IN: Proceedings, Thirty Ninth Workshop Geothermal Reservoir Engineering, February 24-26, 2014. Stanford, Calif.: Stanford University. Stanford Geothermal Program Workshop report SGP-TR-202, pp. 10-21.

McNamara D., Cècile M., Lewis B., Wallis I., 2015, Heterogeneity of structure and stress in the Rotokawa Geothermal Field, New Zealand. Journal of Geophysical Research: Solid Earth, 120, pp. 1243 - 1262.

Milicich, S.D., Wilson, C.J.N., Bignall, G., Pezaro, B., Charlier, B.L.A., Wooden, J.L., Ireland, T.R., 2013a, U–Pb dating of zircon in hydrothermally altered rocks of the Kawerau Geothermal Field, Taupo Volcanic Zone, New Zealand, Journal of Volcanology and Geothermal Research, 253, pp. 97–113.

Milicich, S.D., Clark, J.P., Wong, C., Askari, M., 2016, A review of the Rotokawa Geothermal Field, New Zealand, Geothermics, 59, pp. 281-293.

Mitchell, T., M., and Faulkner, D., R., 2008, Experimental measurements of permeability evolution during triaxial compression of initially intact crystalline rocks and implications for fluid flow in fault zones. Journal of Geophysical Research, 113, doi:10.1029/2008JB005588.

Mockovčiaková, A., and B. Pandula (2003), Study of the relation between the static and dynamic moduli of rocks, Metalurgija, 1, pp. 37–39.

Moebis, A., Cronin, S.J., Neall, V.E., Smith, I.E., 2011, Unravelling a complex volcanic history from fine-grained, intricate Holocene ash sequences at the Tongariro Volcanic Centre, New Zealand, Quaternary International, 246, pp. 352–363.

Mortimer, N., 1993a, Jurassic tectonic history of the Otago Schist, New Zealand, Tectonics, 12, pp. 237–244.

Mortimer, N., 1994, Origin of the Torlesse Terrane and coeval rocks, North Island, New Zealand, International Geology Review, 36, pp. 891–910.

Mortimer, N., 2004, New Zealand's geological foundations. Gondwana Research, 7, pp. 261–272.

Mortimer, N., Gans, P.B., Palin, J.M., Meffre, S., Herzer, R.H., Skinner, D.N.B., 2010, Location and migration of Miocene–Quaternary volcanic arcs in the SW Pacific region. Journal of Volcanology and Geothermal Research, 190, pp. 1–10.

Müller, T. M., B. Gurevich, and M. Lebedev (2010), Seismic wave attenuation and dispersion resulting from wave-induced flow in porous rocks - A review, Geophysics, 75a, pp. 147-164.

Multipycnometer - density analysis by gas pycnometer, checked on October 24, 2015, on Quantachrome, http://www.quantachrome.com/density/multipycnometer.html

Nairn, I.A.; Wood, C.P.; Bailey, R.A. 1994, The Reporoa Caldera, Taupo Volcanic Zone: source of the Kaingaroa Ignimbrites. Bulletin of Volcanology, 56, pp. 529-537.

Nairn, I.A., 2002. Geology of the Okataina Volcanic Centre, scale 1:50,000, Institute of Geological & Nuclear Sciences geological map 25, 1 sheet + 156 p. Institute of Geological & Nuclear Sciences Limited, Lower Hutt, New Zealand.

Nara Y., Meredith P.G., Yoneda T. and Kaneko K., 2011, Influence of macro-fractures and micro-fractures on permeability and elastic wave velocities in basalt at elevated pressure, Tectonophysics, 503, pp. 52–59.

Nicol, A., Walsh, J., Berryman, K., Villamor, P., 2006, Interdependence of fault displacement rates and paleo-earthquakes in an active rift, Geology, 34, pp. 865–868.

Pardo, N., Cronin, S.J., Palmer, A.S., Németh, K., 2012, Reconstructing the largest explosive eruptions of Mt. Ruapehu, New Zealand: lithostratigraphic tools to understand subplinian Plinian eruptions at andesitic volcanoes, Bulletin of Volcanology, 74, pp. 617–640.

Paterson, M. and Wong, T., 2005, Experimental rock deformation - The brittle field, Springer-Verlag, pp. 12 -13.

Pillans, B., Alloway, B., Naish, T., Westgate, J., Abbott, S., Palmer, A., 2005, Silicic tephras in Pleistocene shallow-marine sediments of Wanganui Basin, New Zealand, Journal of the Royal Society of New Zealand, 35, pp. 43–90.

Reyners, M., 2013, The central role of the Hikurangi Plateau in the Cenozoic tectonics of New Zealand and the southwest Pacific, Earth and Planetary Science Letters, 361, pp. 460–468.

Rosenberg, M.D., Bignall, G., Rae, A.J., 2009, The geological framework of the Wairakei Tauhara geothermal system, New Zealand, Geothermics, 38, pp. 72–84.

Rowland, J.V., Sibson, R.H., 2001, Extensional fault kinematics within the Taupo Volcanic Zone, New Zealand: soft-linked segmentation of a continental rift system, New Zealand Journal of Geology and Geophysics, 44, pp. 271–283.

Rowland, J.V., Sibson, R.H., 2004, Structural controls on hydrothermal flow in a segmented rift system, Taupo Volcanic Zone, New Zealand, Geofluids, 4, pp. 259–283.

Rowland, J.V., Wilson, C.J.N., Gravley, D.M., 2010, Spatial and temporal variations in magma assisted rifting, Taupo Volcanic Zone, New Zealand, Journal of Volcanology and Geothermal Research, 190, pp. 89–108.

Risk, G.F.; Bibby, H.M.; Caldwell, T.G. 1999, Resistivity structure of the central Taupo Volcanic Zone, New Zealand, Journal of Volcanology and Geothermal Research, 90, pp. 163-181.

Schellart, W.P., Lister, G.S., Toy, V.G., 2006, A Late Cretaceous and Cenozoic reconstruction of the southwest Pacific region: tectonics controlled by subduction and slab rollback processes, Earth-Science Reviews, 76, pp. 191–233.

Schellart, W.P., Spakman, W., 2012, Mantle constraints on the plate tectonic evolution of the Tonga-Kermadec-Hikurangi subduction zone and the South Fiji Basin region, Australian Journal of Earth Science, 59, pp. 933–952.

Schmerr Jr., L. and Song, S., 2007, Ultrasonic Nondestructive Evaluation Systems - Models and Measurements. Springer.

Schoen, J. H. 1996, Physical properties of rocks: Fundamentals and principles of petrophysics, Handbook of Geophysical Exploration: Seismic Exploration, Vol. 18, Pergamon, New York.

Shane, P.A.R., Froggatt, P.C., 1991, Glass chemistry, paleomagnetism, and correlation of middle Pleistocene tuffs in southern North Island, New Zealand, and western Pacific, New Zealand, Journal of Geology and Geophysics, 34, pp. 203–211.

Sherburn, S.; Bannister, S.C.; Bibby, H.M., 2003, Seismic velocity structure of the central Taupo Volcanic Zone, New Zealand, from local earthquake tomography. Journal of Volcanology and Geothermal Research, 122, pp. 69-88.

Sibson, R.H., 1994, Geological evidence for fluid involvement in the rupture processes of crustal earthquakes. IN: Hickman, S.; Sibson, R.; Bruhn, R. Proceedings of

workshop LXIII - The mechanical involvement of fluids in faulting. Menlo Park, CA: US Geological Survey. Open-file report / US Geological Survey, pp. 31-38.

Sibson, R.H., 1996, Rock mechanics of extensional faulting and fracturing in the Taupo Fault Belt. 1 p. IN: New Zealand Geophysical Society 1996 Symposium: Volcanic and extensional processes: Programme and abstracts: Thursday 29 August - Friday 30 August 1996, GNS Wairakei Research Centre, Wairakei, Taupo. [Wellington]: New Zealand Geophysical Society. New Zealand Geophysical Society Inc. Symposium, programme and abstracts 1996.

Sibson, R.H., 1998, Brittle failure mode plots for compressional and extensional tectonic regimes. Journal of Structural Geology, 20, 655-660.

Sibson, R.H.; Rowland, J.V. 2003, Stress, fluid pressure and structural permeability in seismogenic crust, North Island, New Zealand. Geophysical Journal International, 154, 584-594.

Simiyu S. M., 2000, Geothermal reservoir characterization: Application of micro-seismic activity and seismic wave properties. Journal of Geophysics Research, 105, pp. 779-795.

Simmons, S. F., Keywood, M.; Scott, B.J.; Keam, R.F. 1993, Irreversible change of the Rotomahana-Waimangu hydrothermal system (New Zealand) as a consequence of a volcanic eruption. Geology, 21, 643-646.

Simpson, B., 1987, Heat flow measurements on the bay of plenty coast, New Zealand. Journal of Volcanology and Geothermal Research, pp. 25-33.

Siratovich P.A., Von Aulock F.W., Lavallée Y., Cole J.W., Kennedy B.M., Villeneuve M.C., 2015, Thermoelastic properties of the Rotokawa Andesite: A geothermal

reservoir constraint, Journal of Volcanology and Geothermal Research, 301, pp. 1–13.

Smith, I.E.M., Price, R.C., 2006, Tonga-Kermadec arc and Havre-Lau back-arc system: their role in the development of tectonic and magmatic models for the western Pacific, Journal of Volcanology and Geothermal Research, 156, pp. 315–331.

Speden, I.G., 1976 Fossil localities in Torlesse rocks of the North Island, New Zealand. Journal of the Royal Society of New Zealand, 6, pp. 73-91.

Spöerli, K.B.; Grant-Mackie, J.A., 1976, Upper Jurassic fossils from the Waipapa Group of Tawharanui Peninsula, North Auckland, New Zealand. New Zealand Journal of Geology and Geophysics, 19, pp. 21-34.

Stagpoole, V.M.; Bibby, H.M., 1998, Electrical resistivity map of the Taupo Volcanic Zone, New Zealand: nominal array spacing 500 m, 1:250,000. Lower Hutt: Institute of Geological & Nuclear Sciences. Institute of Geological & Nuclear Sciences geophysical map 11. 1 map.

Steiner, A., 1963, The rocks penetrated by drillholes in the Waiotapu geothermal area, and their hydrothermal alteration, Bulletin of the New Zealand Department of Industrial Research, 155, pp. 26–34.

Stevens, G.R. 1963, Jurassic belemnites in the Torlesse Group of the North Island. New Zealand Journal of Geology and Geophysics, 6, pp. 707-710.

Strassburger, E., 1982, Use of piezoelectric transducers for stiffness and density measurements of soils, M.S. Thesis, University of Texas.

Suggate, R.P., Stevens, G.R. and Te Punga, M.T., 1978, The Geology of New Zealand. 2 Vols., R.P. Suggate Chief Ed., Wellington, Government Printer, 820 pp.

Taylor, R.H.; Barton, K.J.; Wilson, P.R.; Thomas, B.W.; Karl, B.J. 1995, Population status and breeding of New Zealand fur seals (Arctocephalus forsteri) in the Nelson-northern Marlborough region, 1991-94, New Zealand Journal of Marine and Freshwater Research, 29, pp. 223-234.

Te Punga, M.T. 1978, Upper Jurassic fossils from the Ruahine Range: note. New Zealand Journal of Geology and Geophysics, 21, pp.773-774.

Thermomechanical analysis, checked on January 26, 2016, on Wikipedia, https://en.wikipedia.org/wiki/Thermomechanical_analysis.

Timm, C., Davy, B., Haase, K., Hoernle, K., Graham, I.J., de Ronde, C.E.J., Woodhead, J., Bassett, D., Hauff, F., Mortimer, N., Seebeck, H.C., Wysoczanski, R.J., Caratori-Tontini, F., Gamble, J.A., 2014, Subduction of the oceanic Hikurangi Plateau and its impact on the Kermadec arc Nature Communication, 5, pp. 49-68.

Vanheerden, W. L., 1987, General relations between static and dynamic moduli of rocks, International Journal of Rock Mechanics and Mining Sciences ,Abstract, 24, pp. 381–385.

Van Valkenburg, H., 1983, Backing for ultrasonic transducer crystal. Automation Industries, Inc., Greenwich Connecticut, pp. 1-18.

Villamor, P., Berryman, K.R., 2001, A late Quaternary extension rate in the Taupo Volcanic Zone, New Zealand, derived from fault slip data, New Zealand Journal of Geology and Geophysics, 44, pp. 243–269.

Vucetich, C.G., Howorth, R., 1976, Late Pleistocene tephro stratigraphy in the Taupo District, New Zealand, New Zealand Journal of Geology and Geophysics, 19, pp. 51–69.

Wallace, L.M., Beavan, J., McCaffrey, R., Darby, D.J., 2004, Subduction zone coupling and tectonic block rotations in the North Island, New Zealand Journal of Geology and Geophysics, 109, pp. 161-183.

Wallis, I.C., McNamara, D., Rowland, J.V., Massiot, C., 2012, The nature of fracture permeability in the basement greywacke at Kawerau Geothermal Field, New Zealand. IN: Proceedings, thirty-seventh Workshop on Geothermal Reservoir Engineering, January 30 - February 1, 2012, Stanford University. Stanford, Calif.: Stanford University. Stanford Geothermal Program Workshop report SGP-TR-194, pp. 9-18.

Wan, T.; Hedenquist, J.W., 1981, A reassessment of the structural control of the Broadlands geothermal field, New Zealand. IN: Proceedings of the New Zealand Geothermal Workshop 1981. Auckland: Geothermal Institute, pp. 195-202.

Wang, Z., 2000, Dynamic versus static elastic properties of reservoir rocks, Soc. Explor. Geophys. Seismic and Acoustic Velocities in Reservoir Rocks, 3, pp. 531–539.

Wheatstone bridge, checked on November 15, 2015, on Wikipedia, https://en.wikipedia.org/wiki/Wheatstone_bridge.

Wilson, C.J.N.; Houghton, B.F.; Lloyd, E.F., 1986, Volcanic history and evolution of the Maroa-Taupo area, central North Island. IN: Smith, I.E.M. (ed.) Late Cenozoic volcanism in New Zealand: a collection of papers dealing with the nature and distribution of Late Cenozoic volcanic activity in New Zealand, published in the centennial year of the 1886 eruption of Tarawera. Wellington:

Royal Society of New Zealand. Bulletin / Royal Society of New Zealand 23, pp. 194-223.

Wilson, C.J.N., Houghton, B.F., McWilliams, M.O., Lanphere, M.A., Weaver, S.D., Briggs, R.M., 1995, Volcanic and structural evolution of Taupo Volcanic Zone, New Zealand, a review, Journal of Volcanology and Geothermal Research, 68, pp. 1–28.

Wilson, C.J.N.; Manville, V. 2001, The 26.5 ka Oruanui eruption and its aftermath. IN: Lowe, D.J.; Cooke, P.J.; Pallentin, A. (eds.) Geological Society of New Zealand annual conference 2001, 27-29 November, Hamilton: Advances in geosciences: abstracts & programme. [Wellington]: Geological Society of New Zealand. Geological Society of New Zealand miscellaneous publication 110A, pp. 157-174.

Wilson, C.J.N., Rhoades, D.A., Lanphere, M.A., Calvert, A.T., Houghton, B.F., Weaver, S.D., Cole, J.W., 2007, A multiple approach radiometric age estimate for the Rotoiti and Earthquake Flat eruptions, New Zealand, with implications for the MIS 4/3 boundary, Quaternary Science Reviews, 26, pp. 1861–1870.

Wilson, C.J.N., Charlier, B.L.A., Fagan, C.J., Spinks, K.D., Gravley, D.M., Simmons, S.F., Browne, P.R.L., 2008b, U–Pb dating of zircon in hydrothermally altered rocks as a correlation tool: application to the Mangakino geothermal system, New Zealand, Journal of Volcanology and Geothermal Research, 176, pp. 191–198.

Wilson, C.J.N., Gravley, D.M., Leonard, G.S., Rowland, J.V., 2009, Volcanism in the central Taupo Volcanic Zone, New Zealand: tempo, styles and controls. In: Thordarson, T., Self, S., Larsen, G., Rowland, S.K., Hoskuldsson, A. (Eds.), Studies in Volcanology: The Legacy of George Walker. Special Publications of IAVCEI, 2, pp. 225–247.

Wilson, C.J.N., Charlier, B.L.A., Rowland, J.V., Browne, P.R.L., 2010, U–Pb dating of zircon in subsurface, hydrothermally altered pyroclastic deposits and implications for subsidence in a magmatically active rift: Taupo Volcanic Zone, New Zealand, Journal of Volcanology and Geothermal Research, 191, pp. 69–78.

Wilson C. J.N., Rowland J. V., 2016, The volcanic, magmatic and tectonic setting of the Taupo Volcanic Zone, New Zealand, reviewed from a geothermal perspective, Geothermics, 59, pp. 168–187.

Wong, T.F., Brace, W.F., 1979, Thermal expansion of rocks: some measurements at high pressure. Tectonophysics, 57, pp. 95–117.

Wood, C., Brathwaite, R.L., Rosenberg, M.D., 2001, Basement structure, lithology and permeability at Kawerau and Ohaaki geothermal fields, New Zealand, Geothermics, 30, pp. 461-481.